박 사 학 위 논 문
Ph.D. Dissertation

구조 건전성 모니터링을 위한 실시간 변형 추정

Real-time deformation estimation for structural health monitoring

2024

이 승 보 (李 承 保 Lee, Sungbo)

한 국 과 학 기 술 원
Korea Advanced Institute of Science and Technology

박 사 학 위 논 문

구조 건전성 모니터링을 위한 실시간 변형 추정

2024

이 승 보

한 국 과 학 기 술 원

기계항공공학부/기계공학과

구조 건전성 모니터링을 위한 실시간 변형 추정

이 승 보

위 논문은 한국과학기술원 박사학위논문으로
학위논문 심사위원회의 심사를 통과하였음

2024년 3월 19일

심사위원장 이 필 승 (인)
심 사 위 원 윤 정 환 (인)
심 사 위 원 박 용 화 (인)
심 사 위 원 유 승 화 (인)
심 사 위 원 오 민 한 (인)

Real-time deformation estimation for structural health monitoring

Sungbo Lee

Advisor: Phill-Seung Lee

A dissertation/thesis submitted to the faculty of
Korea Advanced Institute of Science and Technology in
partial fulfillment of the requirements for the degree of
Doctor of Philosophy in Mechanical Engineering

Daejeon, Korea
March 19, 2024

Approved by

Phill-Seung Lee
Professor of Mechanical Engineering

The study was conducted in accordance with Code of Research Ethics[1].

1) Declaration of Ethical Conduct in Research: I, as a graduate student of Korea Advanced Institute of Science and Technology, hereby declare that I have not committed any act that may damage the credibility of my research. This includes, but is not limited to, falsification, thesis written by someone else, distortion of research findings, and plagiarism. I confirm that my dissertation contains honest conclusions based on my own careful research under the guidance of my advisor.

DME

이승보. 구조 건전성 모니터링을 위한 실시간 변형 추정. 기계공학과. 2024년. 99+vi 쪽. 지도교수: 이필승. (영문 논문)

Lee, Sungbo. Real-time deformation estimation for structural health monitoring. Department of Mechanical Engineering. 2024. 99+vi pages. Advisor: Phill-Seung Lee. (Text in English)

초 록

본 연구는 실시간 변형 추정을 위한 가상 측정 방법을 다룬다. 가상 측정이란 구조물의 유한요소 모델 및 최소제곱법, 구조물로부터 측정된 실제 응답을 이용해 측정되지 않은 지점에 대한 변형을 추정하는 것이며, 결국 구조물 전 영역에 대한 변형을 추정할 수 있다. 이러한 가상 측정은 구조 건전성 모니터링 및 구조분야의 디지털 트윈을 위한 기반기술로써 활용될 수 있다. 본 연구는 모드 기반의 가상 측정을 사용하며 유한요소법을 이용해 그 절차를 정식화한다. 정규화 기법을 적용한 개선된 가상 측정 절차를 제안하고, 고정식 해양 구조물에 적용하여 그 성능을 평가한다. 또한, 구조물의 운용 하중을 고려하여 가상 측정을 위한 기저 벡터 개수 선정 가이드 및 새로운 센서 배치 방법을 제시한다. 제안된 방법은 수치 실험을 통해 그 성능이 평가된다.

핵 심 낱 말 가상 측정, 구조 건전성 모니터링, 디지털 트윈, 실시간, 유한요소법, 모드중첩법, 정규화, 센서 배치

Abstract

This research is related to virtual sensing for real-time deformation estimation. Virtual sensing is a technique that can estimate the structural responses at unmeasured region, and eventually in the full-field region of the structure using the finite element model of the structure, least squares method, and structural response measured from sensors. Virtual sensing can be utilized as a fundamental technology for structural health monitoring and digital twins in structural engineering. This study uses mode-based virtual sensing and suggest comprehensive virtual sensing formulation based on finite element method. An improved virtual sensing procedure with the regularization technique is proposed, and its performance is evaluated by applying it to a fixed offshore structure. In addition, we present guidelines for determining the numbers of basis vectors and propose a novel sensor placement method considering operational loads of the structure. The performance of the proposed methods is evaluated through numerical experiments.

Keywords Virtual sensing, Structural Health Monitoring, Digital twin, Real-time, FEM, Mode superposition, Regularization, Sensor placement

Contents

List of Tables

List of Figures

Chapter 1. Introduction

This research focuses on virtual sensing for real-time deformation estimation of the structure in the full-field region. Virtual sensing is a technique that can estimate the structural responses at unmeasured region using the finite element (FE) model, least square method, and a limited number of sensors [1-8].

Virtual sensing can estimate the structural response of the full-field region with a limited number of sensors. This means the response inside material or in areas with extreme conditions can be estimated too. By performing virtual sensing using data with a high signal-to-noise ratio, it is possible to measure structural response in a wider range and more precisely than actual sensing. In addition, through the use of real-time virtual sensing, various operational information about the structure can be acquired for structural diagnosis such as fatigue life monitoring as well as future design optimization [9, 10]; thus, virtual sensing is one of the fundamental techniques for the Structural Health Monitoring (SHM) and digital twin [11-16].

The mode superposition approach has been commonly used in virtual sensing which utilizes the displacement modes of the structure obtained from the FE model to estimate responses at unmeasured region. In virtual sensing based on mode superposition, the use of FE model and method is essential. Thus, the complete formulation of a virtual sensing based on FE method is necessary. In addition, virtual sensing using a conventional least square regression scheme can cause overfitting to input responses. Therefore, improved virtual sensing procedures are required. Signal division considering frequency of the response and regularization for generalized coordinates can solve these problems and improve the virtual sensing performance. In the early days, related studies were conducted for relatively simple structures such as beams or plates. It is necessary to confirm whether mode-based virtual sensing is effective for general structures in the operational loading conditions of the structure.

The measurement of the structural response by sensors establishes a connection between the physical structure and its digital twin, the corresponding FE model of the structure. Since the results of virtual sensing vary depending on the basis and sensor placement, basis selection and sensor placement are very important in virtual sensing [17-19]. When constructing a virtual sensing system, the number of basis vectors and sensor placement need to be carefully determined. They have been determined by the engineering insight without specific guidelines. Additionally, because structures are designed considering specific operational loads, sensor placement that consider these operational loads improve the accuracy and reliability of virtual sensing. Existing sensor placement methods, however, do not consider these operational conditions and determine sensor placement by considering only the characteristics of basis vectors.

The objective of this dissertation is developing and improving a virtual sensing method for real-time deformation estimation. First, virtual sensing procedure for real-time strain field estimation of structures is presented based on FE formulation with a signal division and a regularization scheme for accurate and robust estimation. The virtual sensing with the proposed methods is applied to a lab-scale jacket structure for experimental validation and their performance is evaluated. Second, a guideline for the numbers of basis vectors and novel sensor placement method considering operational loads of the structure are proposed for efficient and practical usage of the virtual sensing.

In Chapter 2, the complete FE formulation for strain-based virtual sensing is derived with signal division and corresponding multi-basis sets and a regularization scheme for the generalized coordinates is proposed. This study details the selection of displacement modes and the processing of strain signals for a lab-scale jacket structure, one of fixed offshore platforms, under wave loading. Virtual sensing is performed to the jacket structure according to the proposed procedure. The experimental setup and results are presented for the validation of the proposed method. Then, the accuracy of deformation estimation of virtual sensing is evaluated.

In Chapter 3, a guideline for determining proper number of basis vectors is presented. The numbers of basis vectors determined by the proposed method guarantee the target performance of the virtual sensing. In addition, a new sensor placement method considering operational loads of the structure is proposed for the better sensor placement. The proposed method determines the sensor placement providing high virtual sensing accuracy regardless of target structure even in limited sensor installation conditions and preventing overfitting in the deformation estimation. Finally, the proposed method is applied to various numerical examples and its performance is confirmed by comparing it with existing sensor placement methods.

In Chapter 4, conclusions of this research and future works for better virtual sensing are drawn.

Chapter 2. Mode-based virtual sensing

2.1 Introduction

Large structures are usually operated for a long period once installed and costs expensively in design and installation. In particular, structures such as plants, nuclear power plants, and offshore structures have a problem in that maintenance is difficult under operating conditions. In addition, according to a survey by the EU, over 38% of all European fixed offshore structures are operating beyond their design life necessitating fatigue life management and SHM for life extension. The number of structures that have exceeded the initial design lifetime will increase a lot rapidly in decades [16]. This scenario is not limited only to offshore platforms; similar situations are also present in various structural types. Fatigue life is contingent upon stress and strain variations and their cycle counts [20, 21]. Consequently, tracking stress and strain over time is imperative for fatigue life analysis.

Conducting a reliable fatigue life analysis requires full-field structural response (displacement, strain, and stress) over time. However, the high cost of sensor installation and maintenance often limits the practical number of sensors for structural response measurement. Furthermore, direct response measurement in vulnerable regions such as submerged locations in offshore structures is notably challenging. Virtual sensing, which leverages a numerical model to estimate responses at unmeasured locations, has emerged as a solution to these challenges.

The mode superposition approach has been commonly used in virtual sensing which utilizes the displacement modes of the structure obtained from the finite element model to estimate responses at unmeasured locations [3, 22-30]. This method is a type of the least square regression scheme that reconstructs the structural displacement field using appropriate displacement modes [22, 23, 31]. In the early days, related studies were conducted for relatively simple structures such as beams or plates, for which analytical models are available [22-26, 32]. Recently, monopile and tripod offshore platforms, have been addressed utilizing a finite element model [15-18]. However, the development of applicable technologies for more realistic structures remains a challenge. At this point, it is worthwhile to note that there are promising approaches in virtual sensing that utilize the Inverse Finite Element Method (iFEM) [4-7, 33-36] and deep learning techniques [1, 37-41].

Displacement mode selection, measured signal processing, and sensor placement are all critical in the mode superposition approach [42-46]. Dynamic modes have most frequently been used. Recently, operational modes or proper orthogonal decomposition (POD) modes have been adopted. Signal processing techniques have been extensively studied to achieve high-accuracy estimations [42-45]. Furthermore, a data fusion scheme has been developed to capture a broad frequency range of responses, combining both strains and accelerations [15]. The use of various sensors such as strain gauges, displacement meters, and accelerometers has also been explored, and selection and placement of these sensors significantly impact the overall process and its outcomes [2, 24].

Chapter 2 presents a comprehensive virtual sensing procedure for real-time strain field estimation of structures, from finite element (FE) formulation to experimental verification. The complete FE formulation for strain-based virtual sensing is derived for general structures, in which a scheme for the regularization of modal coordinates is introduced. The procedure hinges on a mode superposition approach. Our study details the selection of displacement modes and the processing of strain signals for a lab-scale jacket structure under real wave loading. The experimental setup, numerical tests, and experimental results are presented for verification of the proposed procedure focusing on its practical applicability. The FE model, interfaced with the actual structure via specific sensor signals, can be regarded as the digital twin of the structure.

Chapter 2 is structured as follows: Section 2.2 outlines the FE formulation for strain-based virtual sensing and regularization schemes for proper generalized coordinates. Section 2.3 presents the real-time strain field estimation procedure including strain signal division with corresponding basis sets. In Section 2.4 new regularization schemes for generalized coordinates are proposed in order to reduce overfitting. In Section 2.5, the validity and versatility of the proposed procedure are demonstrated through numerical and experimental studies, utilizing a lab-scale jacket structure under water waves. Finally, conclusions are drawn in Section 2.6.

2.2 FE formulation for virtual sensing

In this section, we derive the FE formulation to estimate the full-field responses (displacement, strain, and stress) of structures under operational loading utilizing a limited number of strain signals in real time. The signals are measured by strain sensors (gauges), which can precisely measure the structural response over a wide range of frequencies, including the static and dynamic responses, at low installation and maintenance costs.

The estimation process using the displacement signals of the structure is simpler and more convenient than that using the strain signals; however, in actual structures, measuring displacement is more difficult than measuring strain.

Note that the foundational concepts for the formulation discussed herein were initially identified in Refs [22-24], although a detailed FE formulation has not been provided yet for general structures.

2.2.1 Strain mode matrix

Let us consider a structure under its operational loading as shown in Fig. 2.1(a). The structure is discretized into an FE model of N degrees of freedom (DOFs), as shown in Fig. 2.1(b).

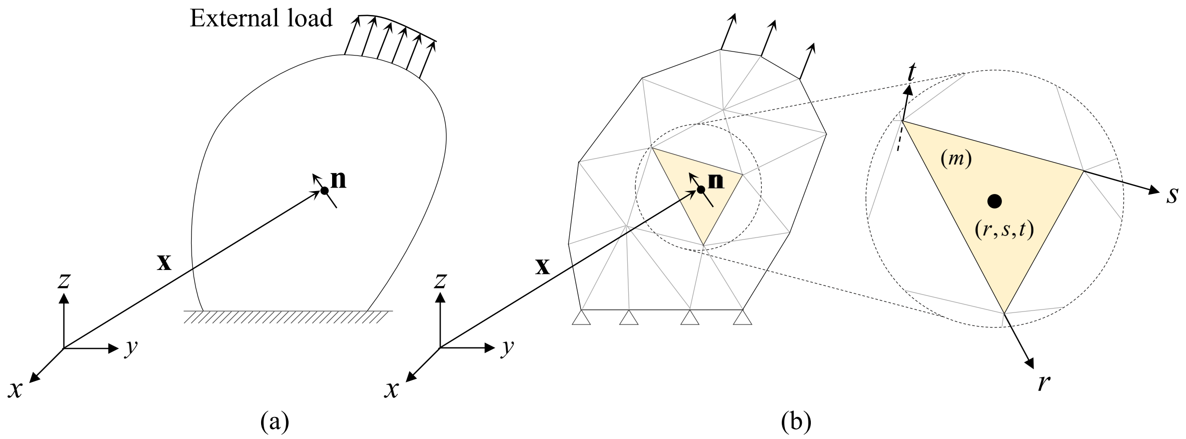

Figure 2.1: Construction of the strain mode matrix: (a) Structure under operational load, (b) Corresponding FE model.

The dynamic behavior of the structure is then expressed by [47]

$$\mathbf{M}\ddot{\mathbf{U}} + \mathbf{C}\dot{\mathbf{U}} + \mathbf{K}\mathbf{U} = \mathbf{R}, \tag{2.1}$$

where $\mathbf{U} = \mathbf{U}(t)$ with time t, $\dot{\mathbf{U}} = d\mathbf{U}/dt$, and $\ddot{\mathbf{U}} = d^2\mathbf{U}/dt^2$ denote nodal displacement, nodal velocity, and nodal acceleration vectors respectively, $\mathbf{M}$ is the mass matrix, $\mathbf{C}$ is the damping matrix, $\mathbf{K}$ is the stiffness matrix, and $\mathbf{R} = \mathbf{R}(t)$ is the external load vector.

In the mode superposition approach, the nodal displacement vector can be approximated with a combination of some proper displacement mode vectors as [47-49]

$$\mathbf{U} \approx \mathbf{\Phi}_1 q_1 + \mathbf{\Phi}_2 q_2 + \cdots + \mathbf{\Phi}_{\bar{N}} q_{\bar{N}} = \mathbf{\Phi}\mathbf{q} \quad \text{with} \quad \bar{N} \ll N, \tag{2.2}$$

where $\mathbf{\Phi}$ is the displacement mode matrix consisting of the mode vectors $\mathbf{\Phi}_i$, $\mathbf{q}$ is the corresponding generalized coordinate vector, and $\bar{N}$ is the number of displacement modes used for the approximation.

The displacement mode matrix and the generalized coordinate vector in Eq. (2.2) are defined as

$$\mathbf{\Phi} = [\mathbf{\Phi}_1 \quad \mathbf{\Phi}_2 \quad \ldots\ldots \quad \mathbf{\Phi}_{\bar{N}}] \quad \text{and} \quad \mathbf{q} = \begin{bmatrix} q_1 & q_2 & \ldots\ldots & q_{\bar{N}} \end{bmatrix}^{\mathrm{T}}. \tag{2.3}$$

Once the generalized coordinates are found, the displacement field and the corresponding strain and stress fields can be approximated.

As the FE model is composed of individual finite elements, the strain field is obtained element by element. The strain vector for the element m is defined as

$$\boldsymbol{\varepsilon}^{(m)} = \begin{bmatrix} \varepsilon_{xx} & \varepsilon_{yy} & \varepsilon_{zz} & \gamma_{xy} & \gamma_{yz} & \gamma_{zx} \end{bmatrix}^{\mathrm{T}}. \tag{2.4}$$

Let us consider a material point at $\mathbf{x} = [x \quad y \quad z]^{\mathrm{T}}$. There is an element m which includes the point in the FE model. When the natural coordinates (r, s, t) in the element corresponds to the point, the strain at $\mathbf{x}$ is calculated in the element m by

$$\boldsymbol{\varepsilon}^{(m)}(r,s,t) = \mathbf{B}^{(m)}(r,s,t)\mathbf{u}^{(m)} = \mathbf{B}^{(m)}(r,s,t)\mathbf{L}^{(m)}\mathbf{U}, \tag{2.5}$$

where $\mathbf{B}^{(m)}$ is the strain-displacement relation matrix for the element m, $\mathbf{u}^{(m)}$ is the nodal DOF vector of the element m, and $\mathbf{L}^{(m)}$ is a Boolean matrix that relates to $\mathbf{u}^{(m)}$ and $\mathbf{U}$ [47, 50-52].

Substituting Eq. (2.2) into Eq. (2.5), the strain at the point $\mathbf{x}$ is obtained in the element m with respect to the generalized coordinate vector as

$$\boldsymbol{\varepsilon}^{(m)}(r,s,t) \approx \boldsymbol{\Psi}_1^{(m)} q_1 + \boldsymbol{\Psi}_2^{(m)} q_2 + \cdots + \boldsymbol{\Psi}_{\bar{N}}^{(m)} q_{\bar{N}} = \boldsymbol{\Psi}^{(m)} \mathbf{q}$$

with $\boldsymbol{\Psi}_i^{(m)}(r,s,t) = \mathbf{B}^{(m)}(r,s,t)\mathbf{L}^{(m)}\boldsymbol{\Phi}_i$ and $\boldsymbol{\Psi}^{(m)}(r,s,t) = \mathbf{B}^{(m)}(r,s,t)\mathbf{L}^{(m)}\boldsymbol{\Phi}$, (2.6)

where $\boldsymbol{\Psi}^{(m)}$ is the strain mode matrix at $\mathbf{x}$ consisting of strain mode vectors $\boldsymbol{\Psi}_i^{(m)}$,

$$\boldsymbol{\Psi}^{(m)} = [\boldsymbol{\Psi}_1^{(m)} \quad \boldsymbol{\Psi}_2^{(m)} \quad \ldots\ldots \quad \boldsymbol{\Psi}_{\bar{N}}^{(m)}]. \tag{2.7}$$

From the strain vector in Eq. (2.6), a normal strain ε at $\mathbf{x}$ in the direction $\mathbf{n} = \begin{bmatrix} n_x & n_y & n_z \end{bmatrix}^{\mathrm{T}}$ can be calculated in the element m as

$$\varepsilon(\mathbf{x},\mathbf{n}) \approx \mathbf{Q}(\mathbf{n})\boldsymbol{\varepsilon}^{(m)}(r,s,t) = \mathbf{Q}(\mathbf{n})\boldsymbol{\Psi}^{(m)}(r,s,t)\mathbf{q}, \tag{2.8}$$

with $\mathbf{Q}(\mathbf{n}) = \begin{bmatrix} n_x^2 & n_y^2 & n_z^2 & n_x n_y & n_y n_z & n_x n_z \end{bmatrix}$,

where $\mathbf{Q}$ is the matrix used for evaluating the normal strain from the strain vector [47, 53].

2.2.2 Estimation of structural responses

We now assume that M strain sensors are attached to the structure, as shown in Fig. 2.2(a). Let us consider a strain sensor *i* attached to the structure at $\mathbf{x}_i = [x_i \quad y_i \quad z_i]^{\mathrm{T}}$. The sensor measures a normal strain in the direction $\mathbf{n}_i$. The measured normal strain is

$$e_i = e(\mathbf{x}_i, \mathbf{n}_i). \tag{2.9}$$

Considering all the normal strains (e_i) measured from sensors 1 to M, we define the measured normal strain vector as

$$\mathbf{e} = \begin{bmatrix} e_1 \\ e_2 \\ \vdots \\ e_M \end{bmatrix}. \tag{2.10}$$

Also, the estimated normal strain vector is defined as

$$\boldsymbol{\varepsilon} = \begin{bmatrix} \varepsilon_1 \\ \varepsilon_2 \\ \vdots \\ \varepsilon_M \end{bmatrix} \quad \text{with} \quad \varepsilon_i = \varepsilon(\mathbf{x}_i, \mathbf{n}_i) \approx \mathbf{Q}(\mathbf{n}_i)\boldsymbol{\Psi}^{(m_i)}(r_i, s_i, t_i)\mathbf{q}, \tag{2.11}$$

where ε_i is the estimated normal strain in the direction $\mathbf{n}_i$ at $\mathbf{x}_i$, as shown in Fig. 2.2(b), and the natural coordinates (r_i, s_i, t_i) are in the element m_i including $\mathbf{x}_i$ in the FE model. That is, ε_i corresponds to e_i.

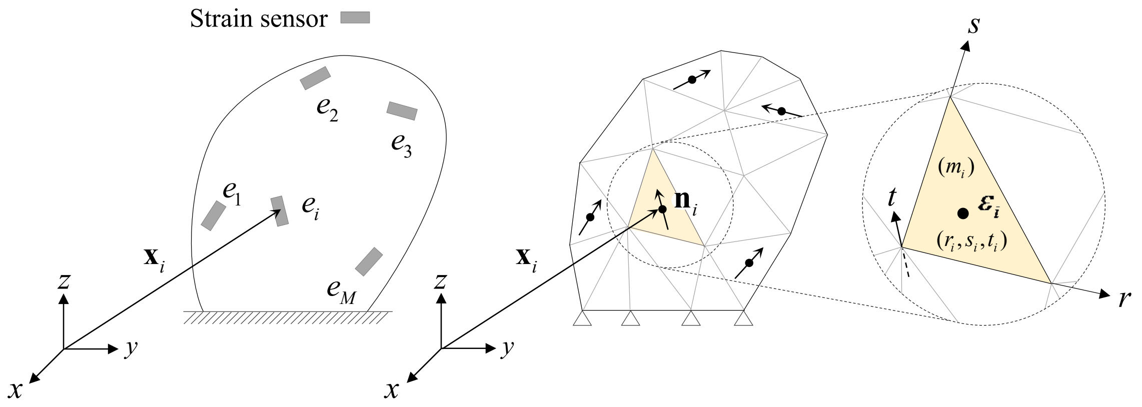

Figure 2.2: Measured and estimated normal strains: (a) Strain sensors attached on the structure, (b) Estimated strains on the corresponding FE model.

Eq. (2.11) can be rewritten as

$$\boldsymbol{\varepsilon} = \begin{bmatrix} \varepsilon_1 \\ \varepsilon_2 \\ \vdots \\ \varepsilon_M \end{bmatrix} = \mathbf{Tq} \quad \text{with} \quad \mathbf{T} = \begin{bmatrix} \mathbf{Q}(\mathbf{n}_1)\mathbf{\Psi}^{(m_1)}(r_1, s_1, t_1) \\ \mathbf{Q}(\mathbf{n}_2)\mathbf{\Psi}^{(m_2)}(r_2, s_2, t_2) \\ \vdots \\ \mathbf{Q}(\mathbf{n}_M)\mathbf{\Psi}^{(m_M)}(r_M, s_M, t_M) \end{bmatrix}, \tag{2.12}$$

where $\mathbf{T}$ is the transformation matrix to calculate the estimated normal strain vector from the generalized coordinate vector.

The difference between the measured and estimated normal strains at the positions of M sensors can be evaluated by the following cost function

$$C = \sum_{i=1}^{M} \left(\varepsilon_i - e_i\right)^2 = (\boldsymbol{\varepsilon} - \mathbf{e})^{\mathrm{T}} (\boldsymbol{\varepsilon} - \mathbf{e}) = (\mathbf{Tq} - \mathbf{e})^{\mathrm{T}} (\mathbf{Tq} - \mathbf{e}) \tag{2.13}$$

and, minimizing the cost function by $\dfrac{\partial C}{\partial \mathbf{q}} = \mathbf{0}$, the following generalized coordinate vector is found as

$$\mathbf{q}' = (\mathbf{T}^{\mathrm{T}}\mathbf{T})^{-1}\mathbf{T}^{\mathrm{T}}\mathbf{e}. \tag{2.14}$$

Substituting the resulting $\mathbf{q}'$ in Eq. (2.14) into Eq. (2.2), the nodal displacement vector is estimated by

$$\mathbf{U} \approx \mathbf{\Phi}\overline{\mathbf{q}}'. \tag{2.15}$$

For all finite elements in the FE model, the strain fields are calculated by substituting $\mathbf{q}'$ into Eq. (2.6)

$$\boldsymbol{\varepsilon}^{(m)}(r,s,t) \approx \mathbf{\Psi}^{(m)}\overline{\mathbf{q}}'. \tag{2.16}$$

The corresponding stress fields are obtained by

$$\boldsymbol{\sigma}^{(m)}(r,s,t) \approx \mathbf{C}\mathbf{\Psi}^{(m)}\overline{\mathbf{q}}' \quad \text{with} \quad \boldsymbol{\sigma} = \begin{bmatrix} \sigma_{xx} & \sigma_{yy} & \sigma_{zz} & \sigma_{xy} & \sigma_{yz} & \sigma_{zx} \end{bmatrix}^{\mathrm{T}}, \tag{2.17}$$

where $\mathbf{C}$ denotes the material law matrix and $\boldsymbol{\sigma}$ is the stress vector.

2.3 Strain field estimation of a lab-scale jacket structure

As presented in Section 2.2, the full-field responses of a structure are estimated by a linear combination of the displacement modes and the generalized coordinates calculated from several measured input strains. While the mode superposition approach requires a relatively small number of sensors and yields stable solutions, the occurrence of truncation errors is inevitable. For accurate estimation, displacement modes as the basis need to be selected carefully. It is efficient to select these basis modes considering the dynamic characteristics of the structure under an operational load condition, because, in general, most structures are exposed to specific types of operational loads rather than arbitrary loads. Without this consideration, a significantly larger number of displacement modes would be necessary to achieve the desired accuracy in virtual sensing.

In the following sections, FE model is constructed for a target structure and the procedure of the basis selection is explained considering operational loads, characteristics of the structure, and strain signal division for accurate virtual sensing.

2.3.1 Lab-scale jacket structure

An offshore jacket, a representative offshore structure, is the target structure of this study, and a lab-scale jacket structure, a prototype of the offshore jacket, was constructed for our analysis. This section explains the selection of displacement modes and division of strain signals specialized for the jacket structure.

The lab-scale jacket structure, shown in Fig. 2.3(a), is a 100 times reduced dimension model of the Donghae-1 oil platform in Korea. Instead of steel pipes, used in the actual platform of the structure, our lab-scale jacket structure was manufactured using acrylic pipes so that measurable deformation occurs by wave loads generated in an ocean basin. The lab-scale jacket structure consists of 4 main legs, 12 braces without horizontal braces through 3 floors, and a deck [54].

The total height from the bottom to the deck is 1570 mm. The main legs are composed of pipes with a 30 mm diameter and 2 mm thickness. The braces are composed of pipes with a 20 mm diameter and 2 mm thickness. The deck is a $400 \times 400\,\mathrm{mm}^2$ acrylic square plate with 20 mm thickness. The legs, braces, and deck are combined through X-, K- and Y-joints. All joints are composed of 3D-printed output filaments. To cope with the joining of members via welding in the actual jacket structure, 3D filament joints and acrylic pipes were combined with an interference fit. In addition, epoxy glue was applied to the joints to reinforce the jointing, as seen in Fig. 2.3(a) and (b).

(a)

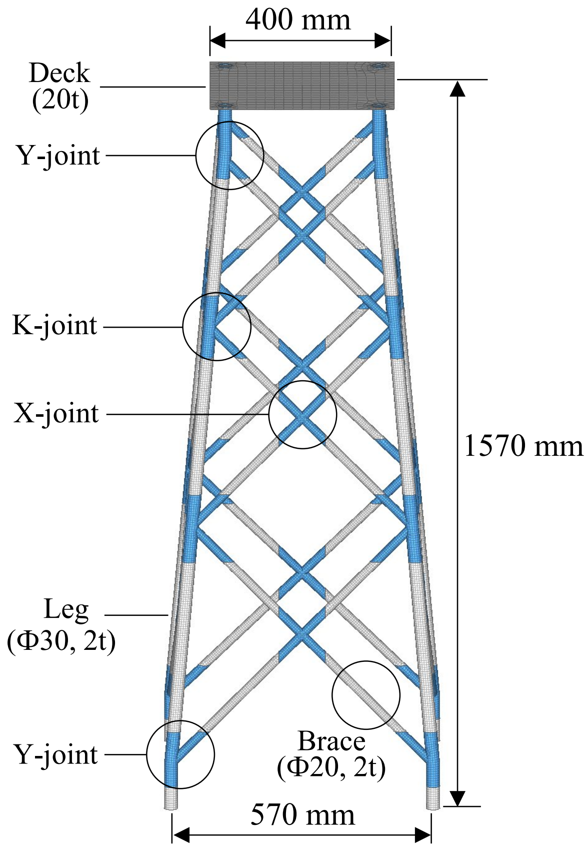

(b)

Figure 2.3: Lab-scale jacket structure: (a) Lab-scale jacket structure composed of acrylic pipes and 3D-printed output filaments, (b) Schematic of the lab-scale jacket structure with its components and dimensions.

To apply wave load to the lab-scale jacket structure, wave loading experiments were carried out in a laboratory ocean basin at KAIST. Figs. 2.4 and 2.5 show the experimental setup. The area of the ocean basin is $15 \times 10\,\mathrm{m}^2$ and the water depth was set to 1.5 m. Wave absorbers were installed at the beach and on both sides. The wave maker generates waves according to two input parameters: wave frequency and wave amplitude.

To prevent the rigid body motion of the lab-scale jacket structure due to wave loads, the foundation, where the 4 legs are clamped, must be rigid and immovable. A square plate with an area of $1000 \times 1000\,\mathrm{mm}^2$, a thickness of 200 mm, and a mass of 80 kg, was placed on the floor and moored, and the jacket legs are clamped on the plate. The submerged depth of the structure is 1.3 m; thus, the freeboard is 0.27 m.

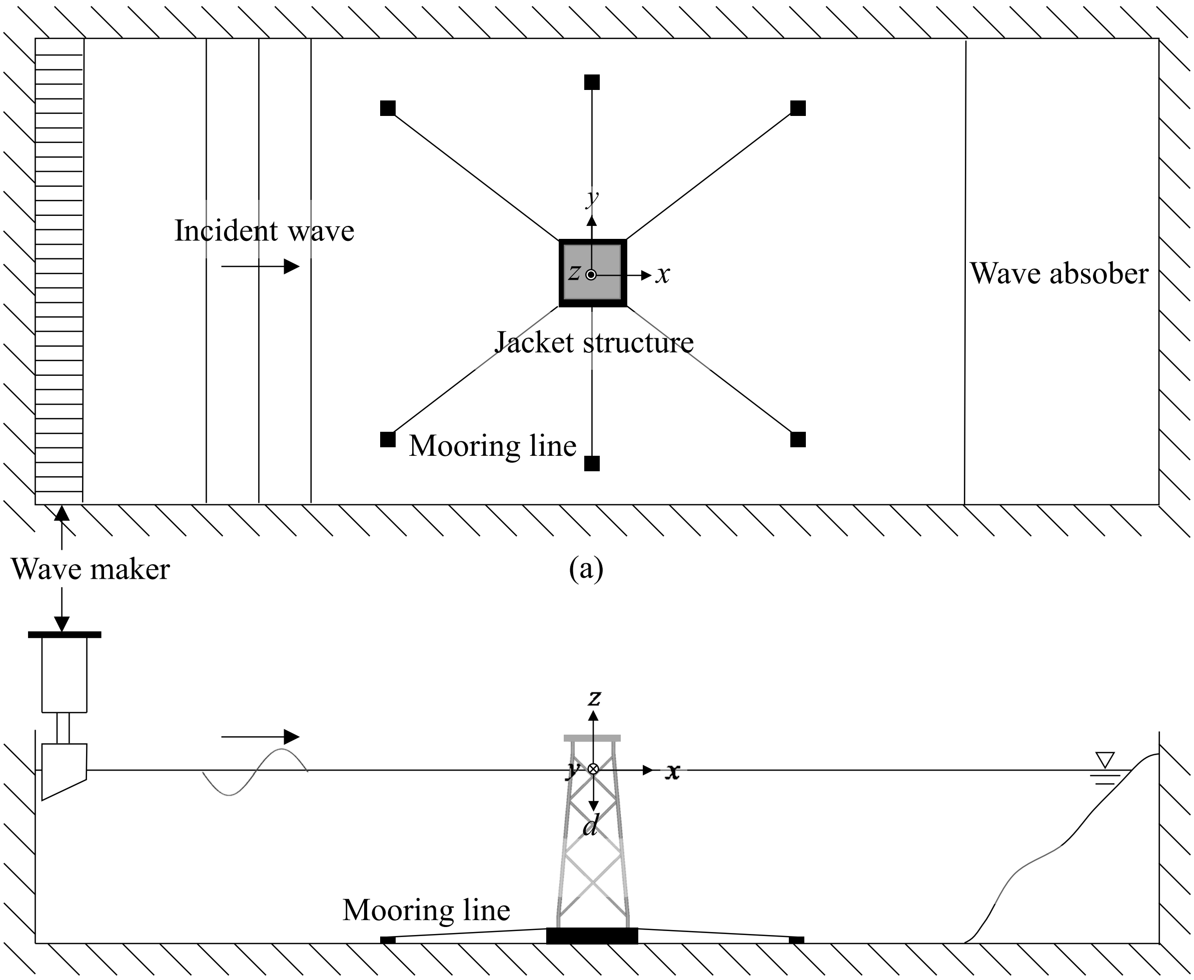

Figure 2.4: Schematic of the experimental setup: (a) Top view, (b) Front view.

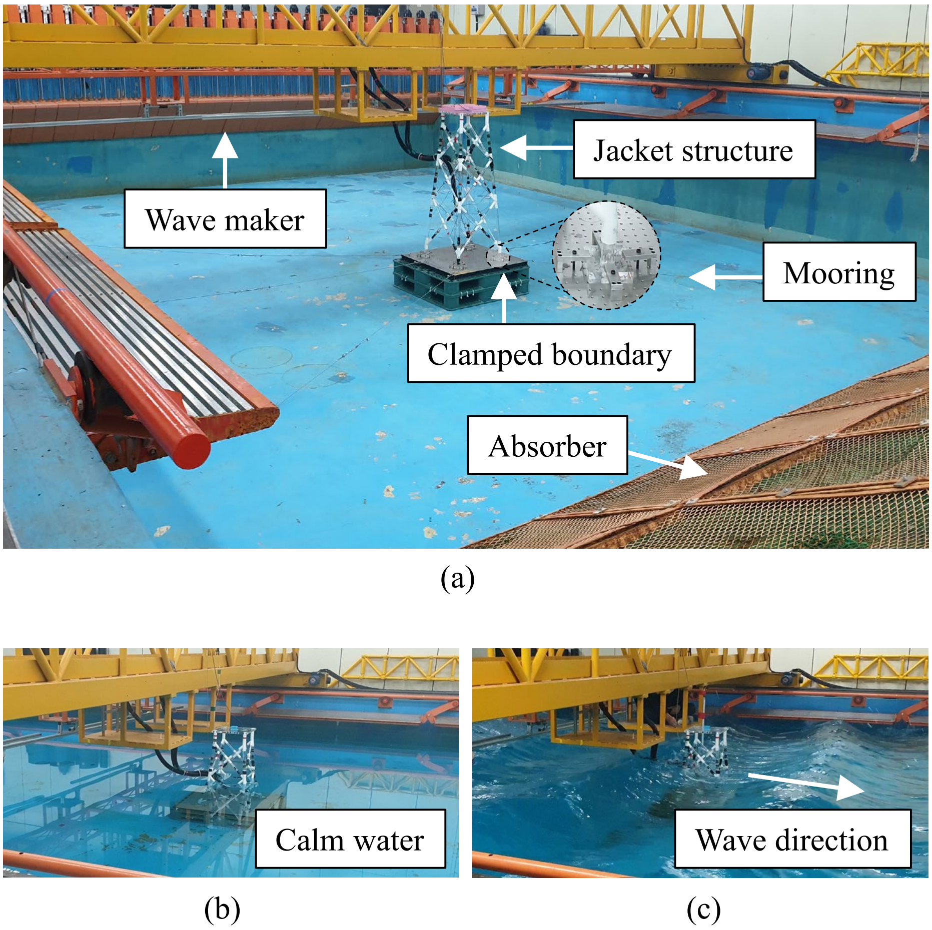

Figure 2.5: Photos of the experimental setup: (a) Ocean basin, (b) Calm water, (c) Water wave.

An FE model is required to generate displacement modes, to apply the virtual sensing process, and visualize the estimated structural responses. Fig. 2.6 presents the FE model of the built lab-scale jacket structure. The FE mesh was constructed using the MITC3 and MITC4 shell elements [47, 55, 56] and the average element size is approximately 5 mm, which is small enough for the solution to converge; as a result, the total numbers of elements and nodes are 64,647 and 62,568, respectively, and the FE model has 374,342 DOFs, N in Eq. (2.2). The pipe and joint materials are assumed to be homogeneous and isotropic. Elastic modulus E is 3900 MPa, Poisson's ratio υ is 0.3, and density ρ is $1.2\,\mathrm{kg/m^3}$.

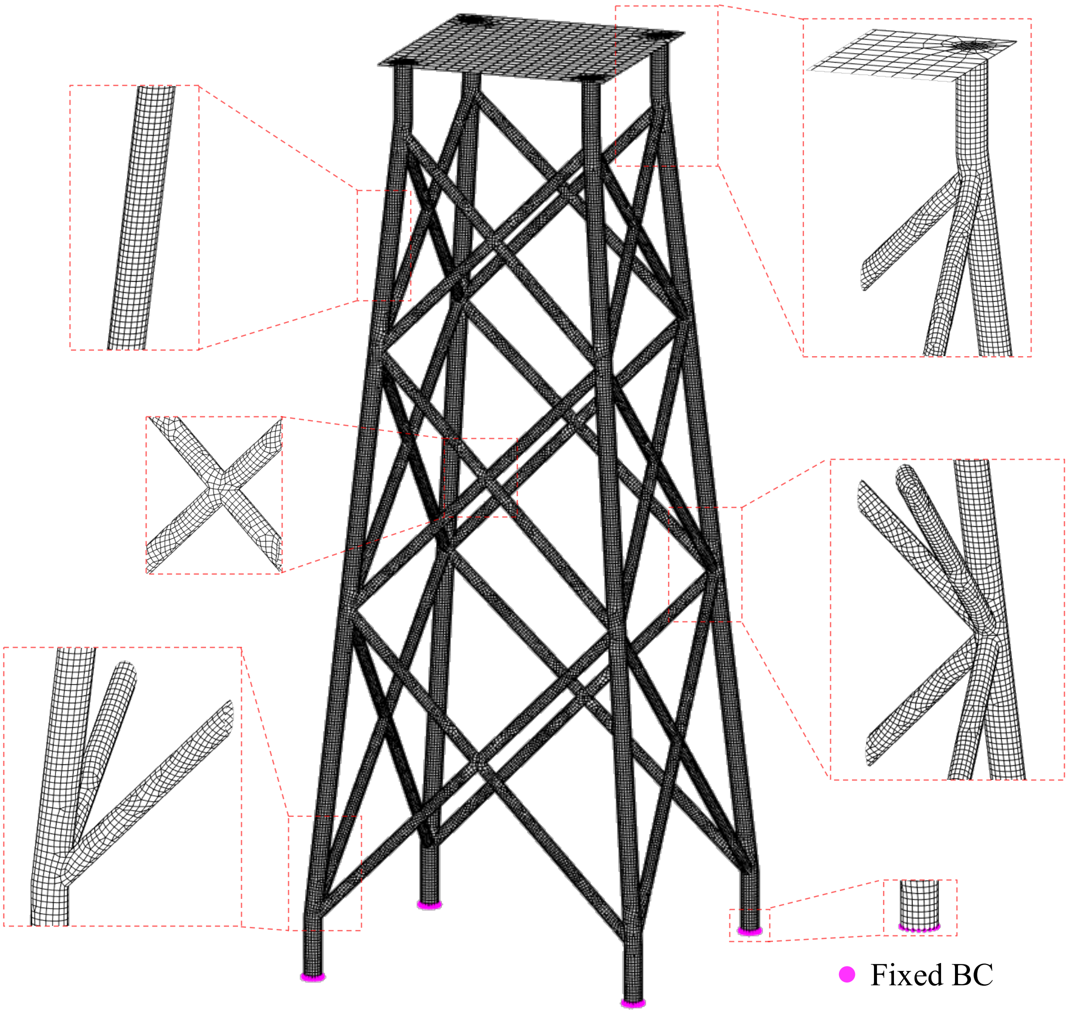

Figure 2.6: FE model of the lab-scale jacket structure.

2.3.2 Selection of displacement modes

In general, waves acting on offshore jacket structures have low frequencies that are much smaller than the 1st natural frequency of jacket structures. Therefore, the entire displacement can be divided into the load-dependent quasi-static and free vibration parts [42-44, 57, 58] as

$$\mathbf{U} = \mathbf{U}_{\text{quasi}} + \mathbf{U}_{\text{free}} \tag{2.18}$$

and both parts are separately approximated as

$$\mathbf{U}_{\text{quasi}} \approx \mathbf{\Phi}_1^{\text{quasi}} q_1^{\text{quasi}} + \mathbf{\Phi}_2^{\text{quasi}} q_2^{\text{quasi}} + \cdots + \mathbf{\Phi}_{\bar{N}_{\text{quasi}}}^{\text{quasi}} q_{\bar{N}_{\text{quasi}}}^{\text{quasi}} = \mathbf{\Phi}_{\text{quasi}} \mathbf{q}_{\text{quasi}}\,, \tag{2.19a}$$

$$\mathbf{U}_{\text{free}} \approx \mathbf{\Phi}_1^{\text{free}} q_1^{\text{free}} + \mathbf{\Phi}_2^{\text{free}} q_2^{\text{free}} + \cdots + \mathbf{\Phi}_{\bar{N}_{\text{free}}}^{\text{free}} q_{\bar{N}_{\text{free}}}^{\text{free}} = \mathbf{\Phi}_{\text{free}} \mathbf{q}_{\text{free}}\,, \tag{2.19b}$$

where “quasi” and “free” denote the load-dependent quasi-static and free vibration behaviors, respectively.

Two types of displacement modes are considered, the quasi-static displacement modes and free vibration modes, which are proper to approximate the quasi-static and free vibration behaviors, respectively. The displacement modes are obtained from the FE model.

The quasi-static displacement modes are obtained solving the following equation

$$\mathbf{K}\mathbf{U}_i = \mathbf{R}_i\,, \tag{2.20}$$

where $\mathbf{R}_i$ is the ith operational quasi-static load vector and $\mathbf{U}_i$ is the corresponding displacement vector calculated.

To obtain the quasi-static displacement modes under wave loads, a static FE analysis under wave loads is performed. The considered wave directions are $\theta = 0^\circ$ and $\theta = 90^\circ$, as shown in Fig. 2.7(a). The force applied to the pipe cross-sections is calculated by the Morison equation [59, 60] and Airy wave theory [61, 62] as

$$f(t) = \frac{1}{2}\rho C_D D v|v| + \rho C_A A \dot{v} \tag{2.21a}$$

with

$$v = \omega a \frac{\cosh(k(z+h))}{\sinh(kh)} \cos(ks - \omega t)\,, \tag{2.21b}$$

$$\dot{v} = \omega^2 a \frac{\cosh(k(z+h))}{\sinh(kh)} \sin(ks - \omega t)\,, \tag{2.21c}$$

$$\omega = \sqrt{gk \tanh(kh)}\,, \tag{2.21d}$$

$$s = x\cos\theta + y\sin\theta\,, \tag{2.21e}$$

where ρ, C_D, D, C_A, A, v, and $\dot{v}$ denote fluid density, drag coefficient, diameter of a structural member, added mass coefficient, cross-sectional area of a pipe, fluid velocity, and fluid acceleration, respectively. In Eqs. (2.21b)-(2.21e), h, a, ω, k and g represent water depth, wave amplitude, wave angular frequency, wave number, and gravitational acceleration, respectively. z, s and t represent the vertical position from the waterline, horizontal position along the wave direction, and time, respectively. The load vector $\mathbf{R}_i$ in Eq. (2.20) is calculated by uniformly distributing the cross-sectional force along the pipe circumference.

The wave parameters used in this study are presented in Table 1. Fig. 2.7(b) describes the calculated wave load distribution normalized from 0 to 1 by its maximum value.

Fig. 2.8 shows two quasi-static displacement modes with an axial strain contour normalized from -1 to 1 with its absolute maximum value. Two calculated nodal displacement vectors $\mathbf{U}_i$ corresponding to wave directions $\theta = 0^\circ$ and $\theta = 90^\circ$ are adopted as quasi-static displacement modes $\mathbf{\Phi}_i^{\text{quasi}}$; thus, the number of displacement modes used for the quasi-static part, $\bar{N}_{\text{quasi}}$ in Eq. (2.21a), is 2.

Table 2.1: Wave parameters for equivalent nodal force calculation.

Parameters	Values
ρ [$\mathrm{kg/mm^3}$]	1.024×10^{-9}
C_D [-]	0.65
D [mm]	30.0
C_A [-]	1.6
A [$\mathrm{mm^2}$]	175.93
h [mm]	1500.0
a [mm]	100.0
k [$\mathrm{mm^{-1}}$]	3.65×10^{-3}
g [$\mathrm{mm/s^2}$]	9810.0
$kx - \omega t$ [$^\circ$]	80.0

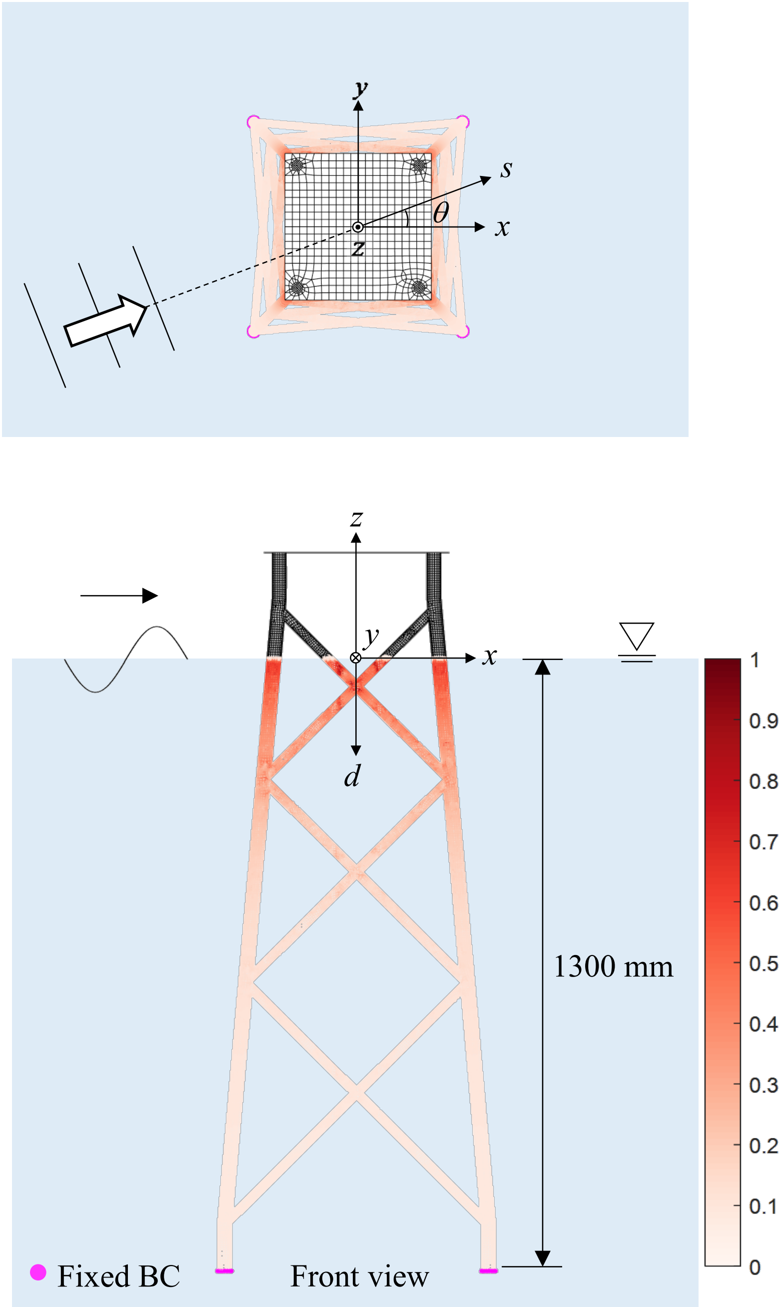

(b)

Figure 2.7: Calculation of wave loads: (a) Wave direction, (b) Normalized wave load distribution.

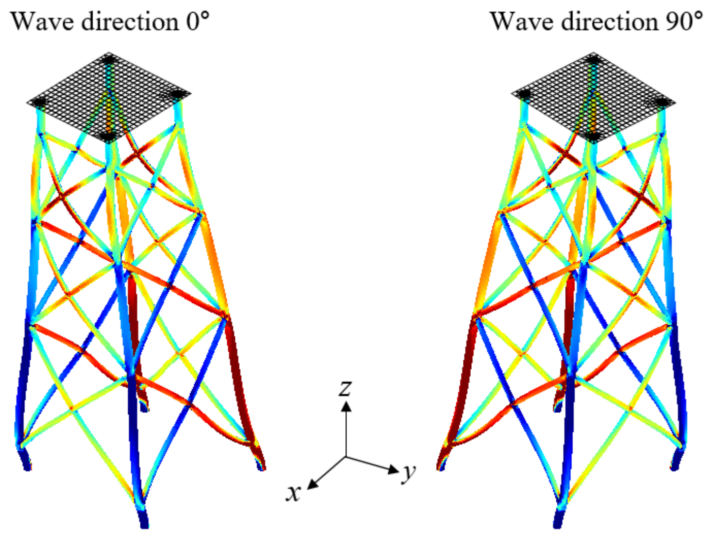

Figure 2.8: Two quasi-static displacement modes with normalized axial strain contour.

The free vibration modes are calculated by solving the following eigenvalue problem

$$[\mathbf{K}-\lambda_i\mathbf{M}]\boldsymbol{\Phi}_i^{\text{free}}=\mathbf{0}\,, \tag{2.22}$$

where λ_i and $\boldsymbol{\Phi}_i^{\text{free}}$ are the eigenvalue and eigenvector corresponding to the ith free vibration mode [47, 63, 64].

The number of free vibration modes used is determined considering the effective mass of each mode [63, 65, 66]. The effective mass is the amount of mass that moves in a specific direction when the structure vibrates in a considering mode shape. The effective mass for the ith mode in the $\mathbf{n}$ direction is defined by

$$m_i(\mathbf{n})=\left(\Gamma_i(\mathbf{n})\right)^2 \quad \text{with} \quad \Gamma_i(\mathbf{n})=\left[\boldsymbol{\Phi}_i^{\text{free}}\right]^{\mathrm{T}}\mathbf{M}\mathbf{D}(\mathbf{n})\,, \tag{2.23}$$

where $\Gamma_i(\mathbf{n})$ is the modal mass participation factor of the ith mode in the $\mathbf{n}$ direction, $\boldsymbol{\Phi}_i^{\text{free}}$ is the ith free vibration mode normalized to the mass matrix $\mathbf{M}$, and $\mathbf{D}(\mathbf{n})$ is a nodal displacement vector representing a translational rigid body motion in the $\mathbf{n}$ direction.

Since the jacket structure primarily deforms in the lateral directions due to wave loads, the number of free vibration modes for the approximation is determined so that the sum of the effective mass reaches 90% of the total mass in the two lateral directions (x- and y-directions).

To achieve this, the accumulated values from the 1st mode (accumulated mass ratio) are

$$\overline{m}_i(\mathbf{n}_x) = \sum_{k=1}^{i} m_k(\mathbf{n}_x) / m_{\text{total}} > 0.9 \quad \text{and} \quad \overline{m}_i(\mathbf{n}_y) = \sum_{k=1}^{i} m_k(\mathbf{n}_y) / m_{\text{total}} > 0.9\,, \tag{2.24}$$

where m_{total} is the total mass of the jacket structure, and $\mathbf{n}_x$ and $\mathbf{n}_y$ correspond to the x- and y-directions, respectively.

Fig. 2.9 shows the effective mass ratio and the accumulated mass ratio. As the accumulated mass ratio reaches 90% within 5 modes for both translations, 5 free vibration modes from number 1 to 5 are selected for $\mathbf{\Phi}_i^{\text{free}}$; thus, the number of displacement modes used for the free vibration part, $\overline{N}_{\text{free}}$ in Eq. (2.19b), is 5. Fig. 2.10 shows the free vibration modes from number 1 to 5 with the axial strain contours normalized from -1 to 1 with their absolute maximum values.

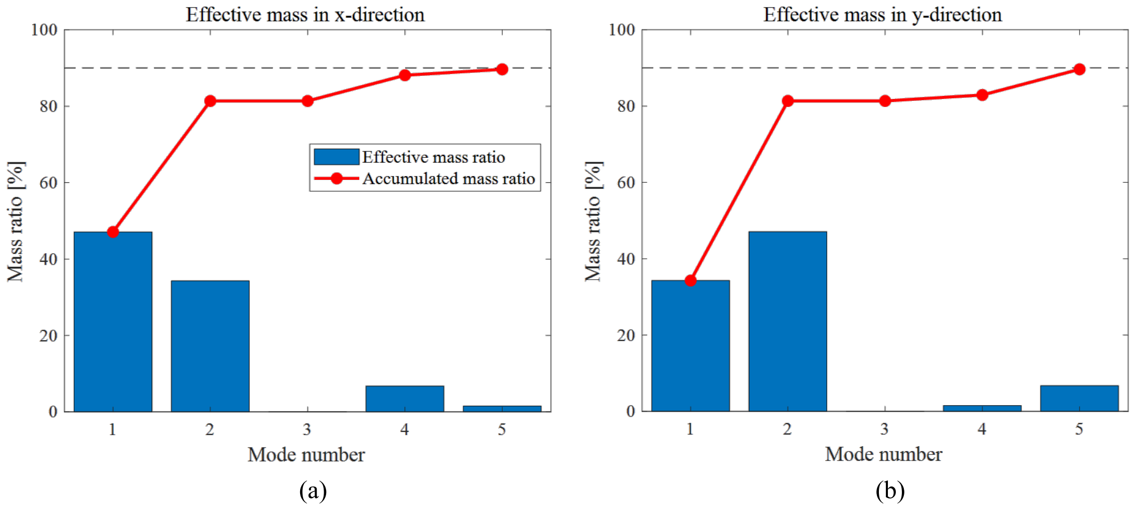

Figure 2.9: Effective and accumulated mass ratios according to mode number: (a) x-direction, (b) y-direction.

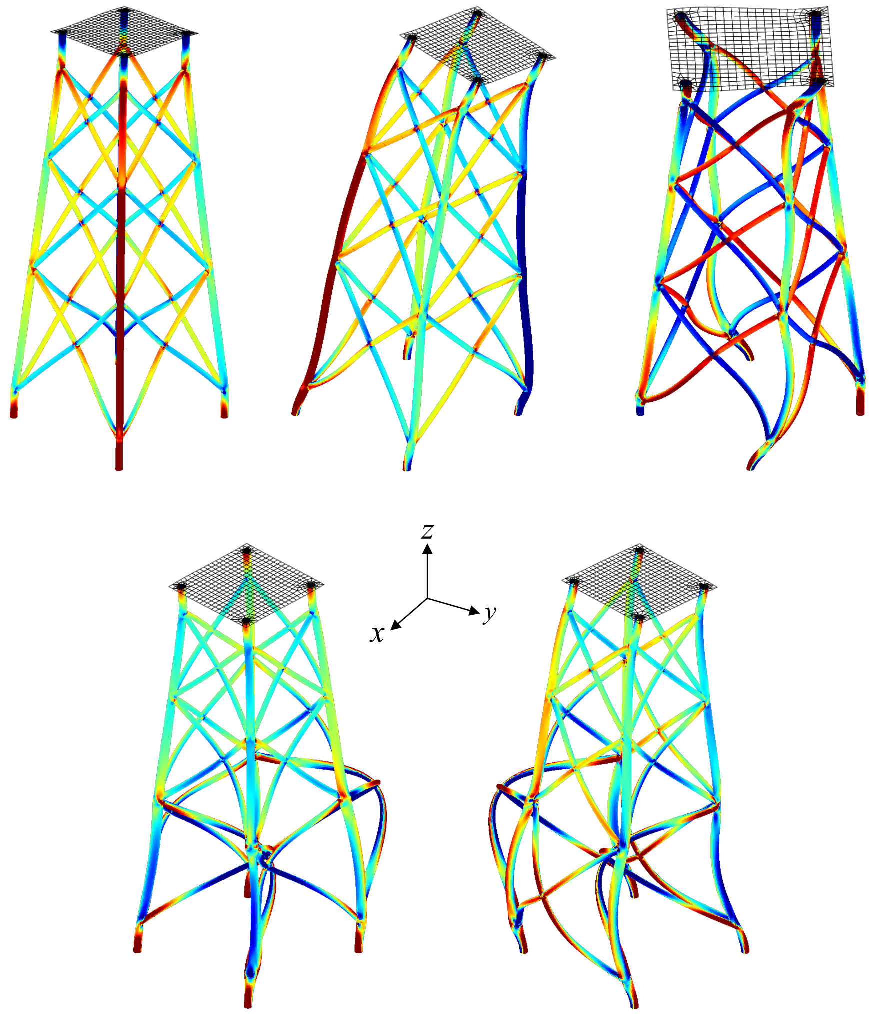

Figure 2.10: Free vibration modes from number 1 to 5 with normalized axial strain contour.

2.3.3 Strain signal division

Strain gauges measure the superimposed signals of both strain parts derived from quasi-static and free vibration behaviors with a certain level of measurement error. To obtain accurate and stable estimation results, it is necessary to correlate each type of displacement mode with the corresponding strain part, which is called multi-band modal expansion [2, 42, 45]. Since the sets of quasi-static displacement modes and free vibration modes are not orthogonal, the strain signals must be divided into quasi-static and free vibration parts to calculate the generalized coordinates.

The measured normal strain vector in Eq. (2.10) is divided into quasi-static and free vibration parts as

$$\mathbf{e} = \mathbf{e}^{\text{quasi}} + \mathbf{e}^{\text{free}}, \tag{2.25}$$

where $\mathbf{e}^{\text{quasi}}$ and $\mathbf{e}^{\text{free}}$ denote the strain vectors related to the quasi-static and free vibration behaviors, respectively.

In the strain signal, the two parts can be divided using a high pass filter, where the pass band frequency can be determined considering the frequency range of operational loads and natural frequencies of the structure. In this study, the frequencies of waves are approximately 1 Hz and the first natural frequency of the lab-scale jacket structure is approximately 23 Hz. Therefore, this study adopts 5 Hz as a cutoff frequency. The strain signal for the free vibration part is extracted through the high pass filter and the remaining signal is considered as the quasi-static part.

The generalized coordinate vectors $\mathbf{q}_{\text{quasi}}$ and $\mathbf{q}_{\text{free}}$ in Eq. (2.19) are expressed using

$$\mathbf{q}'_{\text{quasi}} = (\mathbf{T}_{\text{quasi}}^{\text{T}} \mathbf{T}_{\text{quasi}})^{-1} \mathbf{T}_{\text{quasi}}^{\text{T}} \mathbf{e}_{\text{quasi}}, \tag{2.26a}$$

$$\mathbf{q}'_{\text{free}} = (\mathbf{T}_{\text{free}}^{\text{T}} \mathbf{T}_{\text{free}})^{-1} \mathbf{T}_{\text{free}}^{\text{T}} \mathbf{e}_{\text{free}}, \tag{2.26b}$$

with

$$\mathbf{T}_{\text{quasi}} = \begin{bmatrix} \mathbf{Q}(\mathbf{n}_1)\mathbf{\Psi}_{\text{quasi}}^{(m_1)}(r_1, s_1, t_1) \\ \mathbf{Q}(\mathbf{n}_2)\mathbf{\Psi}_{\text{quasi}}^{(m_2)}(r_2, s_2, t_2) \\ \vdots \\ \mathbf{Q}(\mathbf{n}_M)\mathbf{\Psi}_{\text{quasi}}^{(m_M)}(r_M, s_M, t_M) \end{bmatrix}, \tag{2.27a}$$

$$\mathbf{T}_{\text{free}} = \begin{bmatrix} \mathbf{Q}(\mathbf{n}_1)\mathbf{\Psi}_{\text{free}}^{(m_1)}(r_1, s_1, t_1) \\ \mathbf{Q}(\mathbf{n}_2)\mathbf{\Psi}_{\text{free}}^{(m_2)}(r_2, s_2, t_2) \\ \vdots \\ \mathbf{Q}(\mathbf{n}_M)\mathbf{\Psi}_{\text{free}}^{(m_M)}(r_M, s_M, t_M) \end{bmatrix}. \tag{2.27b}$$

Finally, the entire displacement field is estimated by

$$\mathbf{U} = \mathbf{\Phi}_{\text{quasi}} \mathbf{q}'_{\text{quasi}} + \mathbf{\Phi}_{\text{free}} \mathbf{q}'_{\text{free}} , \tag{2.28}$$

the corresponding strain field for element m is calculated by

$$\boldsymbol{\varepsilon}^{(m)}(r,s,t) \approx \mathbf{\Psi}^{(m)}_{\text{quasi}} \mathbf{q}'_{\text{quasi}} + \mathbf{\Psi}^{(m)}_{\text{free}} \mathbf{q}'_{\text{free}} , \tag{2.29}$$

and the corresponding stress field for element m is calculated by

$$\boldsymbol{\sigma}^{(m)}(r,s,t) \approx \mathbf{C}\mathbf{\Psi}^{(m)}_{\text{quasi}} \mathbf{q}'_{\text{quasi}} + \mathbf{C}\mathbf{\Psi}^{(m)}_{\text{free}} \mathbf{q}'_{\text{free}} . \tag{2.30}$$

The process of the full-field response estimation with the strain signal division is depicted in Fig. 2.11.

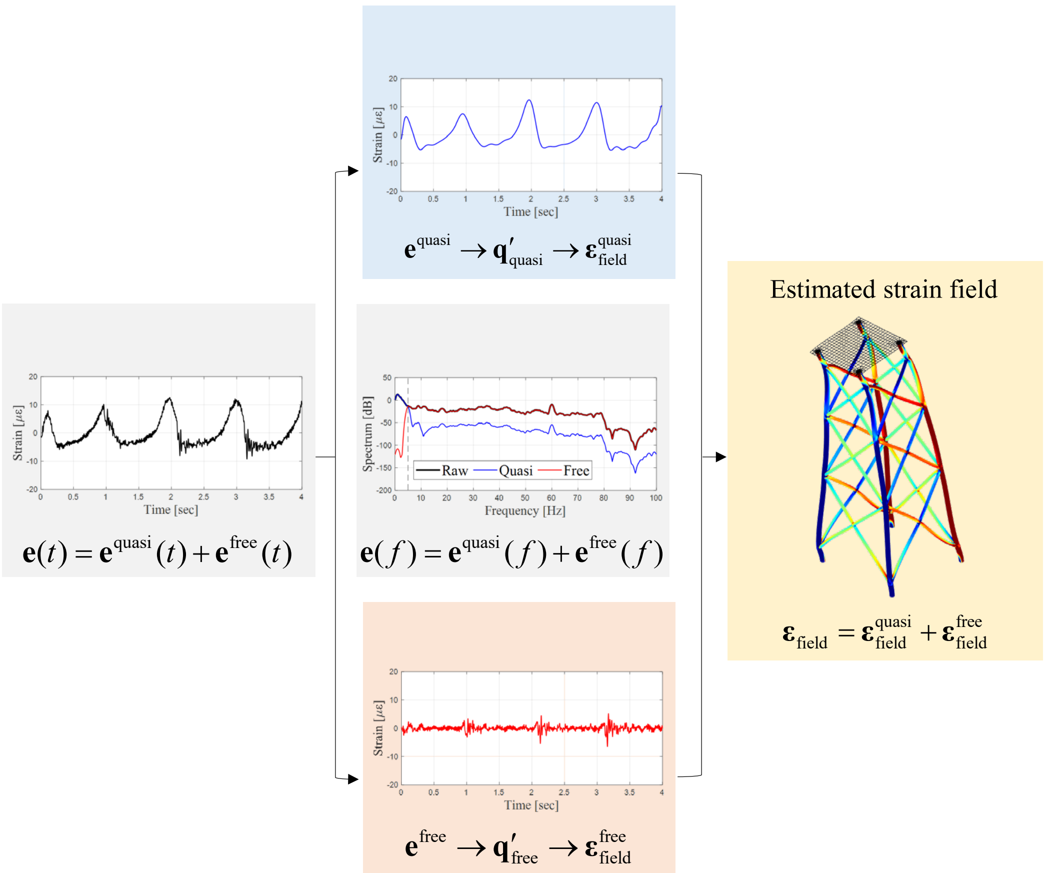

Figure 2.11: The process of the full-field response estimation with strain signal division.

2.4 Regularization of generalized coordinates

Estimation results obtained using the least-square solution in Eq. (2.14) are likely to be overfitted to the measured input strains. Fig. 2.12 shows the overfitting in virtual sensing conceptually, where the accuracy of the estimated strain at measured region is high but that at virtually measured region is low [67-69]. When sensors are located close to each other and the number of sensors is small in comparison to the number of displacement modes, the possibility of overfitting increases. When the number of sensors is equal to that of the displacement modes, the input strains are reconstructed identically; however, the accuracy in the virtual sensing region could severely deteriorates due to overfitting. The distortion would be severe if the input response is contaminated by several disturbance such as truncation error, measurement error, damage of strain sensors, etc. because the estimation results are severely overfitted to the wrong measured response.

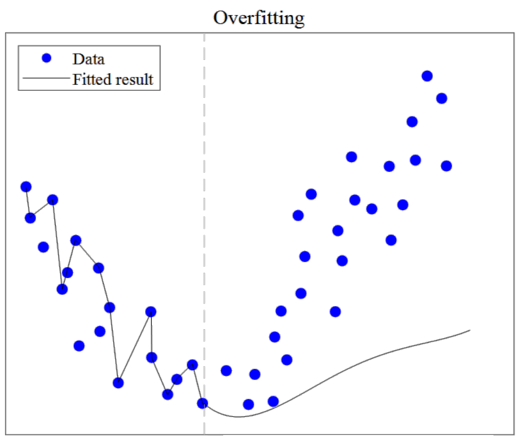

Figure 2.12: Overfitting in virtual sensing.

Regularizing the generalized coordinates could reduce overfitting and increases the estimation accuracy and stability. A regularization scheme is one approach utilized to prevent overfitting by making the regression result smooth and simple in exchange for a tolerable amount of bias [70-72]. The cost function is newly re-defined to regularize the generalized coordinates by adding the norm of the generalized coordinate vector to Eq. (2.13), where the regularization form is referred to as Tikhonov regularization [70, 72],

$$\bar{C} = \sum_{i=1}^{M}\left(\varepsilon_i - e_i\right)^2 + \alpha\sum_{i=1}^{\bar{N}} q_i^{\,2} = (\boldsymbol{\varepsilon}-\mathbf{e})^{\mathrm{T}}(\boldsymbol{\varepsilon}-\mathbf{e}) + \alpha\left\|\mathbf{q}\right\|^2 = (\mathbf{Tq}-\mathbf{e})^{\mathrm{T}}(\mathbf{Tq}-\mathbf{e}) + \alpha\mathbf{q}^{\mathrm{T}}\mathbf{q}\,, \tag{2.31}$$

where α is a regularization factor.

The regularization effect varies according to the scale of α. A proper regularization factor α depends on the problem and could be determined by trial and error or a heuristic criterion [49, 50]. To have a meaningful effect on the cost function by regularization, the 2nd term, the norm of the generalized coordinates, needs to have a similar order of magnitude to the 1st term, the strain difference. We here determine the value of α through trial-and-error considering the scale of the measured strain vector $\mathbf{e}$ and that of the generalized coordinate vector $\mathbf{q}$.

Minimizing the re-defined cost function by $\frac{\partial \overline{C}}{\partial \mathbf{q}} = \mathbf{0}$, the generalized coordinate vector is found as

$$\overline{\mathbf{q}}' = (\mathbf{T}^{\mathrm{T}}\mathbf{T} + \alpha\mathbf{I})^{-1}\mathbf{T}^{\mathrm{T}}\mathbf{e}, \tag{2.32}$$

and the corresponding nodal displacement vector, strain field and stress field are calculated by Eqs. (2.15), (2.16), and (2.17), respectively.

Free vibration behavior from the divided strain signal in Eq. (2.25) is usually weak to disturbance and easily contaminated compared to the quasi-static behavior. That is because strain of the free vibration behavior is much smaller than that of the quasi-static behavior, which makes the free vibration strain easy to contaminated by even a small measurement noise. In addition, the strain error by truncation of the free vibration strain is usually large because a lot of dynamic displacement modes are truncated. These means the estimation result of free vibration behavior is weak to overfitting, and the regularization scheme in Eq. (2.32) is only applied to the free vibration part; thus, Eq. (2.26b) is replaced with Eq. (2.32). Finally, the corresponding nodal displacement vector, strain field, and stress field are calculated by Eqs. (2.28), (2.29), and (2.30), respectively, with (2.26a) for quasi-static part and (2.32) for free vibration part.

Fig. 2.13 shows the procedure of the full-field response estimation divided into offline and online processes. In the offline process, the FE model in Eq. (2.1) is constructed and displacement modes in Eq. (2.2) are generated from the FE model of the structure. The location and direction of sensors are determined as in Eq. (2.9). Then, the transformation matrices in Eqs. (2.27a) and (2.27b) are constructed utilizing the displacement modes and the sensor placement. In the online process, the strain signals in Eq. (2.10) are measured and then the generalized coordinates are calculated from the transformation matrix and the conditioned real-time sensor signals using Eq. (2.26a) and (2.32). Finally, the full-fields of displacement, strain, and stress are estimated using Eqs. (2.28), (2.29), and (2.30), respectively. The structural responses can then be used to diagnose the health state of structures.

Even though virtual sensing is performed through the improved procedure following Eqs. (2.26)-(2.32), the accuracy is still affected by modeling error, measurement error, and numerical error. Therefore, when constructing a virtual sensing system, FE modeling, measurement setup, and numerical techniques should be carefully considered to reduce the effect of these error sources.

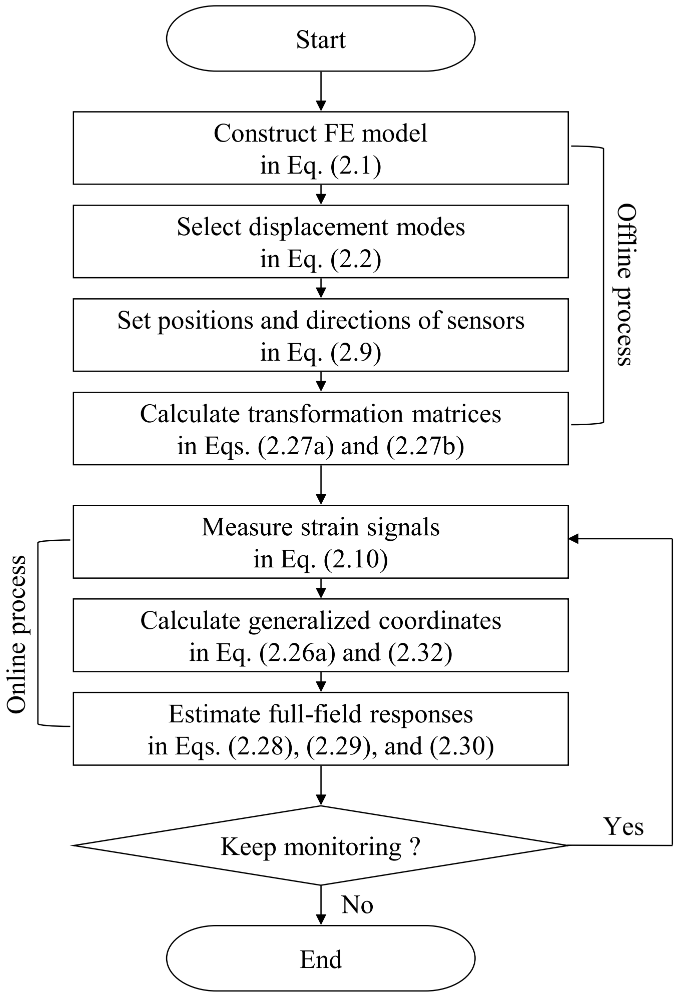

Figure 2.13: The procedure of the full-field response estimation.

2.5 Lab-scale experiments

The performance of the strain field estimation proposed in this study was evaluated through the jacket structure under wave loading numerically and experimentally. In this section, the experimental setup on the lab-scale jacket structure under wave loading is described and the stain field estimation results are investigated.

2.4.1 Experimental setup

For measurement setup, a DAQ system with NI 9236 [73] and NI 9178 [74] was used. The sampling rate for the strain measurement was 1000 Hz, which is enough to prevent aliasing considering the frequencies of the wave loads and the natural frequencies of the structure. LABVIEW was used for real-time data processing including strain signal division, calculation of the generalized coordinates, and visualization of the results [75].

The strain was measured using a NI 9236 Wheatstone bridge and HBM 350-ohm linear uniaxial strain gauges (K-CLY41-6/350) attached to the surface of the pipes in their axial directions. All strain gauges are waterproofed with a silicone coating [76].

The strain gauges, called input sensors, measure the input strain signals for virtual sensing. Input strain gauges were installed above the waterline. Additional strain gauges, called validation sensors, were installed at the virtual sensing region under the waterline. To validate the virtual sensing results, the estimated strains need to be directly compared with the measured strains.

Fig. 2.14 shows the placement of the 26 installed strain gauges: 10 input sensors (colored in yellow) above the waterline, and 16 validation sensors (colored in green) under the waterline.

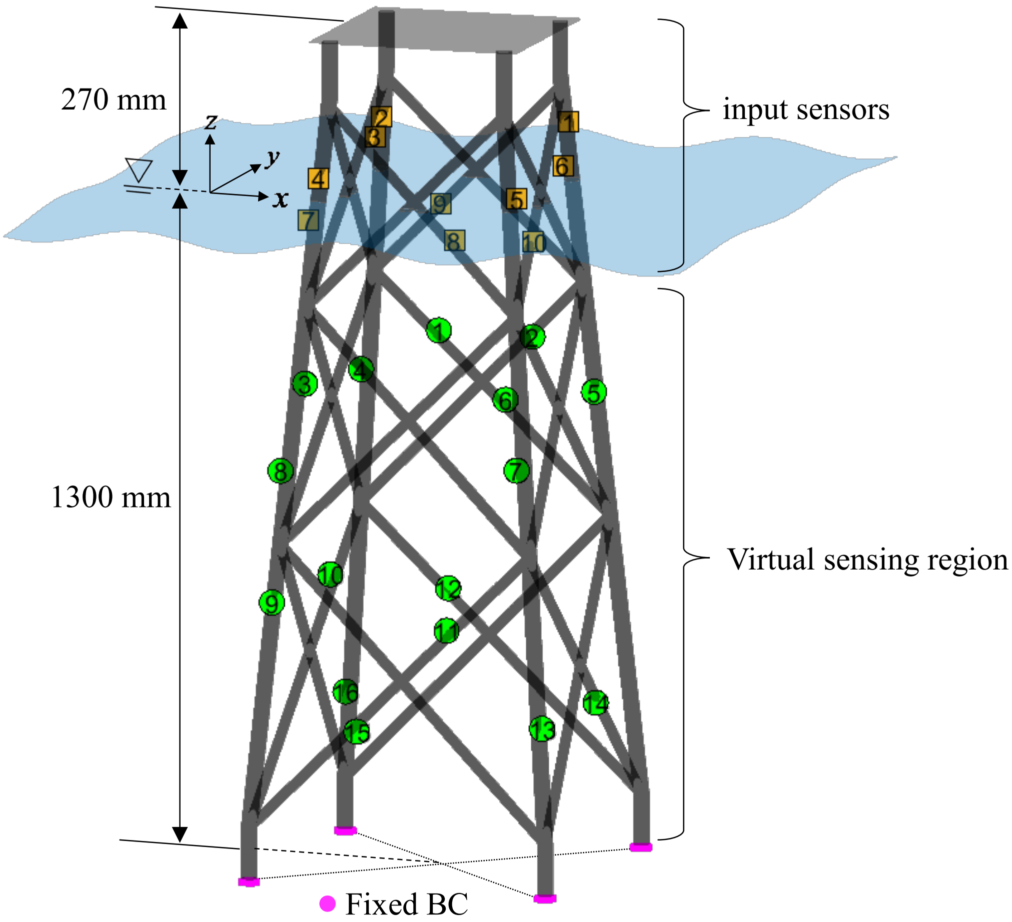

Figure 2.14: Placement of input sensors (colored in yellow) and validation sensors (colored in green).

2.4.2 Numerical tests

In the virtual sensing process, the selected displacement modes should be accurate enough to reconstruct full-field deformation under operational loading conditions; that is, the deformed shape can be represented by the selected displacement modes with the desired accuracy. In numerical analysis, there are no measurement errors and modeling errors. The virtual sensing formulation as well as the selected displacement modes was verified through numerical tests.

In the numerical tests, the measured strains were replaced with the reference strains calculated from FE analysis and the same sensor placement with that of the actual experiment is applied. Strain signals were obtained from dynamic FE analysis performed under the following conditions: implicit analysis is applied, the sampling rate is 1000 Hz, wave direction is $\theta = 45^\circ$, and wave frequency is 1 Hz. The other wave parameters in Eq. (2.21) are listed in Table 2.1.

As mentioned in Section 2.3, 2 quasi-static displacement modes in the directions of $\theta = 0^\circ$ corresponding to the x-direction and $\theta = 90^\circ$ corresponding to the y-direction are employed to cover load-dependent quasi-static behavior. For free vibration behavior, 5 free vibration displacement modes are adopted. Signals obtained from 10 input strain sensors above the waterline are divided using a high pass filter with a 5 Hz cutoff frequency.

The regularization factor α in Eq. (32) is adopted as 5.0×10^{-12}. The 1st and 2nd terms in Eq. (31) need to have similar orders of magnitude. The scale of the 1st term ($(\mathbf{Tq}-\mathbf{e})^{\mathrm{T}}(\mathbf{Tq}-\mathbf{e})$) is about $10^{-13} \sim 10^{-10}$ and the scale of $\mathbf{q}^{\mathrm{T}}\mathbf{q}$ is about $10^{0} \sim 10^{1}$. The scale of a proper regularization factor is in the range of $10^{-13} \sim 10^{-11}$. The specific value is determined through trial and error, within the range that enhances the accuracy of virtual sensing.

Virtual sensing is carried out following the procedure of the full-field response estimation in Fig. 2.13. The accuracy of the estimated strain field and deformed shape were evaluated by strain modal assurance criterion (EMAC) and displacement modal assurance criterion (UMAC) as

$$\mathrm{EMAC}(t) = \frac{\left(\boldsymbol{\varepsilon}_{\mathrm{field}}(t) \cdot \mathbf{e}_{\mathrm{field}}(t)\right)^2}{\left(\boldsymbol{\varepsilon}_{\mathrm{field}}(t) \cdot \boldsymbol{\varepsilon}_{\mathrm{field}}(t)\right)\left(\mathbf{e}_{\mathrm{field}}(t) \cdot \mathbf{e}_{\mathrm{field}}(t)\right)}, \tag{2.33a}$$

$$\mathrm{UMAC}(t) = \frac{\left(\mathbf{U}(t) \cdot \hat{\mathbf{U}}(t)\right)^2}{\left(\mathbf{U}(t) \cdot \mathbf{U}(t)\right)\left(\hat{\mathbf{U}}(t) \cdot \hat{\mathbf{U}}(t)\right)}, \tag{2.33b}$$

where $\boldsymbol{\varepsilon}_{\text{field}}(t)$ and $\mathbf{e}_{\text{field}}(t)$ are the estimated and measured (or reference) normal strain vectors at time t, respectively, which consist of axial strains obtained at the centers on the top surfaces of all 64,647 elements modeling the pipe members, and $\mathbf{U}(t)$ and $\hat{\mathbf{U}}(t)$ are the estimated and measured (or reference) nodal displacement vectors at time t, respectively.

Fig. 2.15(a) presents the estimated and reference displacements, and Fig. 2.15(b) presents the estimated and reference normal strains in the axial direction, where each title of the graph denotes water depth of its validation sensors, $d\ (=-z)$. In Fig. 2.15(a), the estimated and reference displacements in the x-direction at the top surface center of the deck and at the position of validation sensor 15 are compared. The estimated displacements are nearly identical to the references. Similar results are obtained at other points. As shown in Fig. 2.15(b), the estimated and reference strains are also very close to each other at validation sensors 3 and 9. Estimated strains at other validation sensors have the same extent of accuracy. Fig. 2.15(c) shows the estimated and reference deformed shapes with strain contours normalized from -1 to 1 with its absolute maximum value at time $t = 0.25\,s$: the moment of the wave crest. The EMAC and UMAC were 0.9991 and 0.9996, respectively.

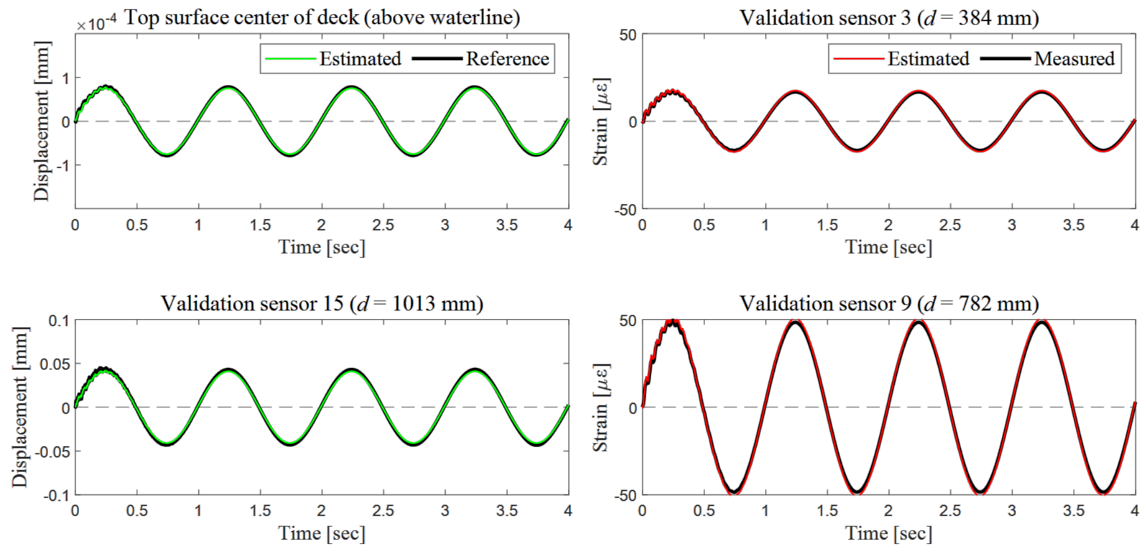

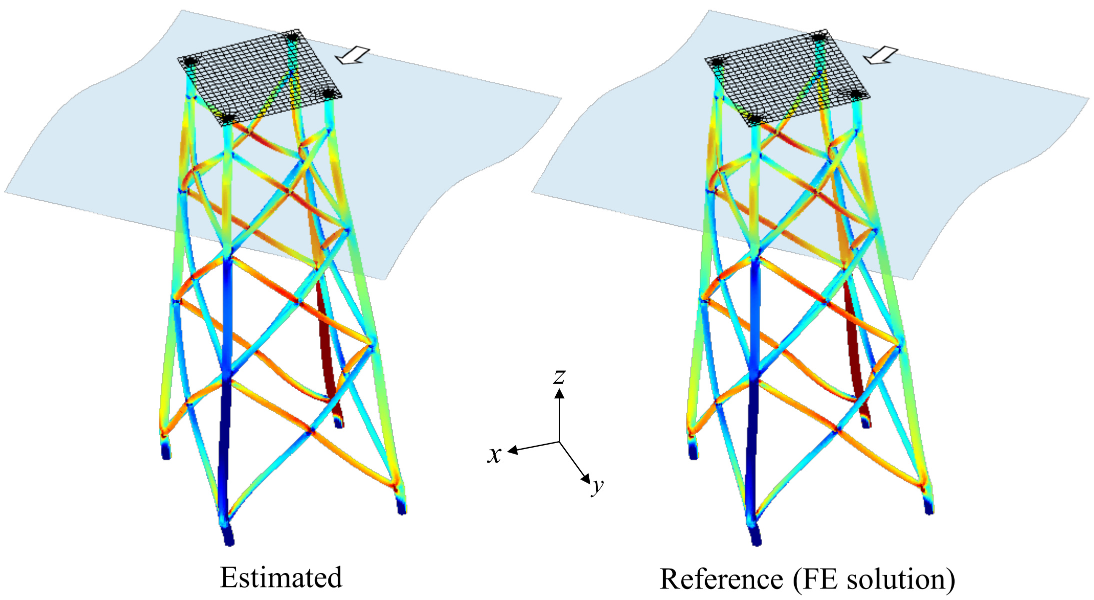

(c)

Figure 2.15: Comparison of estimated and reference responses: (a) Estimated and reference displacements in the x-direction, (b) Strain signals at validation sensors, (c) Estimated and reference deformed shapes with normalized axial strain contours at the moment of wave crest.

2.4.3 Dry condition experiments

Before the wave loading experiments in an ocean basin, we performed dry condition experimental tests. A dynamic load was applied on the deck, as shown in Fig. 2.16. The virtual sensing conditions were identical with the numerical tests except for the quasi-static displacement modes selected. In the dry condition experiments, the quasi-static displacement modes were replaced with static deformed shapes calculated by the forces acting on the deck in the x- and y-directions, as shown in Figs. 2.17(a) and (b).

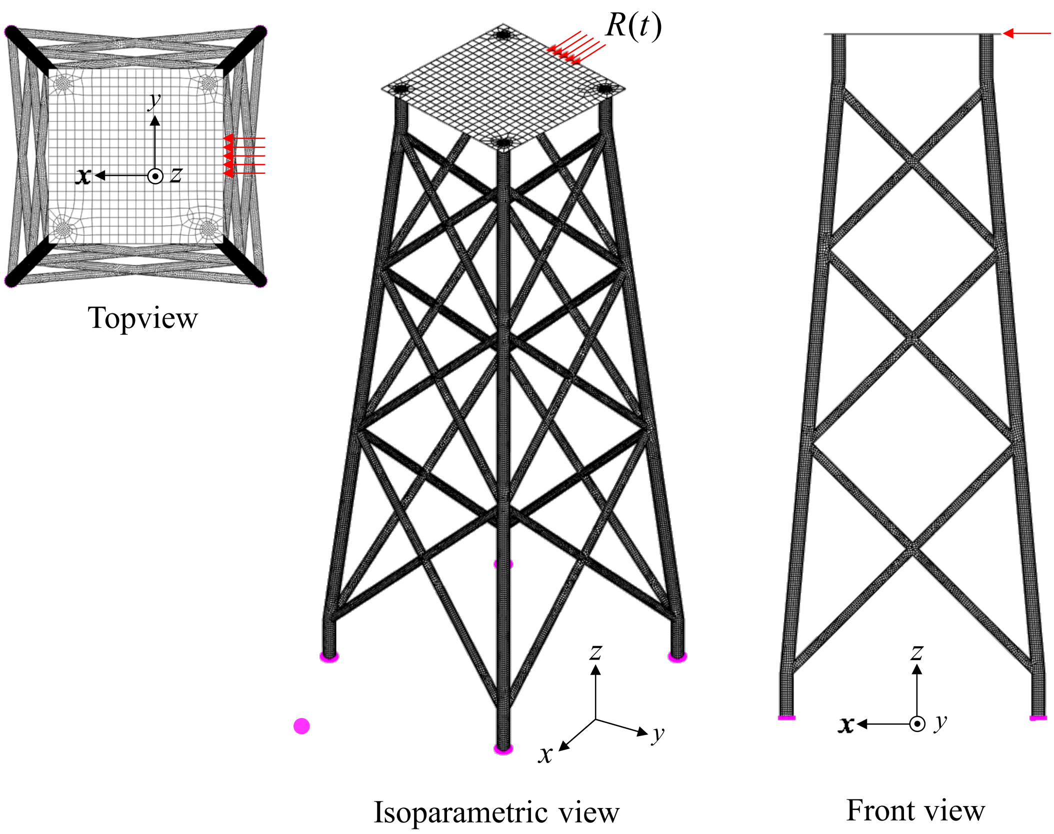

Figure 2.16: Dynamic loads applied on the deck in the dry condition experiments.

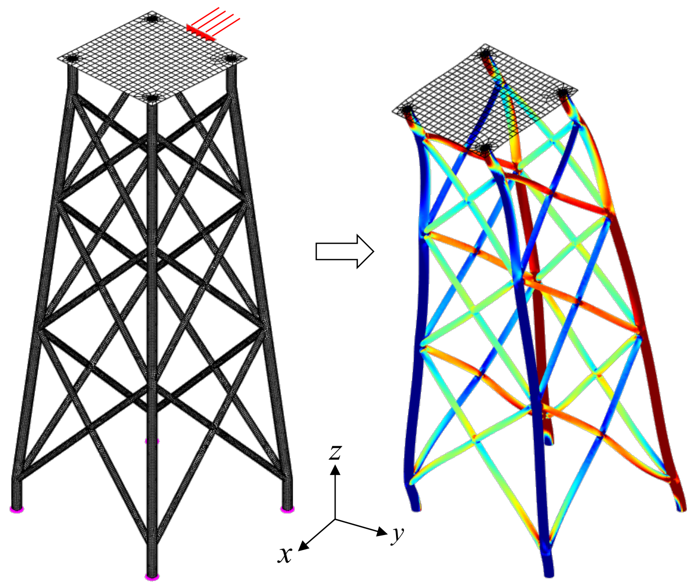

(a)

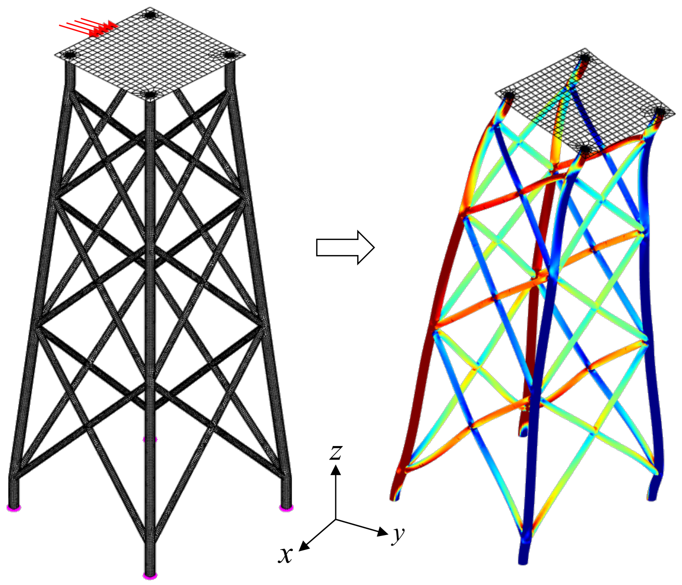

Figure 2.17: Two quasi-static displacement modes with normalized axial strain contour in the dry condition experiments: (a) x-direction, (b) y-direction.

Fig. 2.18 presents the estimated and measured normal strain signals in the axial direction at validation sensors 3 and 9. The estimated strains are in good agreement with the measured strains, and other validation sensors also showed similar results. In these experiments, only strain signals were measured.

Through the numerical tests and dry condition experiments, it is confirmed that the strain field can be estimated with high accuracy through virtual sensing by the proposed procedure.

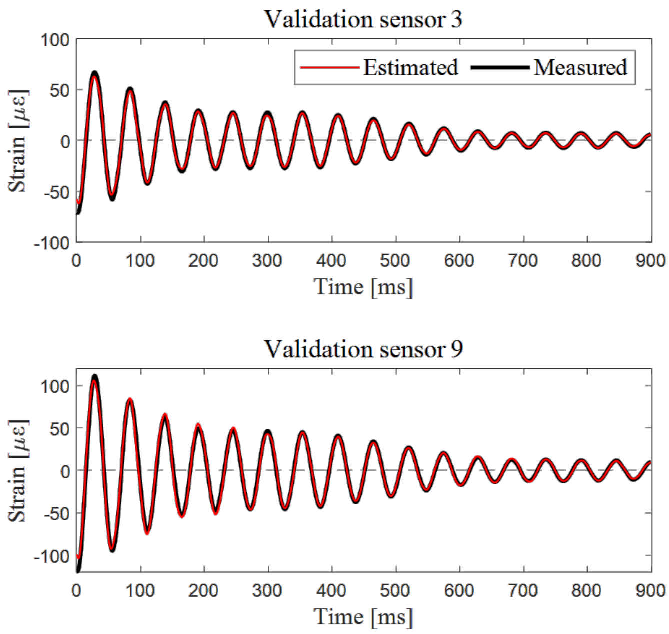

Figure 2.18: Comparison of virtual sensing results with measured strain signals in the dry condition test.

2.4.4 Experimental tests under waves

To estimate the actual strain field of the lab-scale jacket structure under wave loads by utilizing several measured strain signals, wave loading experiments were carried out in a laboratory ocean basin. Basically, the virtual sensing conditions were identical with those of the numerical test.

Compared to the numerical tests and dry condition experiments, various error sources exist in actual wave experiments. Measurement errors like direct loading onto the strain gauge surface, humidity and temperature of the circumstance, electrical noise, etc. could distort the strain signals. Modeling errors, which represent differences between the lab-scale jacket structure and its FE model, are also important error sources.

Experimental tests were performed under regular and irregular wave conditions. To evaluate the performance of virtual sensing with proposed regularization scheme, results of virtual sensing by 3 methods are compared: conventional least square solution, least square solution with strain signal division, and least square solution with strain signal division and regularization scheme proposed in this research, where regularization factor α in Eq. (2.32) was adopted as 5.0×10^{-12}. Fig. 2.19 shows estimated strain and measured strain at validation sensor 16 and strain distribution on the deformed shape of each case under the regular wave condition (wave frequency = 0.95 Hz and wave amplitude = 100 mm).

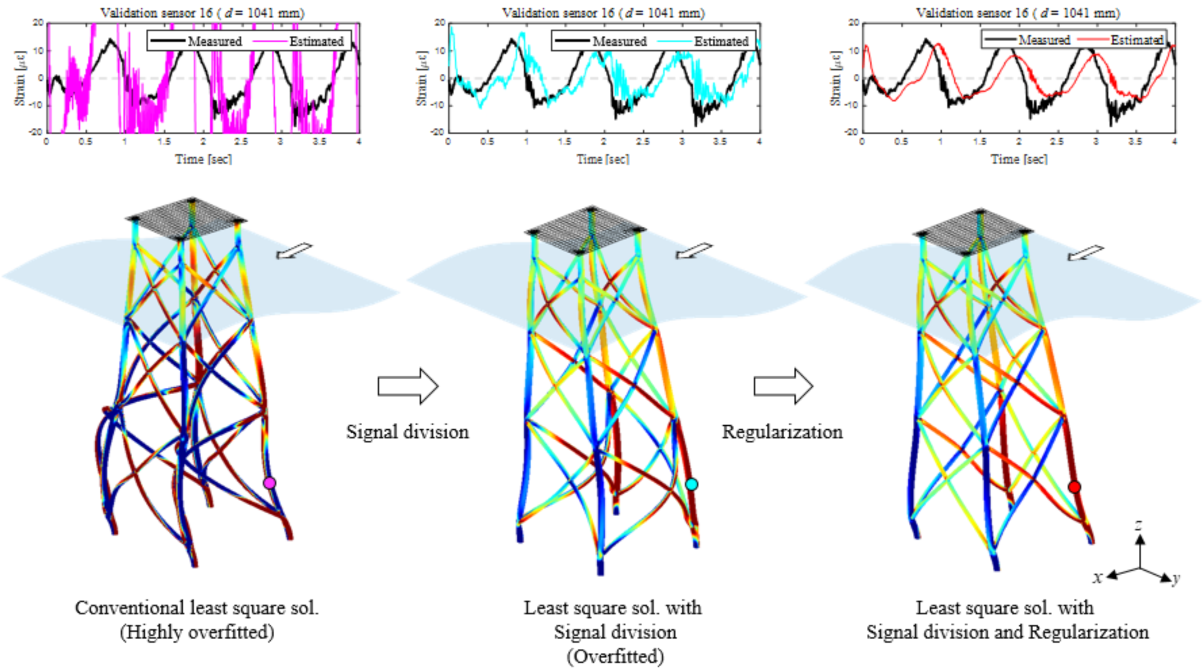

Figure 2.19: Effect of the regularization of generalized coordinates.

The result of virtual sensing with the proposed regularization scheme shows high estimation accuracy compared to others. Conventional least square solution makes estimated strain highly overfitted and strain signal division improves the estimation accuracy but estimation error still exists due to overfitting.

Unlike the numerical tests, less validation sensors were installed in the experiments compared to the numerical tests, making it difficult to use the evaluation measures in Eq. (2.33). Alternatives are local measures only at validation sensor points. The time response assurance criterion (TRAC), frequency response assurance criterion (FRAC), and maximum normalized relative error (MNRE) [3, 45, 77] can be adopted as

$$\mathrm{TRAC} = \frac{\left(\int_0^{4T} \varepsilon(t)e(t)dt\right)^2}{\left(\int_0^{4T} \varepsilon(t)^2 dt\right)\left(\int_0^{4T} e(t)^2 dt\right)}, \tag{2.34a}$$

$$\mathrm{FRAC} = \frac{\left(\int_0^{f_{\max}} \varepsilon(f)e(f)df\right)^2}{\left(\int_0^{f_{\max}} \varepsilon(f)^2 df\right)\left(\int_0^{f_{\max}} e(f)^2 dt\right)}, \tag{2.34b}$$

$$\mathrm{MNRE} = \frac{\int_0^{4T} \left|\varepsilon(t) - e(t)\right| dt}{4Te_{\max}} \times 100\% . \tag{2.34c}$$

In Eq. (2.34a), $\varepsilon(t)$ and $e(t)$ are the estimated and measured strains at a sensor in the time domain, respectively, and T is the wave period. In Eq. (2.34b), $\varepsilon(f)$ and $e(f)$ are the estimated and measured strains at a sensor in the frequency domain, respectively, and $f_{\max}$ is set to 80 Hz to avoid high-frequency noise from the measured strain signals. In Eq. (2.34c), $e_{\max}$ is the maximum value of the absolute strain measured during a 4 times period. TRAC and FRAC represent the similarity between the estimated and measured strain signals in the time domain and frequency domain, respectively. MNRE represents the amplitude error between both strain signals. When TRAC and FRAC are close to 1, and MNRE is close to 0, the estimated strain signal matches well with the measured strain signal.

Regular wave with 0.95 Hz frequency and amplitude of 100 mm are considered. The regularization of generalized coordinates is applied with the factor $\alpha = 5.0 \times 10^{-12}$. Fig. 2.20 shows the local measures for all validation sensors for the regular wave. The values of TRAC are relatively small at some sensors, but the values of FRAC are generally close to 1 at most of the sensors. This means that the estimated strain has a slight phase difference with respect to the measured strain, but the strain spectrum is very similar. The values of MNRE are less than 10 on average, meaning that the amplitude difference between the estimated and measured strain is less than 10%.

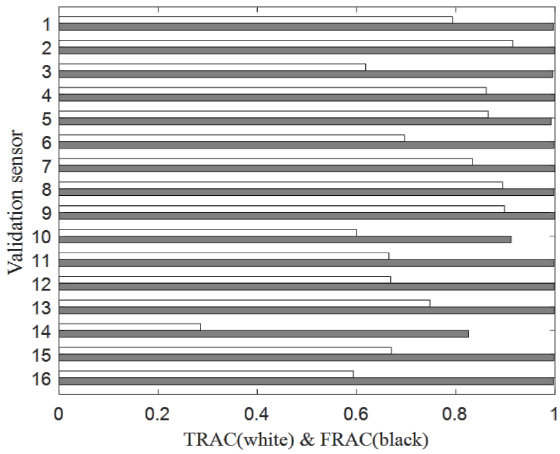

(a)

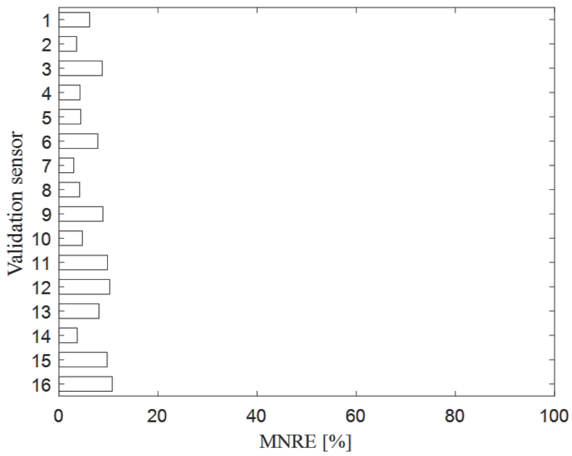

(b)

Figure 2.20: Local measures for all validation sensors for the regular wave: (a) TRAC and FRAC, (b) MNRE.

Figs. 2.21 and 2.22 show the estimated and measured strains at validation sensors for the regular wave, where the title of each graph denotes the water depth of its validation sensor. The estimated strains are in good agreement with the measured strains at all sensors, from the waterline to the bottom. With virtual sensing, strains in harsh regions such as deep water can be well approximated by placing several sensors only in dry regions above the waterline.

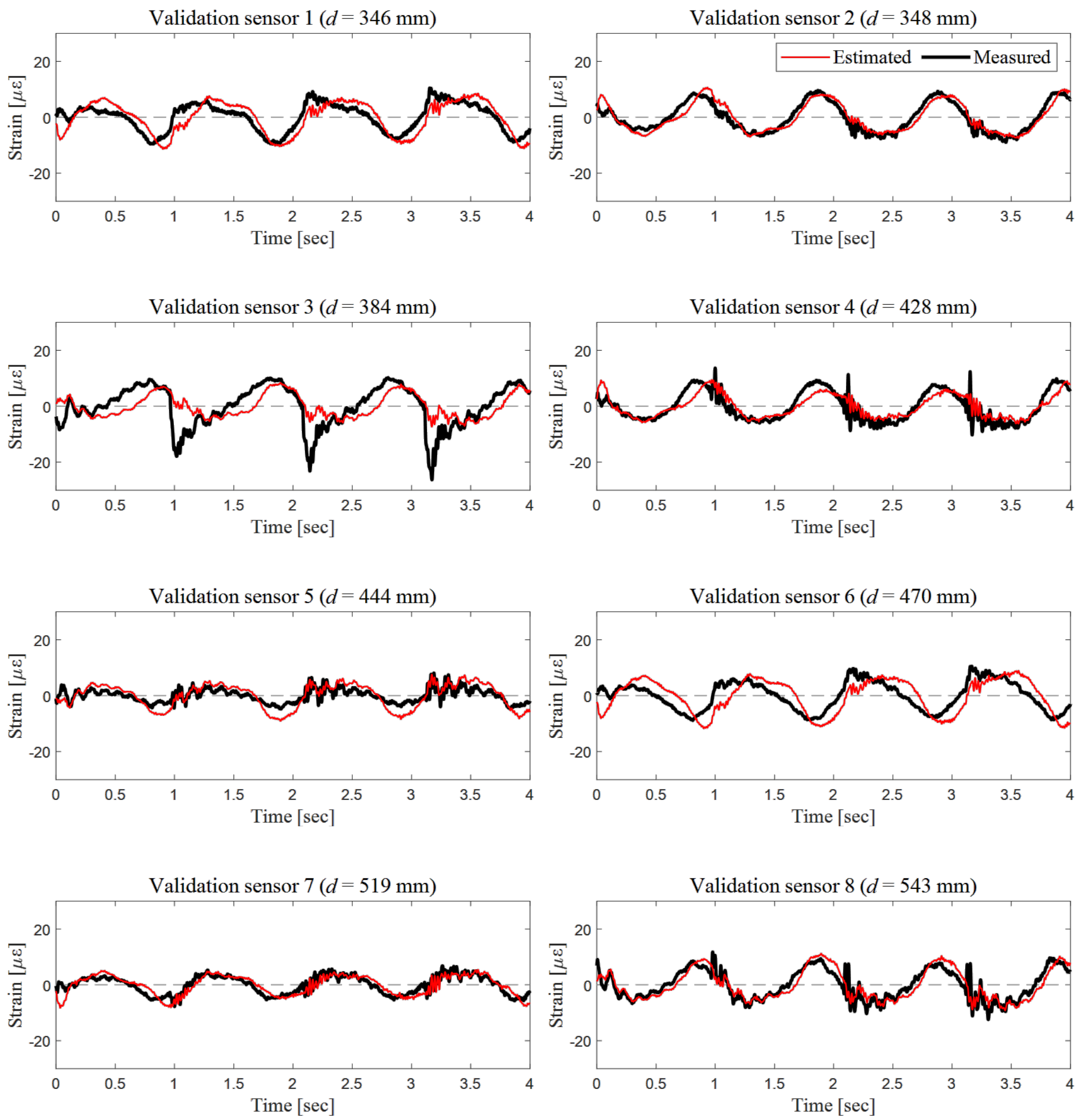

Figure 2.21: Estimated and measured strains at validation sensors from 1 to 8 for the regular wave.

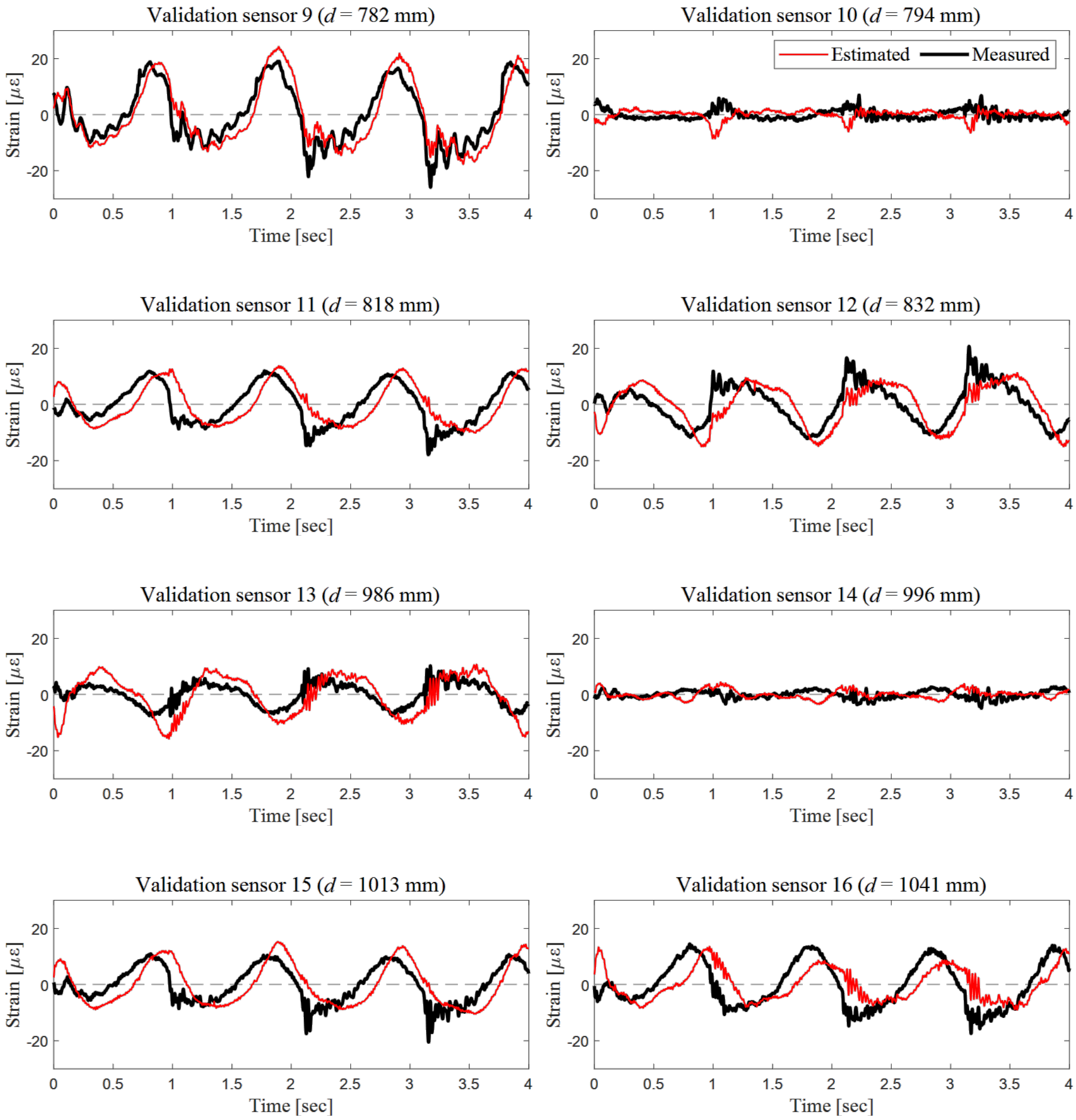

Figure 2.22: Estimated and measured strains at validation sensors from 9 to 16 for the regular wave.

We next consider irregular wave. The frequency and amplitude vary arbitrarily in the range of 0.8-1.25 Hz and 40-100 mm, respectively. The regularization of generalized coordinates is applied with the factor $\alpha = 5.0 \times 10^{-12}$. Fig. 2.23 shows the local measures for all validation sensors for the irregular wave. Similar to the regular wave case, the values of TRAC are relatively small at some validation sensors, but the values of FRAC are generally close to 1 at most of the sensors. The average value of MNRE is approximately 5. That is, the amplitude difference between the estimated and measured strain is about 5%.

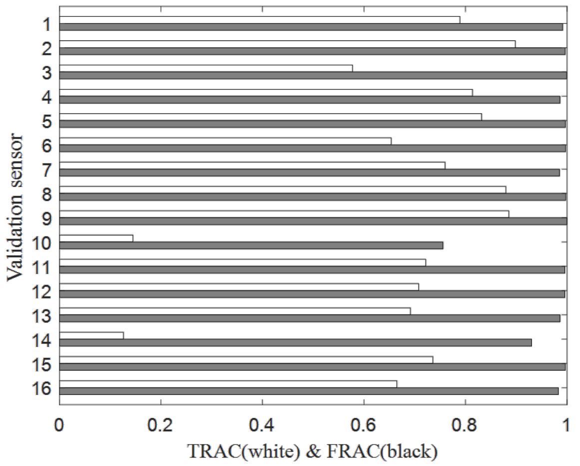

(a)

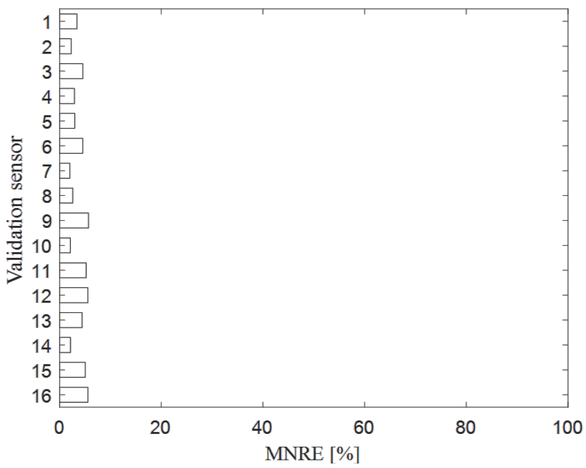

(b)

Figure 2.23: Local measures for all validation sensors for the irregular wave: (a) TRAC and FRAC, (b) MNRE.

Figs. 2.24 and 2.25 show the estimated and measured strains at the validation sensors for the irregular wave. The estimated strains are similar to the measured strains at all validation sensors positioned at different water depths. With virtual sensing, strains under water can be well approximated by placing several sensors only in dry regions above the waterline. Fig. 2.26 shows the axial strain contours normalized from -1 to 1 with their absolute maximum values on the deformed shapes at the moment of wave crest for the regular and irregular wave cases.

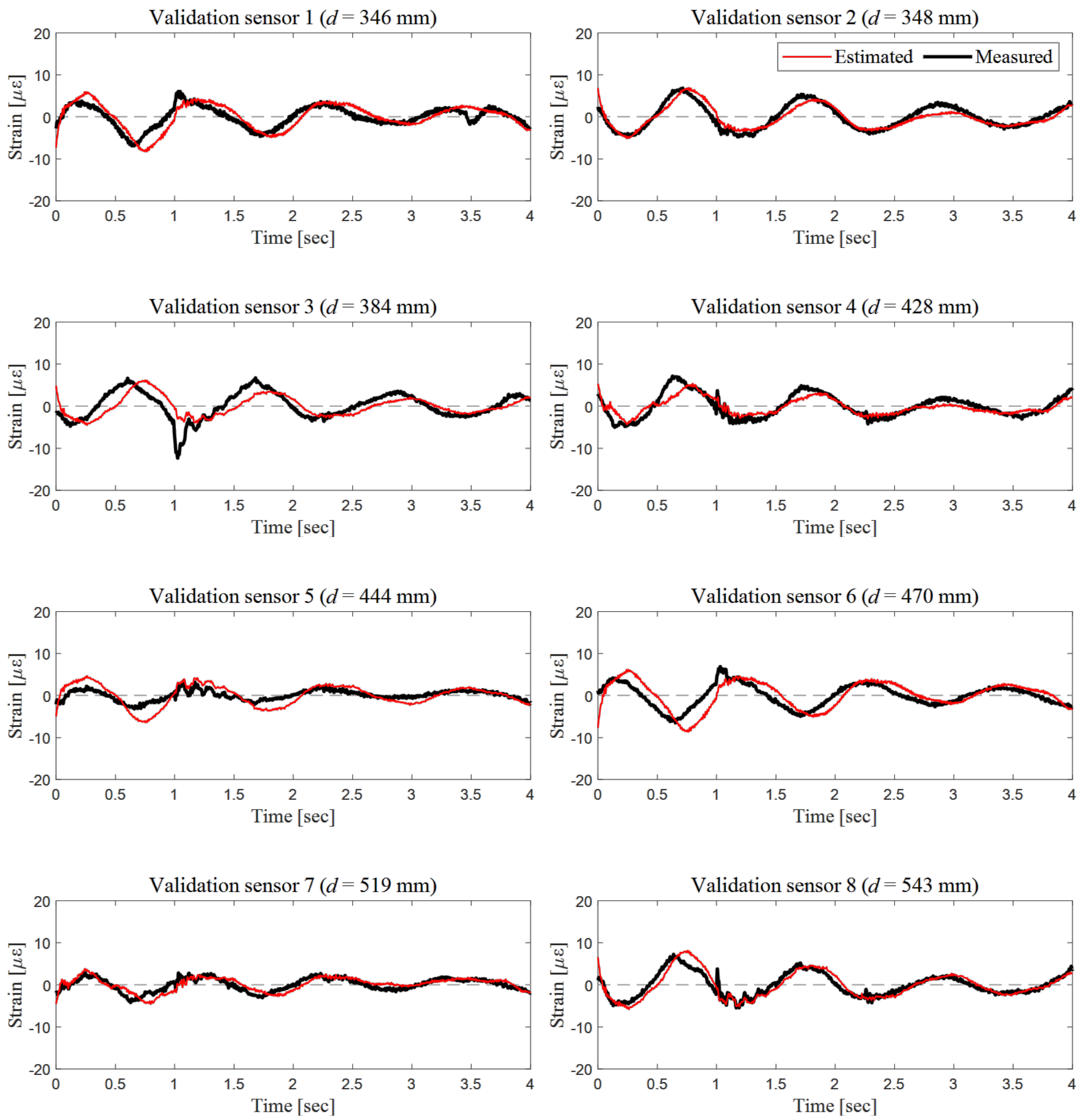

Figure 2.24: Estimated and measured strains at validation sensors from 1 to 8 for the irregular wave.

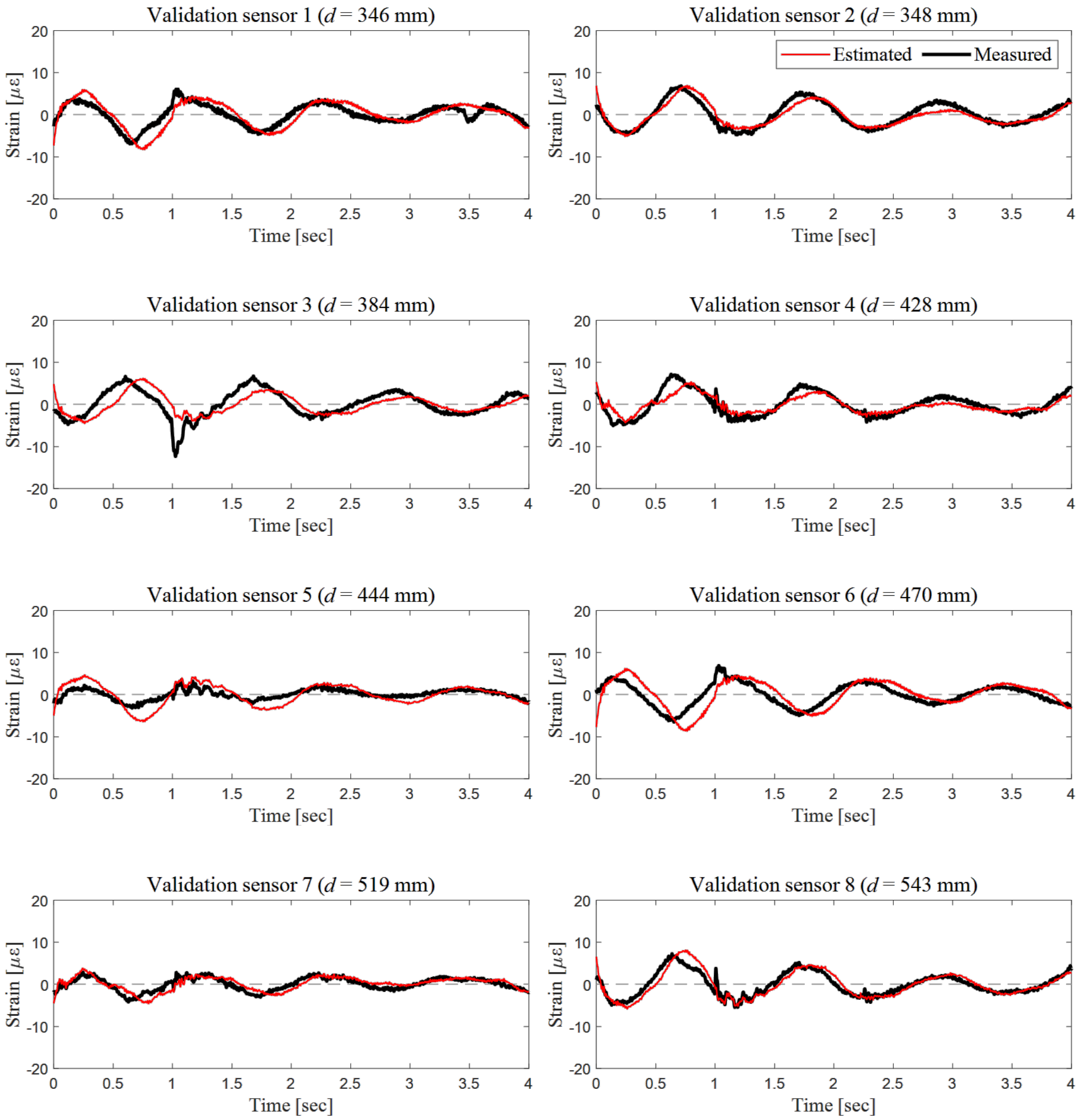

Figure 2.25: Estimated and measured strains at validation sensors from 9 to 16 for the irregular wave.

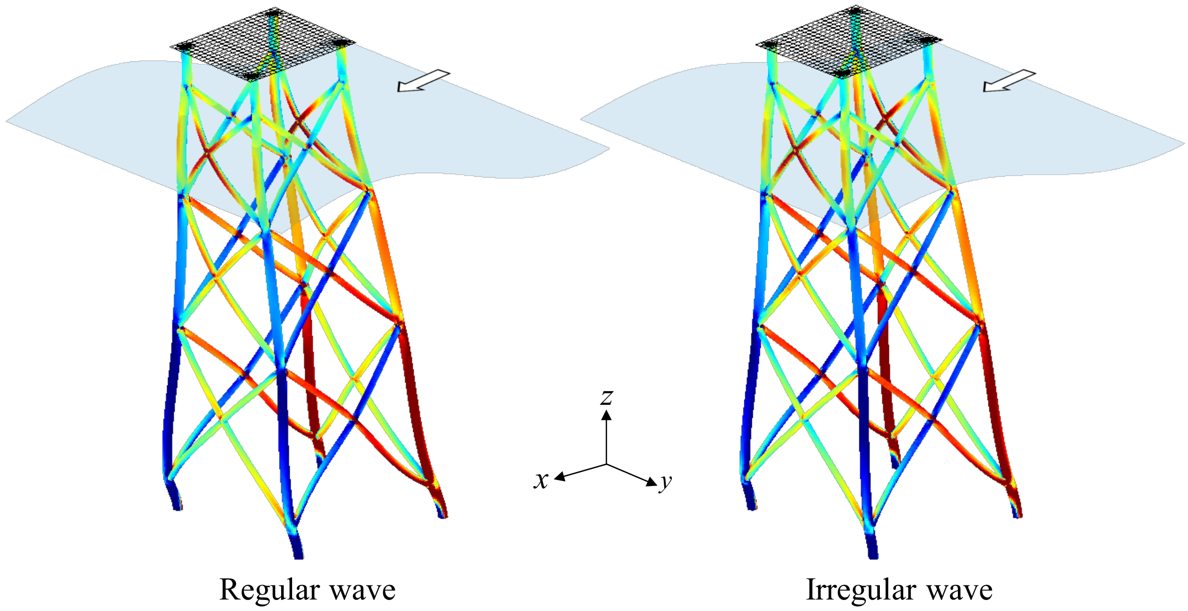

Figure 2.26: Normalized axial strain contours on the deformed shapes for the regular and irregular wave conditions at the moment of wave crest.

Through the experimental study considering the real deformation of the lab-scale jacket structure under waves, we demonstrated that the strain field is well estimated using a finite number of strain sensors with the virtual sensing methodology proposed in this study. Virtual sensing can be carried out nearly in real-time as the strain is measured in real-time and calculating generalized coordinates has very low computational cost. Calculation of the online process shown in Fig. 2.13 is performed about 970 times per second. In addition, the deformed shape and stress field can be also easily obtained from the strain estimation results.

2.6 Conclusions

In this Chapter, a comprehensive virtual sensing procedure for real-time strain field estimation of structures is presented utilizing the FE formulation. The strain-based transformation matrix is built relying on displacement modes and sensor placement. Signals measured at several strain gauges in real-time are used as input to estimate the full-field strain distribution in a structure. Quasi-static displacement modes under operational loads and free vibration modes are employed for the lab-scale jacket structure under water waves. The strain signals are divided into the corresponding quasi-static and free vibration parts and both parts are individually estimated. To avoid overfitting to the input strains, generalized coordinates are regularized. Numerical tests and dry condition tests were conducted, validating the feasibility of the proposed procedure. Experiments are performed in the ocean basin for the lab-scale jacket structure under water waves. Although various known and unknown disturbances exist in real wave experiments, strain fields have been well estimated.

In future works, the application of other displacement modes, such as POD modes, needs to be explored to cover various operating loads and increase versatility and estimation accuracy. Furthermore, it would be beneficial to study optimal sensor placements and utilize other sensor measurements, such as acceleration.

Chapter 3. Sensor placement for virtual sensing

3.1 Introduction

Virtual sensing is one of the key technologies for constructing structural digital twins, enabling the estimation of a structural response in unmeasured areas by utilizing data from measured areas [1-6]. This technology allows for the prediction of responses in locations that are difficult to measure. Additionally, it can estimate the response of the entire structure with a small number of sensors, reducing the need for extensive sensor networks. Virtual sensing enhances the ability to monitor and analyze structural health, making it an essential component in the development and operation of structural digital twins.

Virtual sensing based on the mode superposition method is simple in procedure and allows relatively accurate and stable deformation estimation with a small number of sensors [8]. The response of the structure measured from the sensors serves as a link between the real structure and its corresponding numerical model, the digital twin of the structure. The accuracy of virtual sensing depends on the number, positions, and orientations of the sensors, and thus proper sensor placement is essential in virtual sensing [17-19].

Conventionally, sensor placement methods have been developed for modal testing considering the contribution of the basis vectors, independency of the basis vectors, and redundancy of the measurement responses. The methods considering contribution of basis vectors include Average Driving Point Residue (ADPR) [78, 79], and Eigenvlaue Vector Product (EVP) [78-80] and the methods considering independency include Effective independence (EfI) [81] and minimum Condition Number (CN) [24, 82, 83] to minimize the redundancy of measurement responses.

Conventional sensor placement methods consider only the properties of the basis vectors, resulting in inconsistent performance depending on the structure type, operational loads, and sensor installation conditions. These methodologies fail to provide specific guidelines for determining the necessary number of basis vectors and sensors, despite these being crucial factors in sensor placement. Developing a new method that determines the number of basis vectors and sensors to ensure accurate virtual sensing, regardless of the given problem conditions, is a challenging task.

The key idea of this study is to consider the operational loads of a structure in the procedure of the strain sensor placement. First, we present a procedure for determining the number of basis vectors. The target strain fields corresponding to the operational loads of the structure are calculated using a finite element model, and then the number of basis vectors is determined so that the accuracy of virtual sensing becomes larger than a target accuracy. We next propose a method for determining sensor placement considering both operational loads and truncation error. A number of sensors are initially placed in the desired area of the structure, where the locations and directions of the sensors are considered. Among the sensors, the sensors that can estimate target strain field with low error using the given basis vectors are selected as candidates. Increasing the number of sensors, estimation error is evaluated until the error becomes less than a target error. In addition, condition number is considered to avoid selecting sensors that are too close to each other. The proposed sensor placement procedure provides consistently good virtual sensing accuracy regardless of structural types, operational loads, sensor installation conditions and so on.

Chapter 3 is organized as follows: Section 3.2 introduces the virtual sensing formulation based on mode superposition method, and Section 3.3 describes the method to calculate the target strain of the operational loads. Section 3.4 presents the procedure for determining the number of basis vectors and a novel sensor placement method with a proper number of sensors, and Section 3.5 describes existing sensor placement methods. Section 3.6 demonstrates the performance of the proposed method by various numerical examples. Conclusions are drawn in Section 3.7.

3.2 Mode-based virtual sensing

In this section, a virtual sensing method based on mode superposition method is utilized [8]. Although the mode superposition method causes truncation error, it has the advantage that operational loads and characteristics of the structure can be considered when selecting the basis vectors. In addition, the target performance of virtual sensing can be obtained with a relatively small number of sensors. The response of the structure for virtual sensing is strain measurement data. Strain measurement systems are relatively inexpensive and do not affect the structural characteristics such as stiffness and mass due to sensor attachment.

Let us consider a FE model with N DOFs (Degree Of Freedoms) corresponding to a real structure subjected to operational loads, as shown in Fig. 3.1. The FE model consists of a stiffness matrix $\mathbf{K}$, a mass matrix $\mathbf{M}$, and a damping matrix $\mathbf{C}$. The behavior of the structure is represented by the following equation

$$\mathbf{M}\ddot{\mathbf{U}} + \mathbf{C}\dot{\mathbf{U}} + \mathbf{K}\mathbf{U} = \mathbf{R}, \tag{3.1}$$

where $\mathbf{U} = \mathbf{U}(t)$ with time t, $\dot{\mathbf{U}} = d\mathbf{U}/dt$, and $\ddot{\mathbf{U}} = d^2\mathbf{U}/dt^2$ are nodal displacement, nodal velocity, and nodal acceleration vectors, respectively, and $\mathbf{R} = \mathbf{R}(t)$ is the external load vector.

We define a strain vector that represents the strain at a location $\mathbf{x} = [x \quad y \quad z]^{\mathrm{T}}$ on the structure. $\mathbf{x}$ belongs to element m of the FE model, and its corresponding natural coordinates are (r, s, t),

$$\begin{aligned}\boldsymbol{\varepsilon}^{(m)}(r,s,t) &= \begin{bmatrix}\varepsilon_{xx} & \varepsilon_{yy} & \varepsilon_{zz} & \gamma_{xy} & \gamma_{yz} & \gamma_{zx}\end{bmatrix}^{\mathrm{T}} \\ &= \mathbf{B}^{(m)}(r,s,t)\mathbf{u}^{(m)} = \mathbf{B}^{(m)}(r,s,t)\mathbf{L}^{(m)}\mathbf{U},\end{aligned} \tag{3.2}$$

in which $\mathbf{B}^{(m)}$ is a strain-displacement matrix of element m, $\mathbf{u}^{(m)}$ is a nodal displacement vector of the element, and $\mathbf{L}^{(m)}$ is a Boolean matrix relating $\mathbf{u}^{(m)}$ and $\mathbf{U}$.

The normal strain in the direction $\mathbf{n}$ at a point $\mathbf{x}$ on the structure is calculated by

$$\varepsilon(\mathbf{x},\mathbf{n}) = \mathbf{Q}(\mathbf{n})\boldsymbol{\varepsilon}^{(m)}(r,s,t) = \mathbf{Q}(\mathbf{n})\mathbf{B}^{(m)}(r,s,t)\mathbf{u}^{(m)} = \mathbf{Q}(\mathbf{n})\mathbf{B}^{(m)}(r,s,t)\mathbf{L}^{(m)}\mathbf{U}, \tag{3.3}$$

where $\mathbf{Q}$ is a matrix that calculates the normal strain in the $\mathbf{n}$ direction from the strain vector $\boldsymbol{\varepsilon}^{(m)}$.

The mode superposition method approximates the nodal displacement vector $\mathbf{U}$ having N DOFs in Eq. (3.1) as a linear combination of $\bar{N}$ displacement basis vectors $\mathbf{\Phi}_i$ ($\bar{N} \ll N$)

$$\mathbf{U} \approx \mathbf{\Phi}_1 q_1 + \mathbf{\Phi}_2 q_2 + \cdots + \mathbf{\Phi}_{\bar{N}} q_{\bar{N}} = \mathbf{\Phi q}, \tag{3.4a}$$

with

$$\mathbf{\Phi} = [\mathbf{\Phi}_1 \quad \mathbf{\Phi}_2 \quad \ldots\ldots \quad \mathbf{\Phi}_{\bar{N}}] \text{ and } \mathbf{q} = \begin{bmatrix} q_1 & q_2 & \ldots\ldots & q_{\bar{N}} \end{bmatrix}^{\mathrm{T}}, \tag{3.4b}$$

where $\mathbf{\Phi}$ is the displacement basis matrix and $\mathbf{q}$ is the generalized coordinate vector.

Substituting Eq. (3.4) to Eq. (3.3), the normal strain $\varepsilon(\mathbf{x},\mathbf{n})$ at a point $\mathbf{x}$ belonging to element m is expressed using the generalized coordinate vector as

$$\varepsilon(\mathbf{x},\mathbf{n}) \approx \mathbf{Q}(\mathbf{n})\left(\mathbf{\Psi}_1^{(m)} q_1 + \mathbf{\Psi}_2^{(m)} q_2 + \cdots + \mathbf{\Psi}_{\bar{N}}^{(m)} q_{\bar{N}}\right) = \mathbf{Q}(\mathbf{n})\mathbf{\Psi}^{(m)}\mathbf{q} \tag{3.5a}$$

with

$$\mathbf{\Psi}_i^{(m)}(r,s,t) = \mathbf{B}^{(m)}(r,s,t)\mathbf{L}^{(m)}\mathbf{\Phi}_i, \quad \mathbf{\Psi}^{(m)}(r,s,t) = \mathbf{B}^{(m)}(r,s,t)\mathbf{L}^{(m)}\mathbf{\Phi},$$

$$\mathbf{\Psi}^{(m)} = [\mathbf{\Psi}_1^{(m)} \quad \mathbf{\Psi}_2^{(m)} \quad \ldots\ldots \quad \mathbf{\Psi}_{\bar{N}}^{(m)}], \tag{3.5b}$$

where $\mathbf{\Psi}^{(m)}$ is the strain basis matrix consisting of the strain basis vectors $\mathbf{\Psi}_i^{(m)}$. The number of strain basis vectors is equal to the number of displacement basis vectors, $\bar{N}$.

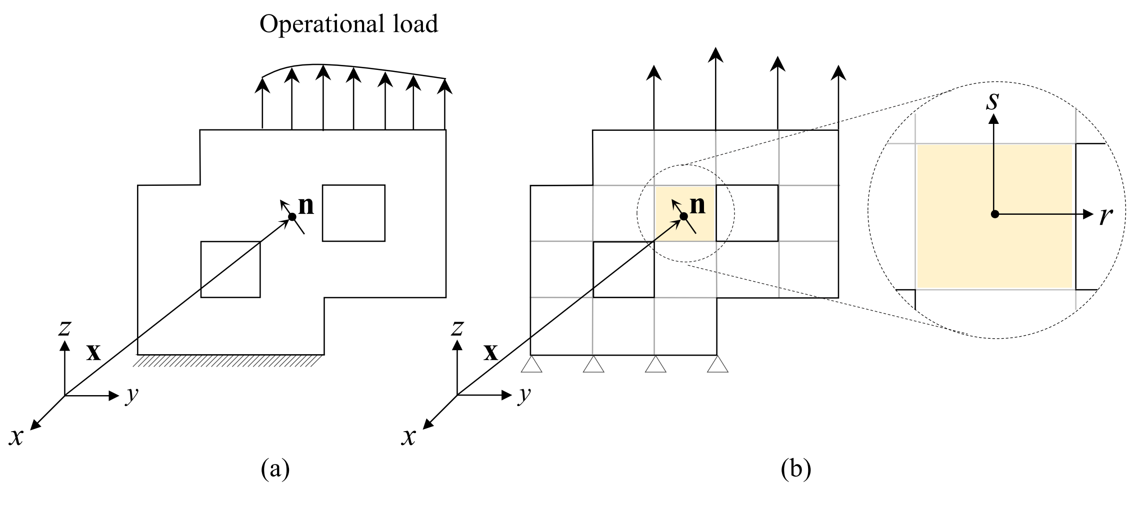

Figure 3.1: Construction of the strain mode matrix: (a) Arbitrary structure under its operational load, (b) Corresponding FE model with idealized load and boundary conditions.

Let us define M measured normal strains $e(\mathbf{x}_i, \mathbf{n}_i)$ shown in Fig. 3.2 as a measured strain vector

$$\mathbf{e}_{\text{inp}} = \begin{bmatrix} e_1 \\ e_2 \\ \vdots \\ e_M \end{bmatrix} \quad \text{with} \quad e_i = e(\mathbf{x}_i, \mathbf{n}_i), \tag{3.6}$$

where $\mathbf{x}_i$ and $\mathbf{n}_i$ corresponds to ith sensor position and measurement direction, respectively.

Using Eq. (3.5) with $\bar{N}$ strain basis vectors, the estimated strain vector corresponding to the measured strain vector in Eq. (3.6) is defined by

$$\boldsymbol{\varepsilon}_{\text{inp}} = \begin{bmatrix} \varepsilon_1 \\ \varepsilon_2 \\ \vdots \\ \varepsilon_M \end{bmatrix} \quad \text{with} \quad \varepsilon_i = \varepsilon(\mathbf{x}_i, \mathbf{n}_i) \approx \mathbf{Q}(\mathbf{n}_i)\boldsymbol{\Psi}^{(m_i)}(r_i, s_i, t_i)\mathbf{q}, \tag{3.7}$$

in which ε_i is the estimated normal strain at ith sensor among M strain sensors.

The measured strain vector $\mathbf{e}_{\text{inp}}$ in Eq. (3.6) is approximated by the estimated strain vector $\boldsymbol{\varepsilon}_{\text{inp}}$ in Eq. (3.7) as

$$\mathbf{e} \approx \boldsymbol{\varepsilon} = \mathbf{T}\mathbf{q} \tag{3.8a}$$

$$\text{with} \quad \mathbf{T} = \begin{bmatrix} \mathbf{T}_1(\mathbf{x}_1, \mathbf{n}_1) \\ \mathbf{T}_2(\mathbf{x}_2, \mathbf{n}_2) \\ \vdots \\ \mathbf{T}_M(\mathbf{x}_M, \mathbf{n}_M) \end{bmatrix} = \begin{bmatrix} \mathbf{Q}(\mathbf{n}_1)\boldsymbol{\Psi}^{(m_1)}(r_1, s_1, t_1) \\ \mathbf{Q}(\mathbf{n}_2)\boldsymbol{\Psi}^{(m_2)}(r_2, s_2, t_2) \\ \vdots \\ \mathbf{Q}(\mathbf{n}_M)\boldsymbol{\Psi}^{(m_M)}(r_M, s_M, t_M) \end{bmatrix}, \tag{3.8b}$$

$\mathbf{T}$ is a transformation matrix which transform the generalized coordinate vector to estimated strain vector, and ith row of $\mathbf{T}$ corresponds to ith sensor.

The difference between two vectors $\boldsymbol{\varepsilon}_{\text{inp}}$ and $\mathbf{e}_{\text{inp}}$ can be measured by

$$C = \sum_{i=1}^{M} \left(\varepsilon_i - e_i\right)^2 = (\boldsymbol{\varepsilon}_{\text{inp}} - \mathbf{e}_{\text{inp}})^{\mathrm{T}} (\boldsymbol{\varepsilon}_{\text{inp}} - \mathbf{e}_{\text{inp}})$$

$$= (\mathbf{Tq} - \mathbf{e}_{\text{inp}})^{\mathrm{T}} (\mathbf{Tq} - \mathbf{e}_{\text{inp}}) \tag{3.9}$$

and the vector of least square solution $\mathbf{q}'$ that minimizes C is calculated as

$$\mathbf{q}' = (\mathbf{T}^{\mathrm{T}}\mathbf{T})^{-1}\mathbf{T}^{\mathrm{T}}\mathbf{e}_{\text{inp}} \, . \tag{3.10}$$

Finally, the displacement field, strain field, and stress field for the entire area of the structure can be estimated by substituting $\mathbf{q}'$ into Eq. (3.4)

$$\mathbf{U} \approx \mathbf{\Phi q}' , \tag{3.11a}$$

$$\boldsymbol{\varepsilon}^{(m)}(r,s,t) \approx \mathbf{\Psi}^{(m)}\mathbf{q}' , \tag{3.11b}$$

$$\boldsymbol{\sigma}^{(m)}(r,s,t) \approx \mathbf{C\Psi}^{(m)}\mathbf{q}' \quad \text{with} \quad \boldsymbol{\sigma} = \begin{bmatrix} \sigma_{xx} & \sigma_{yy} & \sigma_{zz} & \sigma_{xy} & \sigma_{yz} & \sigma_{zx} \end{bmatrix}^{\mathrm{T}} , \tag{3.11c}$$

in which $\boldsymbol{\sigma}$ is the stress vector and $\mathbf{C}$ is the material law matrix.

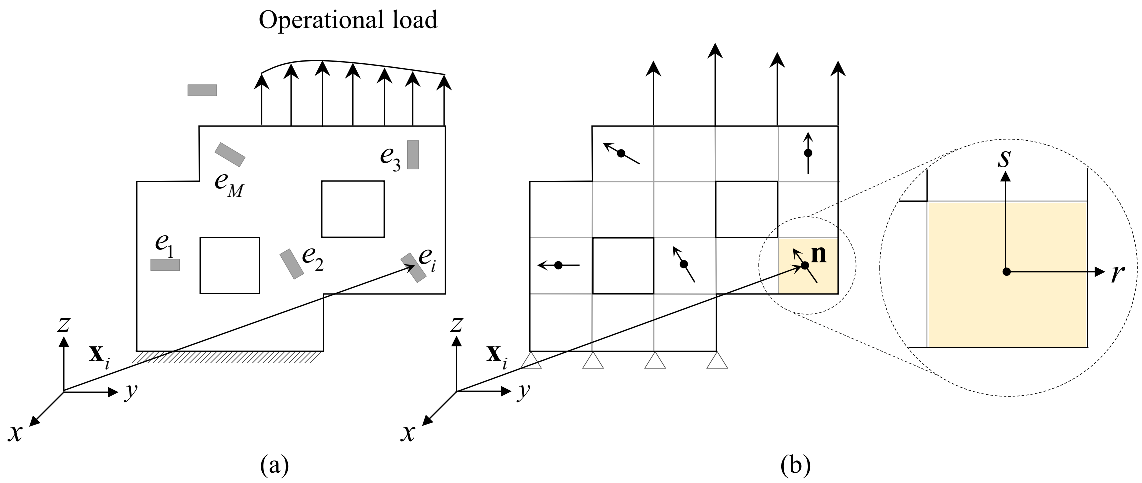

Figure 3.2: Normal strains measured and estimated: (a) Strain sensors attached on the surface of the structure, (b) Estimated strains on the corresponding FE model.

3.3 Operational loading and target response

In the mode-based virtual sensing, the number of displacement (or strain) basis vectors and the number of input sensors are important factors that affect the accuracy and the extent of overfitting of estimation. Conventional sensor placement methods have a limitation in that they do not provide any guidelines for determining the numbers of basis vectors and sensors. In addition, existing sensor placement methods only consider the geometry and dynamic characteristics of the structure to place input sensors without considering the operational loads.

Typically, structures are subjected to a combination of operational loads that are specific to their design role. Therefore, considering operational loads can lead to more effective basis selection and sensor placement. In this study, we calculate target strain fields for operational loads and use them to determine the number of basis vectors, and sensor locations and directions with the proper number of sensors.

We assume that the operational loads acting on a structure is a linear combination of K harmonic loads

$$\mathbf{R}(t) = \sum_{i=1}^{K} \mathbf{R}_i(t) = \sum_{i=1}^{K} w_i \mathbf{R}_i \sin(2\pi\Omega_i t + \alpha_i) h_i(t) \tag{3.12}$$

with a step function $h_i(t) = h(t - t_i) = \begin{cases} 1 & \text{for} \quad t \geq t_i \\ 0 & \text{for} \quad t < t_i \end{cases}$

where t is time, t_i is the time when load is applied, w_i, α_i, and Ω_i are magnitude, phase, and excitation frequency of the ith load, and $\mathbf{R}_i$ is a load distribution vector.

Let us consider the FE model in Eq. (3.1). The response of the structure to K loads can be represented by

$$\mathbf{U}(t) = \sum_{i=1}^{K} w_i \mathbf{U}_i \cos(2\pi\Omega_i t + \beta_i) \quad \text{with} \quad \mathbf{U}_i = (\mathbf{K} - \Omega_i^2 \mathbf{M})^{-1} \mathbf{R}_i , \tag{3.13}$$

where $\mathbf{U}_i$ is the frequency response corresponding to $\mathbf{R}_i$, and β_i represents the phase shift due to damping. That is, the displacement of the structure consists of a linear combination of the frequency response by the ith load distribution $\mathbf{R}_i$.

The basis vectors and sensors placement that can approximate each $\mathbf{U}_i$ with high accuracy will also describe the overall behavior of the structure well. We here define the target normal strain for the *i*th load $\mathbf{R}_i$ in the direction $\mathbf{n}$ at a point $\mathbf{x}$ by substituting the *i*th frequency response $\mathbf{U}_i$ into Eq. (3.3)

$$\varepsilon^{(i)}(\mathbf{x},\mathbf{n}) = \mathbf{Q}(\mathbf{n})\mathbf{B}^{(m)}(r,s,t)\mathbf{L}^{(m)}\mathbf{U}_i \,. \tag{3.14}$$

3.4 Sensor placement considering operational loads

For virtual sensing, the position and direction of the M strain sensors in Eq. (6) need to be determined. In general, the larger the number of basis vectors and sensors used, the higher the estimation accuracy, but the number of sensors is limited due to the cost of sensor installation and maintenance. In addition, overfitting may occur depending on the relationship between the number of basis vectors and sensors, and the accuracy of virtual sensing depends on the sensor placement; thus; the number and placement of sensors should be determined carefully.

Let us consider a structure with input sensors and virtual sensors attached to it, as shown in Fig. 3.3 The total number of sensors is L, of which M is the number of input sensors and $(L-M)$ are virtual sensors. The normal strain measured at the input sensors are used to estimate the normal strain at the virtual sensors. Let L be a finite number that is much larger than M ($L >> M$).

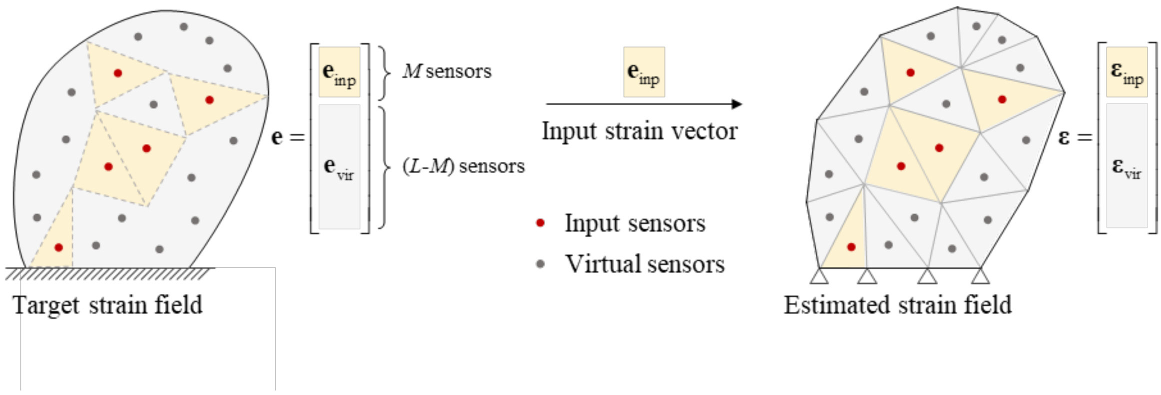

Figure 3.3: Description of input sensors and virtual sensors on the structure and corresponding FE model.

Let us use the target strains calculated in Section 3.3 instead of the actual measured strains and define the target strain vector for the ith load as

$$\mathbf{e}^{(i)} = \begin{bmatrix} \mathbf{e}_{\text{inp}}^{(i)} \\ \mathbf{e}_{\text{vir}}^{(i)} \end{bmatrix} \quad \text{with} \quad \mathbf{e}_{\text{inp}}^{(i)} = \begin{bmatrix} e_1^{(i)} \\ e_2^{(i)} \\ \vdots \\ e_M^{(i)} \end{bmatrix}, \ \mathbf{e}_{\text{vir}}^{(i)} = \begin{bmatrix} e_{M+1}^{(i)} \\ e_{M+2}^{(i)} \\ \vdots \\ e_L^{(i)} \end{bmatrix}, \tag{3.15}$$

where $\mathbf{e}_{\text{inp}}^{(i)}$ and $\mathbf{e}_{\text{vir}}^{(i)}$ are target normal strain vectors at input sensors and virtual sensors, respectively.

The target strain vector for the ith load can be estimated at all sensors using Eq. (10) with $\bar{N}$ modes and M input sensors

$$\boldsymbol{\varepsilon}^{(i)} = \begin{bmatrix} \boldsymbol{\varepsilon}_{\text{inp}}^{(i)} \\ \boldsymbol{\varepsilon}_{\text{vir}}^{(i)} \end{bmatrix} = \begin{bmatrix} \mathbf{T}_{\text{inp}} \\ \mathbf{T}_{\text{vir}} \end{bmatrix} \mathbf{q}^{(i)} \tag{3.16a}$$

with

$$\mathbf{q}^{(i)} = (\mathbf{T}_{\text{inp}}^{\text{T}} \mathbf{T}_{\text{inp}})^{-1} \mathbf{T}_{\text{inp}}^{\text{T}} \mathbf{e}_{\text{inp}}^{(i)}, \quad \boldsymbol{\varepsilon}_{\text{inp}}^{(i)} = \begin{bmatrix} \varepsilon_1^{(i)} \\ \varepsilon_2^{(i)} \\ \vdots \\ \varepsilon_M^{(i)} \end{bmatrix}, \quad \boldsymbol{\varepsilon}_{\text{vir}}^{(i)} = \begin{bmatrix} \varepsilon_{M+1}^{(i)} \\ \varepsilon_{M+2}^{(i)} \\ \vdots \\ \varepsilon_L^{(i)} \end{bmatrix}, \tag{3.16b}$$

where $\boldsymbol{\varepsilon}_{\text{inp}}^{(i)}$ and $\boldsymbol{\varepsilon}_{\text{vir}}^{(i)}$ are estimated normal strain vectors at input sensors and virtual sensors, respectively.

The errors at all sensors, the difference between the estimated strain vector obtained by virtual sensing and the target strain vector for the K loads considered, can be represented by

$$\mathrm{E}_{\text{all}} = \frac{1}{K} \sum_{i=1}^{K} s_i \frac{\left\| \boldsymbol{\varepsilon}^{(i)} - \mathbf{e}^{(i)} \right\|}{\left\| \mathbf{e}^{(i)} \right\|} \quad \text{with} \quad \frac{1}{K} \sum_{k=1}^{K} s_k = 1, \tag{3.17}$$

where s_k represents the weight of each load based on its importance. Note that Eq. (17) considers errors not only at the input sensors but also at the virtual sensors.

3.4.1 Number of displacement basis modes

In order to perform virtual sensing, it is necessary to determine the type and number of displacement basis in Eq. (3.4) and the locations and directions of the input sensors in Eq. (3.6). In this study, the free vibration mode of the structure is used as the displacement basis. Free vibration modes, static deformation shapes, and POD displacements for the operational loads can be utilized as displacement basis [45, 57, 58, 83].

When a number of basis is given, the error calculated by Eq. (3.17) becomes smaller and smaller as the number of input sensors in Eq. (3.15) increases. When all L sensors are used as input sensors $(M = L)$, the error in Eq. (3.17) is minimized

$$\mathrm{E}_{\min} = \frac{1}{K}\sum_{i=1}^{K}\frac{\left\|\bar{\boldsymbol{\varepsilon}}_{\mathrm{inp}}^{(i)} - \bar{\mathbf{e}}_{\mathrm{inp}}^{(i)}\right\|}{\left\|\bar{\mathbf{e}}_{\mathrm{inp}}^{(i)}\right\|} \tag{3.18}$$

with

$$\bar{\mathbf{e}}^{(i)} = \bar{\mathbf{e}}_{\mathrm{inp}}^{(i)} = \begin{bmatrix} e_1^{(i)} \\ e_2^{(i)} \\ \vdots \\ e_L^{(i)} \end{bmatrix}, \quad \bar{\boldsymbol{\varepsilon}}^{(i)} = \bar{\boldsymbol{\varepsilon}}_{\mathrm{inp}}^{(i)} = \begin{bmatrix} \varepsilon_1^{(i)} \\ \varepsilon_2^{(i)} \\ \vdots \\ \varepsilon_L^{(i)} \end{bmatrix} = \bar{\mathbf{T}}_{\mathrm{inp}}\bar{\mathbf{q}}^{(i)}, \quad \bar{\mathbf{q}}^{(i)} = (\bar{\mathbf{T}}_{\mathrm{inp}}^{\mathrm{T}}\bar{\mathbf{T}}_{\mathrm{inp}})^{-1}\bar{\mathbf{T}}_{\mathrm{inp}}^{\mathrm{T}}\bar{\mathbf{e}}_{\mathrm{inp}}^{(i)},$$

where $\bar{\boldsymbol{\varepsilon}}^{(i)}$ is defined as the reference strain vector for the *i*th load.

Using Eq. (3.18), we determine the proper number of displacement basis vectors $\bar{N}^*$ satisfying the following equation

$$\mathrm{E}_{\min}(\bar{N}) \le \mathrm{E}_{\mathrm{trun}} \tag{3.19}$$

where $\mathrm{E}_{\mathrm{trun}}$ denotes the target truncation error of the estimated strain field of Eq. (3.17), determined by users.

Fig. 3.4(a) shows the change of $\mathrm{E}_{\min}$ with increasing the number of basis vectors as an example. As the number of basis vectors $\bar{N}$ increases, the truncation error decreases and thus $\mathrm{E}_{\min}$ becomes progressively smaller. In this example, the smallest number of basis vector for which $\mathrm{E}_{\min}$ is less than $\mathrm{E}_{\mathrm{trun}}$ is 6. Therefore, $\bar{N}^*$ is determined by a number greater than or equal to 6.

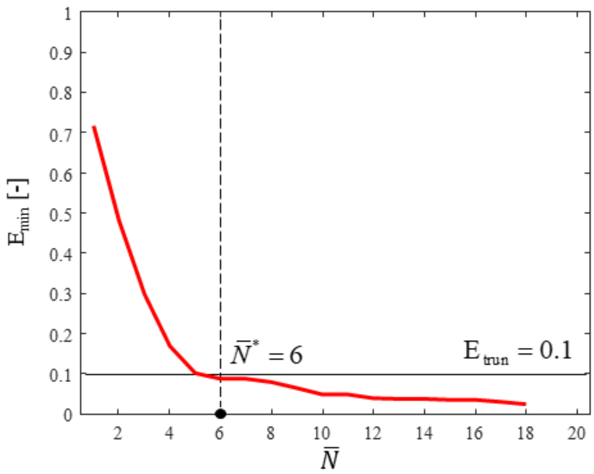

Figure 3.4: Examples of minimum estimation error according to number of basis vectors with $\mathrm{E}_{\mathrm{trun}}$ for the determination of numbers of basis vectors.

3.4.2 Selection of input sensors

In this section, we propose a method for sensor placement for more accurate virtual sensing by utilizing the target strain field obtained from the operational loads of a structure. Since the existing sensor placement method determines the sensor placement by considering only the characteristics of the basis vectors without considering the operational loads, the accuracy of virtual sensing may be low in some cases, i.e., there is a problem of inconsistency in which the accuracy of virtual sensing varies depending on the virtual sensing conditions and the structure. Considering operational loads can find more suitable sensor placement to improve the accuracy and robustness of the virtual sensing.

For the proper virtual sensing of the entire area of the structure, it is necessary to avoid overfitting and thus the number of input sensors (M) need be sufficiently larger than the number of basis vectors $(\bar{N}^* < M)$ [80, 82].

All of the L virtual sensors are considered the initially located sensors. The relative error E_j, which represents the difference between the reference strain $\bar{\varepsilon}_j^{(i)}$ (jth component of the reference strain vector $\bar{\boldsymbol{\varepsilon}}^{(i)}$) and the target strain $e_j^{(i)}$ (jth component of target strain vector $\mathbf{e}^{(i)}$) for all operational loads ($i = 1$ to K) for the jth sensor, can then be defined as

$$\mathrm{E}_j = \sum_{i=1}^{K} s_i \left| \frac{\bar{\varepsilon}_j^{(i)} - e_j^{(i)}}{\bar{\varepsilon}_j^{(i)}} \right|, \tag{3.20}$$

where normalization with the reference strain removes the effect of strain magnitude.

The better the input sensor can represent the target strain field with the $\bar{N}^*$ basis vectors selected by the procedure described in Section 4.1, the smaller the value of E_j will be. This characteristic can be used to select a candidate sensor group from the initial sensors. The sensors whose relative error is smaller than $\mathrm{E}_{\mathrm{cand}}$ belong to the candidate group for the final sensor selection

$$\mathrm{E}_j = \sum_{i=1}^{K} s_i \left| \frac{\bar{\varepsilon}_j^{(i)} - e_j^{(i)}}{\bar{\varepsilon}_j^{(i)}} \right| \le \mathrm{E}_{\mathrm{cand}}, \tag{3.21}$$

where $\mathrm{E}_{\mathrm{cand}}$ is the target relative error in selecting sensors. $\mathrm{E}_{\mathrm{cand}}$ needs to be determined so that number of candidate sensors (P) is sufficiently larger than the required number of input sensors and candidate sensors are widely distributed for the entire region.

We initially set the number of input sensors M to $\bar{N}^* + 1$. Among the P candidate sensors, the combination that minimizes the condition number of $\mathbf{T}^{\mathrm{T}}\mathbf{T}$ in Eq. (3.16) determines M input sensors [24, 82] and evaluates the estimation error $\mathrm{E}_{\mathrm{all}}$ in Eq. (3.17). If M input sensors satisfy the following condition

$$\mathrm{E}_{\mathrm{all}}(M) \le \mathrm{E}_{\mathrm{trun}}, \tag{3.22}$$

the currently selected input sensors become the final; otherwise, the above process is repeated by increasing the number of input sensors one by one.

If Eq. (22) is satisfied, it means that no overfitting occurred in the strain field estimation; that is, because $\mathrm{E}_{\mathrm{all}}$ by the selected M input sensors is as sufficiently small as $\mathrm{E}_{\mathrm{min}}$, the minimum error that the given basis can have, strain is properly estimated in the entire region of the structure.

Fig. 3.5 summarizes the entire procedure of the sensor placement proposed in this study. First, the FE model of a structure is constructed, and a sufficient number of virtual sensors are initially placed in the desired area. Considering the target performance of virtual sensing, $\mathrm{E}_{\mathrm{trun}}$ in Eq. (3.19) and Eq. (3.22) and $\mathrm{E}_{\mathrm{cand}}$ in Eq. (3.21) are determined. The appropriate number of basis vectors $\bar{N}^*$ is determined by using Eq. (3.19) and a group of candidate sensors are made by utilizing Eq. (3.21). The final input sensors satisfying Eq. (3.22) with the minimum number M are selected among the P candidate sensors considering the condition number of $\mathbf{T}^{\mathrm{T}}\mathbf{T}$.

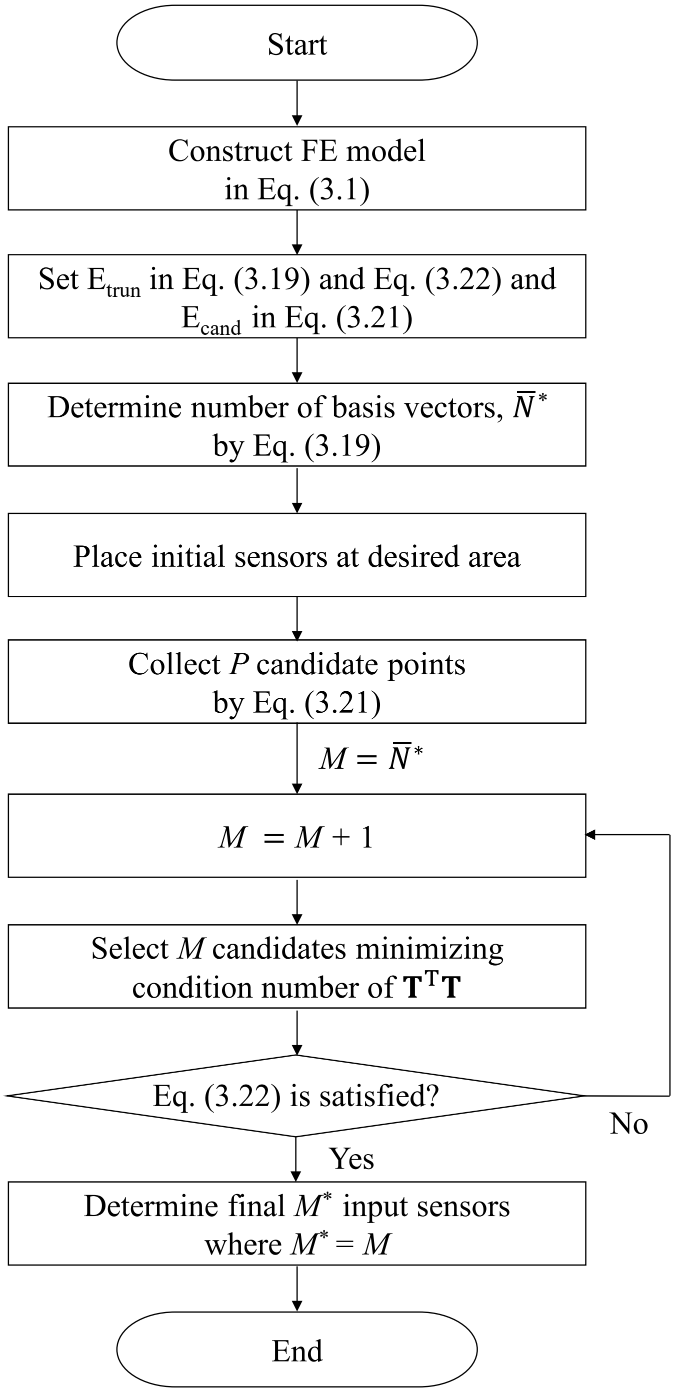

Figure 3.5: Entire procedure of the proposed sensor placement method.

Let us see the example of sensor placement by the proposed method for a beam structure under the operational load with fixed ends. The beam structure consists of 20 beam elements, and a strain sensor is placed virtually at the center of top surface of all elements. To obtain reference strain field, the number of basis vector is $\bar{N} = 2$ using the 1st and 2nd eigenvectors as displacement modes, and the number of sensors to be applied is $M = 3$.

Fig. 3.6(a) shows the target strain field and reference strain field of the structure for the operational load. Fig. 3.6(b) compares the two strain fields and shows 4 candidate sensor placement points of intersections of two fields (hollow circles), and the 3 points (solid circles) finally selected considering the condition number.

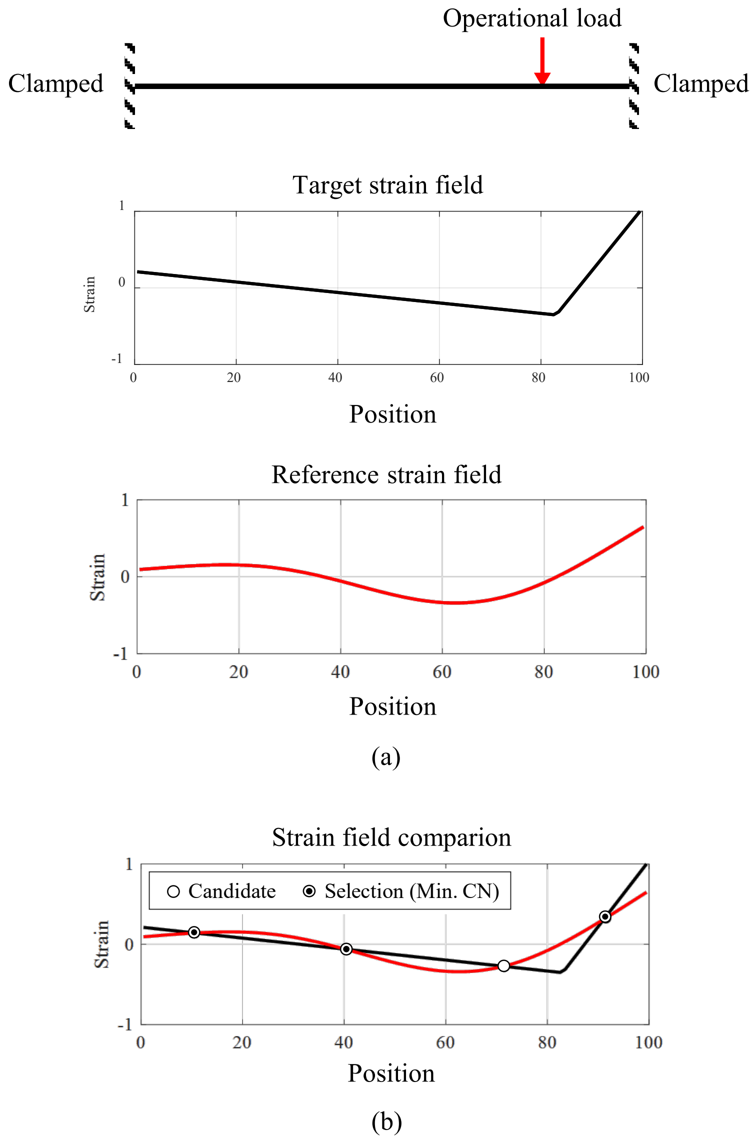

Figure 3.6: Example for sensor placement by proposed method: (a) Target and reference strain fields, (b) Intersections between two strain fields as candidates and finally selected points minimizing condition number.

3.5 Existing sensor placement methods

Among existing sensor placement methods, we briefly introduce Average Driving Point Residue (ADPR) [78, 79], Eigenvalue Vector Product (EVP) [78-80], Effective Independence (EfI) [84], and Minimizing Condition Number (CN) [24, 82, 83]. It is important to note that the methods were developed for the purpose of modal testing and thus do not consider operational loads. We compare their performances with that of the sensor placement method proposed in this research.

The ADPR method [78, 79] defines the averaged contribution of the *i*th candidate sensor for $\bar{N}$ basis vectors as

$$\mathrm{ADPR}_i = \sum_{j=1}^{\bar{N}} \mathrm{DPR}_{ij} \quad \text{with} \quad \mathrm{DPR}_{ij} = (\mathbf{Q}(\mathbf{n}_i)\mathbf{\Psi}_j^{(m_i)}(r_i, s_i, t_i))^2 / w_j , \tag{3.23}$$

where w_j is the *j*th natural frequency of a target structure and DPR_{ij} is the normalized contribution at the *i*th candidate sensor for the *j*th basis vector. Initially located sensors are ranked in order of magnitude of ADPR and M input sensors with larger ADPR are sequentially selected among them.

The EVP method [78-80] defines the multiplied contribution of the *i*th candidate sensor for $\bar{N}$ basis vectors as

$$\mathrm{EVP}_i = \prod_{j=1}^{\bar{N}} \left|\mathrm{T}_{ij}\right| = \left|\mathrm{T}_{i1}\mathrm{T}_{i2}\ldots\mathrm{T}_{i\bar{N}}\right| . \tag{3.24}$$

where T_{ij} is the component of *i*th row of *j*th basis vector. Initially located sensors are ranked in order of magnitude of EVP and M input sensors with larger EVP are sequentially selected among them. This method prevents sensors from selecting at nodal points of each mode and maximizes vibration energy.

The EfI method [84] seeks input sensors that maximize the independence between basis vectors. Effective independence matrix ($\mathbf{E}$) and its diagonal term, $\mathbf{E}_\mathrm{D}$, are defined for L sensors initially placed on a structure

$$\mathbf{E}_\mathrm{D} = \mathrm{diag}(\mathbf{E}) \quad \text{with} \quad \mathbf{E} = \mathbf{T}[\mathbf{T}^\mathrm{T}\mathbf{T}]^{-1}\mathbf{T}^\mathrm{T} , \tag{3.25}$$

where $\mathrm{diag}(\cdot)$ is an operator that extracts the diagonal components of the matrix, and the *i*th value of $\mathbf{E}_\mathrm{D}$ corresponds to the *i*th candidate sensor. The candidate corresponding to the minimum value of $\mathbf{E}_\mathrm{D}$ is removed and $\mathbf{E}_\mathrm{D}$ is for the remaining $(L-1)$ input sensors. This procedure is repeated until the desired M sensors are left.

In the CN method [24, 82, 83], we find a group of input sensors to minimize the condition number of $\mathbf{T}^{\mathrm{T}}\mathbf{T}$ matrix, which has the effect of increasing the independency between basis vectors. Since the possible combination of input sensors are very large in general, optimization algorithm is required to find the sensor group in practice. In this study, Genetic Algorithm (GA) is used to find the optimal group minimizing the condition number of $\mathbf{T}^{\mathrm{T}}\mathbf{T}$. Note that GA is a useful method for finding appropriate solutions in such combinatorial optimization problems [81, 85].

3.6 Numerical examples

The sensor placement method proposed in this paper is applied to the Jacket structure, Cut-out plate structure, and L-shaped bracket structure according to the sensor placement procedure in Fig. 3.5. In all examples, we apply $E_{trun} = 0.1$ to select the numbers of basis vectors and sensors and $E_{cand} = 0.05$ to determine the candidate points. We also apply $s_k = 1$ with the same weights for each target response.

The FE model for each example is composed of MITC3 and MITC4 shell elements [47, 55, 56, 86], and the mesh is constructed using elements of sufficiently small size for the FE analysis results to converge. The material properties of the structure for each example are shown in Table 1. Although arbitrary locations and directions can be considered for sensor placement, the sensor locations are restricted to the center points on the surface of each element and 4 sensor directions are considered: $\theta = 0^\circ$, 45°, 90°, and 135° with an arbitrary reference axis as depicted in Fig. 3.7.

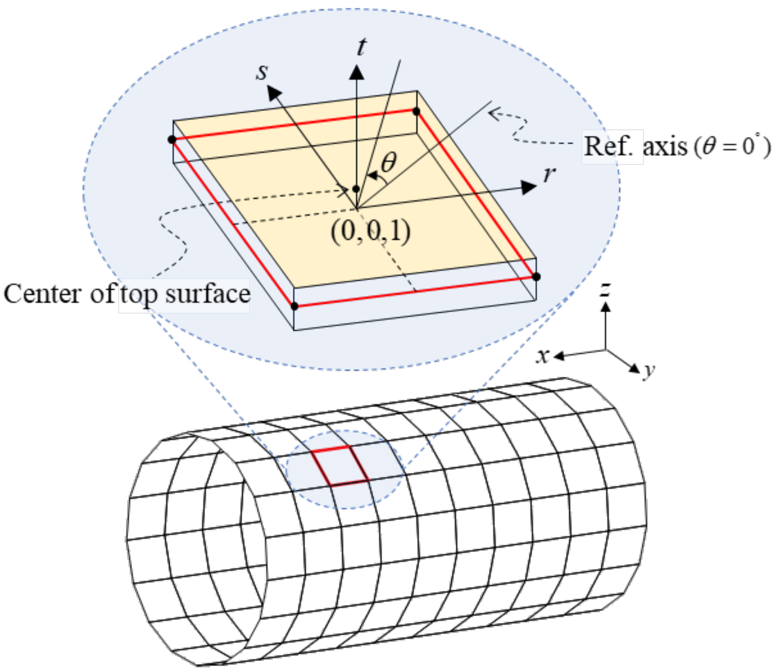

Figure 3.7: Center of top surface of element and the angle of strain sensor considered.

The performance of each sensor placement method is assessed through the accuracy of virtual sensing with the determined sensor placement. To simulate the situation of virtual sensing on a real structure through numerical experiments, the load $\hat{\mathbf{R}}(t)$ acting on the real structure is assumed by adding the noise of the load to the idealized operational load in Eq. (3.12) as

$$\hat{\mathbf{R}}(t) = \sum_{i=1}^{K} \hat{\mathbf{R}}_i(t) = \sum_{i=1}^{K} \mathbf{R}_i(t) + \Delta\mathbf{R}_i(t) \tag{3.26a}$$

where $\Delta\mathbf{R}_i(t) = \mathbf{R}_i(t) X_R$ with $X_R \sim N(0.1, 0.1^2)$. (3.26b)

$\Delta\mathbf{R}_i(t)$ representing the uncertainty of the load is obtained by considering a normal distribution X_R with mean of 0.1 and standard deviation of 0.1 to the ideal load $\mathbf{R}_i(t)$.

The response of the structure under $\hat{\mathbf{R}}(t)$ loading is calculated by dynamic implicit analysis, with a sampling rate of 1000 Hz and Rayleigh damping coefficients α and β for the damping matrix $\mathbf{C}$ as [47]

$$\alpha = \zeta \frac{2\omega_1\omega_2}{\omega_1 + \omega_2} \text{ and } \beta = \zeta \frac{2}{\omega_1 + \omega_2} \text{ with } \zeta = 0.05. \tag{3.27}$$

For the measured strain vector $\mathbf{e}(t)$, measurement noise $\boldsymbol{\varepsilon}_{\text{noise}}(t)$ is added to the $\boldsymbol{\varepsilon}_{\text{FE}}(t)$ calculated by the FE analysis as

$$\mathbf{e}(t) = \boldsymbol{\varepsilon}_{\text{FE}}(t) + \boldsymbol{\varepsilon}_{\text{noise}}(t) \tag{3.28a}$$

with $\boldsymbol{\varepsilon}_{\text{noise}}(t) = \boldsymbol{\varepsilon}_{\text{FE}}(t) X_\varepsilon$ and $X_\varepsilon \sim U(-0.05, 0.05)$. (3.28b)

The measurement noise is obtained by applying a uniform distribution ranging from −0.05 to 0.05 to the FE strain.

We evaluate the performance of virtual sensing by repeating the numerical experiment I times to consider the randomness of the parameters w_k, t_k, Ω_k, α_k, and noise X_R for loads, and the noise X_ε for the measurement. Finally, the accuracy of the virtual sensing is evaluated using the mean $\mu[\mathrm{E}_{\text{all}}(i)]$ and standard deviation $\sigma[\mathrm{E}_{\text{all}}(i)]$ of the estimation error $\mathrm{E}_{\text{all}}(i)$, where $\mathrm{E}_{\text{all}}(i)$ denotes the estimation error of the virtual sensing at the *i*th iteration.

3.6.1 Jacket structure

The jacket structure is one of the typical fixed offshore structures and is subjected to continuous repetitive loading by waves, wind and working facilities. For the jacket structure, Eq. (3.12) is expressed as follows using the horizontal loads due to waves and wind and the vertical load due to the working area.

$$\begin{aligned}\mathbf{R}(t) = {} & \mathbf{R}_1 w_1 \cos(2\pi\Omega_1 t + \alpha_1) u_1(t) + \mathbf{R}_2 w_2 \cos(2\pi\Omega_2 t + \alpha_2) u_2(t) \\ & + \mathbf{R}_3 w_3 \cos(2\pi\Omega_3 t + \alpha_3) u_3(t)\end{aligned} \tag{3.29}$$

where $\mathbf{R}_1$ and $\mathbf{R}_2$ represent the distribution of x- and y-directional horizontal loads by waves and wind, and $\mathbf{R}_3$ represents the distribution of z-directional vertical loads by working facilities. Fig. 3.8 shows the geometry and boundary conditions of the jacket structure with the distribution of the operational loads $\mathbf{R}_1$, $\mathbf{R}_2$, and $\mathbf{R}_3$. The material properties are listed in Table 1. The axis of $\theta = 0^\circ$ for defining sensor direction is set to the axial direction of the pipe where each element belongs.

The horizontal loads $\mathbf{R}_1$ and $\mathbf{R}_2$ due to wave and wind have low excitation frequencies compared to the natural frequency of the structure, leading to a quasi-static behavior. The vertical load $\mathbf{R}_3$ due to working facilities also has a lower frequency than the 1st natural frequency of the jacket structure to avoid resonance. Therefore, excitation frequencies for $\mathbf{R}_1$, $\mathbf{R}_2$, and $\mathbf{R}_3$ are considered to be 0, 5, and 10 Hz, which are lower than the 1st natural frequency of jacket structure, 22 Hz. The target strain field corresponding to each operational load is described in Fig. 3.9.

Table 3.1: Material properties of examples.

Example	E [MPa]	υ [$-$]	Thick [mm]	ρ [kg/mm^3]
Jacket	3900	0.3	2.0	1.2×10^{-9}
Cut-out plate	200×10^3	0.3	0.1	7.8×10^{-9}
L-shaped bracket	3900	0.3	10.0	1.2×10^{-9}

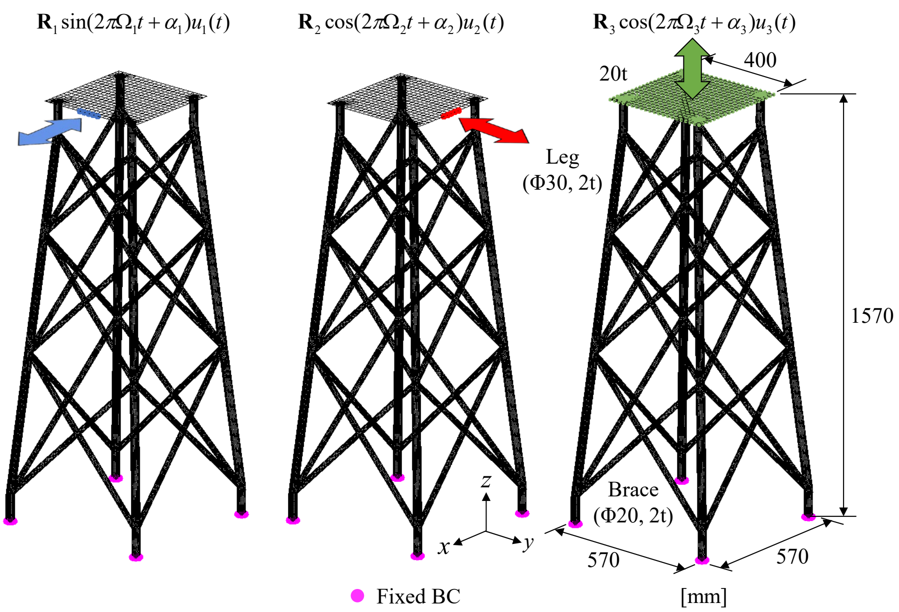

Figure 3.8: Operational loads applied to jacket structure: (a) Lateral load in x-direction, (b) Lateral load in y-direction, (c) Vertical load in z-direction.

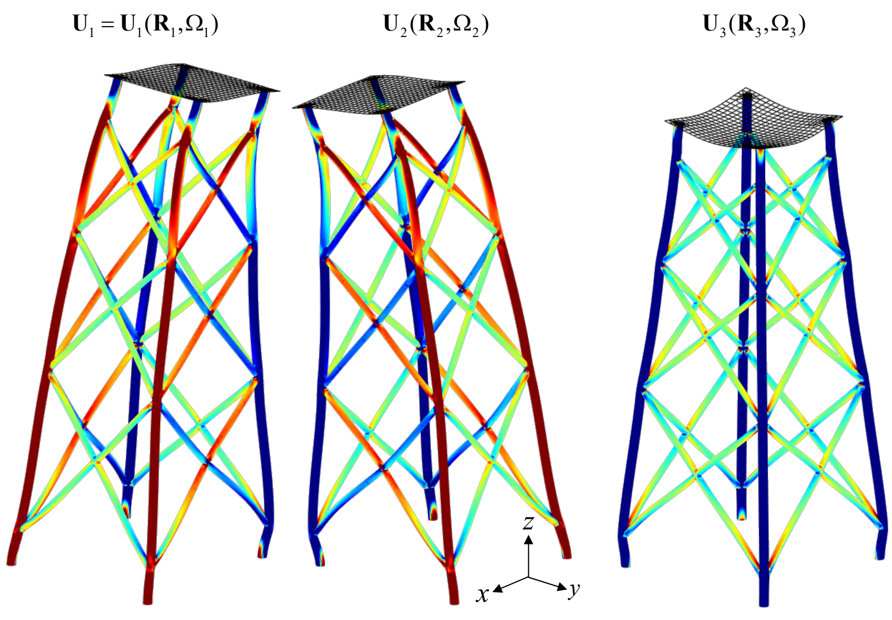

Figure 3.9: Target deformed shape by operational loads: (a) Bending shape by lateral loads in x-direction, (b) Bending shape by lateral loads in y-direction, (c) Deformed shape by vertical loads in z-direction

The number of basis vectors is determined by Eq. (3.19). Fig. 3.10 shows the minimum estimation error $\mathrm{E}_{\min}$ for the target strain field according to number of basis vectors, where the minimum number of basis vectors that satisfies the target performance is $\bar{N}^{*}=9$.

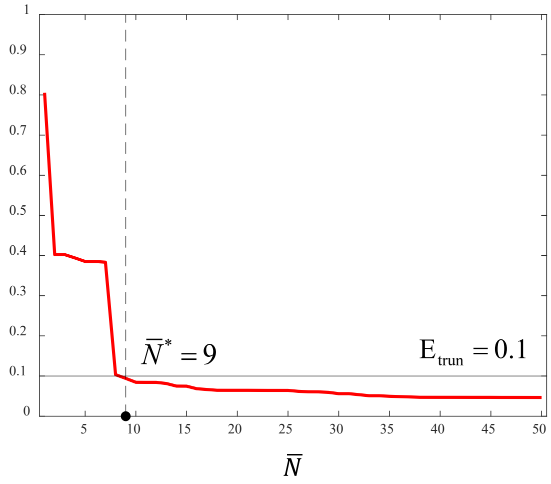

Figure 3.10: Numerical example 1: Determination of the number of basis vectors.

By applying the determined number of basis vectors, $\bar{N}=9$, the location, direction, and number of sensors are determined to satisfy Eq. (3.22). In addition, sensor placement is considered in the area above the waterline since most of area of jacket structure is submerged in water. The proposed sensor placement method satisfies the target performance when the number of sensors is $M=15$ or more.

To compare the virtual sensing performance according to sensor placement determined by each sensor placement method, the same number of sensors and determined number of basis vectors are applied to each method. Figs. 3.11(a) and (b) show the estimation error $\mathrm{E}_{\mathrm{all}}$ of each sensor placement method for the target strain field with $\bar{N}=9$ and $M=15$ and the sensor placement determined by the proposed method, respectively. The estimation error of the proposed method is closest to $\mathrm{E}_{\min}$ among sensor placement methods.

While the existing sensor placement methods fail to find a sensor placement that satisfies the target performance from the initial sensors limited above the water depth, the proposed method determines a sensor placement that satisfies the target performance using a small number of sensors, which means that the proposed method is capable of sensor placement considering the performance of virtual sensing and efficiency from the perspective of sensor cost.

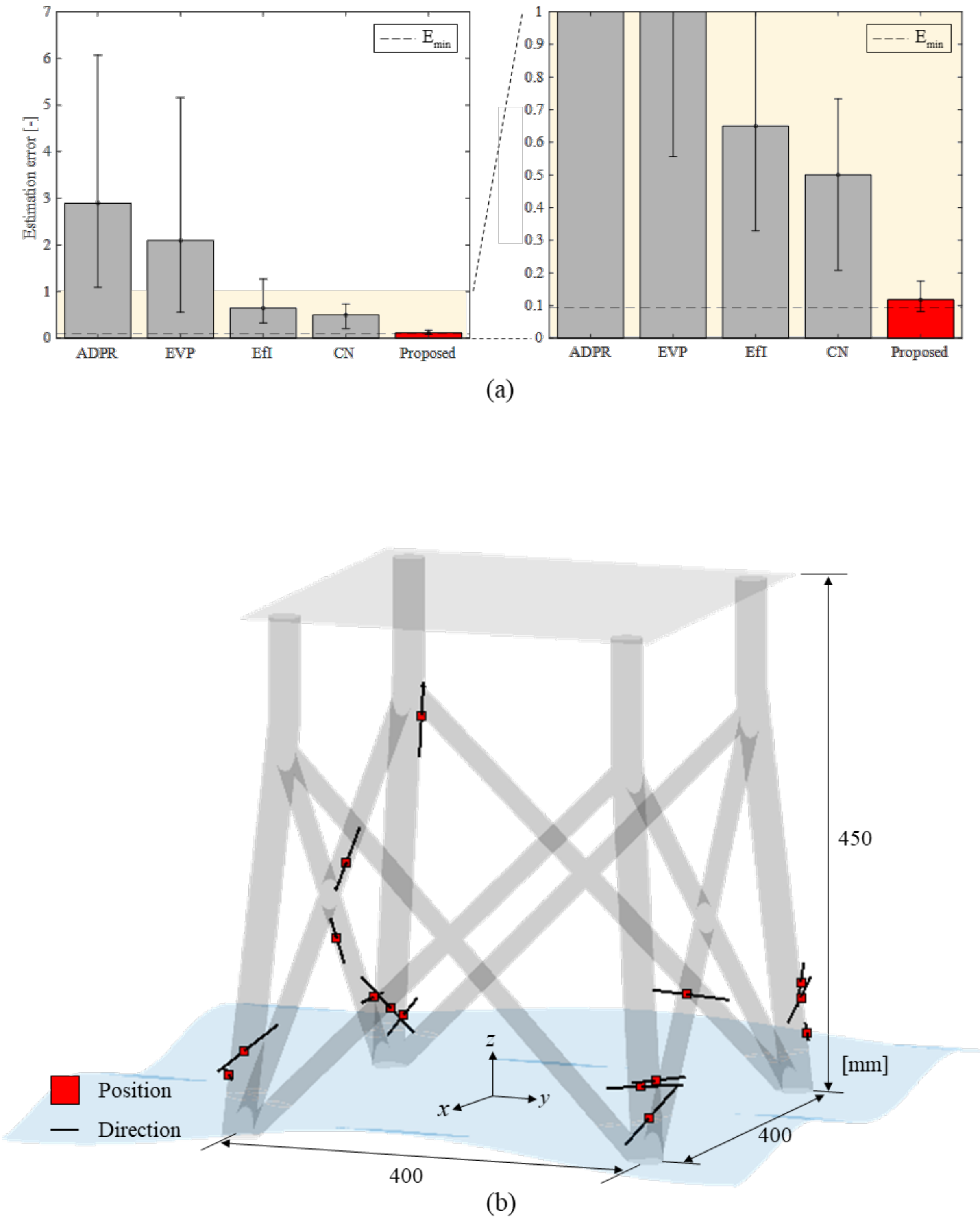

Figure 3.11: Numerical example 1: (a) Estimation errors of each sensor placement method for target responses, (b) Determined sensor placement by the proposed method.

Next, numerical experiments are conducted to verify that the determined sensor placement performs virtual sensing properly in operational state. The ranges of the random parameters for the numerical experiment are $0 < w_k \leq 1$, $0 \leq t_k \leq 1$, $0 \leq \Omega_k \leq 10$, and $0 \leq \alpha_k \leq 2\pi$ with the number of iterations $I = 10$ and damping coefficients $\alpha = 7.2$ and $\beta = 3.5 \times 10^{-4}$. Fig. 3.12 shows the signal of relative magnitude for each $\mathbf{R}_i$ at an arbitrary iteration.

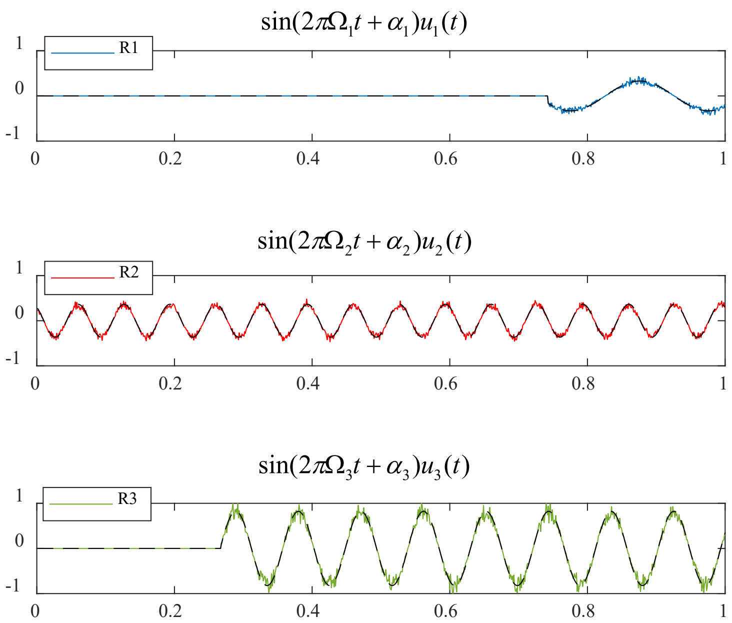

Figure 3.12: An example of load signal of each load during numerical experiment for jacket structure.

Fig. 3.13(a) shows the mean and standard deviation of the estimation error for 10 iterations. The sensor placement by the proposed method shows the minimum estimation error closest to $\mathrm{E}_{\min}$ among the sensor placement methods. Fig. 3.13(b) compares the estimated strain field on the deformed shape by the proposed method with that of the FE solution at a moment of iterations, where the two results are in good agreement. The norm ratio and correlation of the estimated strain vector to that of the FE solution is 1.02 and 0.99, respectively.

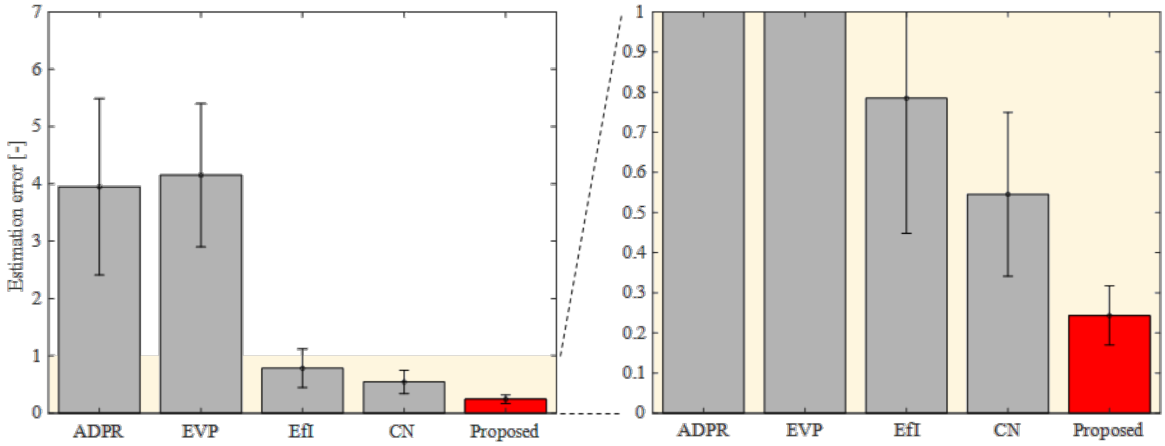

(a)

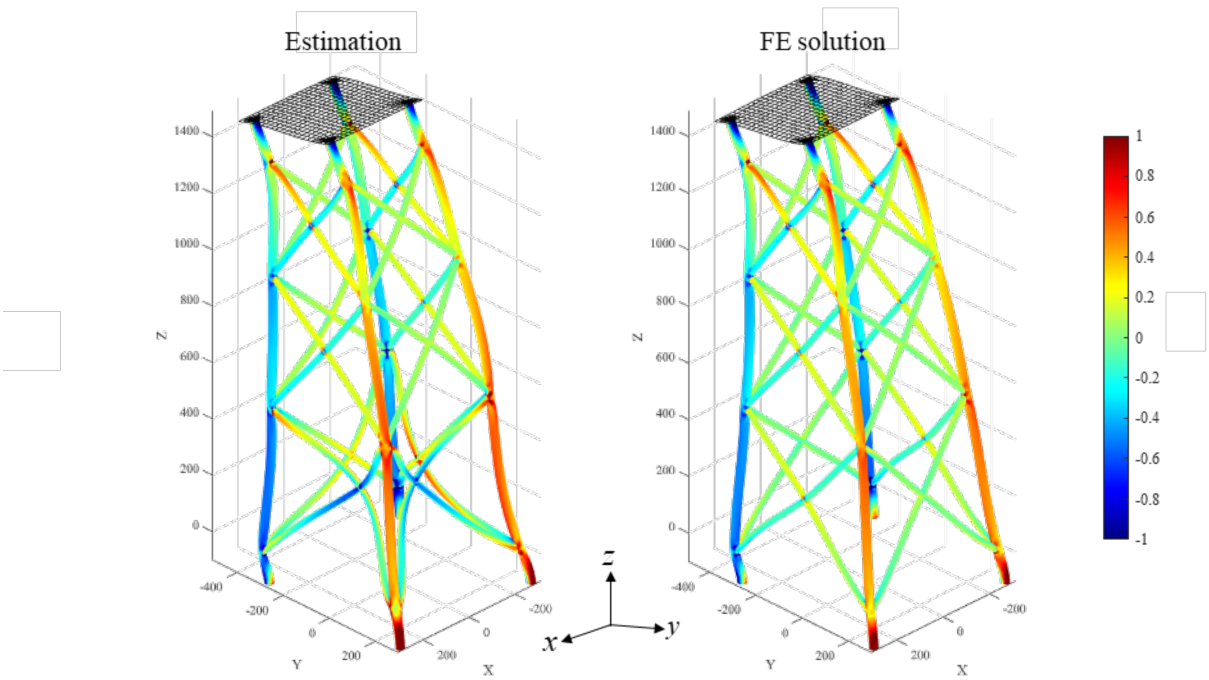

(b)

Figure 3.13: Numerical example 1: (a) Estimation error of each sensor placement method during numerical experiment, (b) Estimated strain distribution on the deformed shape using determined sensor placement by the proposed method with that of FE analysis at one of iterations during numerical experiment.

3.6.2 Cut-out plate structure

Fig. 3.14 shows the FE model of a cut-out plate structure supported at both ends and the distributions of four assumed operational loads. The target strain field consists of 20 cases with frequencies of 0, 43, 96, 121, and 225 Hz (static and 80% of the 1st to 4th natural frequencies of the structure) applied to the 4 main loads. The nodes colored in pink represent the fixed boundary conditions, and the material properties are listed in Table 1. The axis of $\theta = 0^{\circ}$ for defining the sensor direction is aligned with the x-direction. This structure is a representative plate structure whose behavior is dominated by deflection. This example demonstrates the performance of sensor placement on such structures.

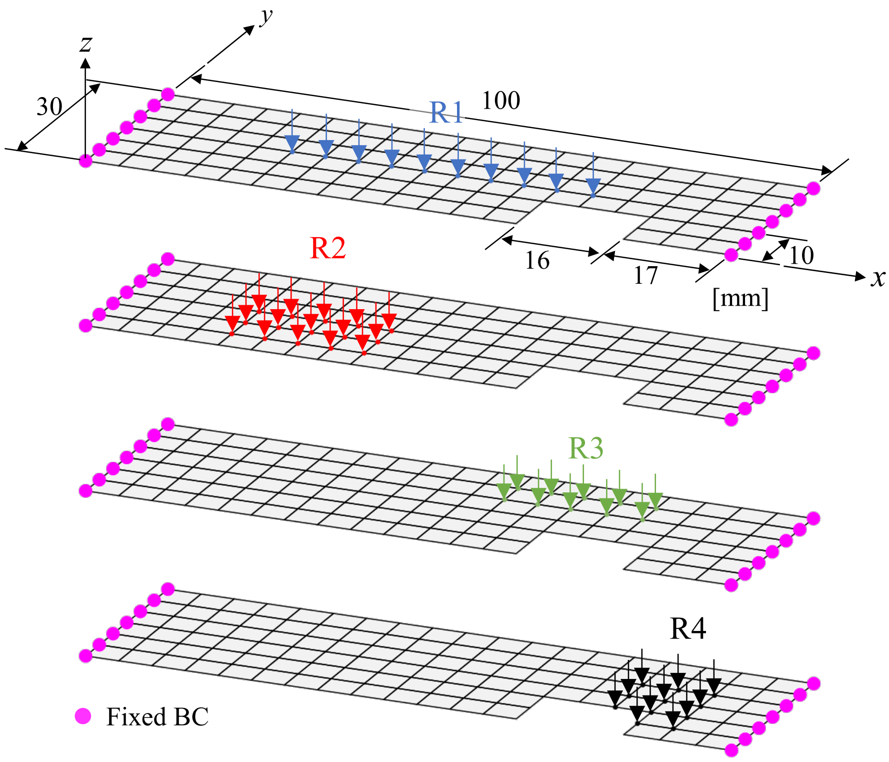

Figure 3.14: Numerical example 2: Cut-out plate structure with its boundary conditions and operational loads.

The number of basis vector is determined by Eq. (3.19). Fig. 3.15(a) shows the estimation error for the target strain fields as a function of the number of basis vector, where $\bar{N}^* = 9$ is the minimum number of basis vector that satisfies the target performance.

By applying the determined number of basis vectors, $\bar{N} = 9$, the location, direction, and number of sensors are determined to satisfy Eq. (3.22). Fig. 3.15(b) shows the minimum number of sensors that satisfy Eq. (3.22) for each sensor placement method. The proposed method and EfI method satisfy the target performance when the number of sensors is M=10 or more. The proposed method enables efficient sensor placement from the perspective of sensor cost, and it uses small number of sensors compared to other methods to achieve sensor placement that satisfies the target performance.

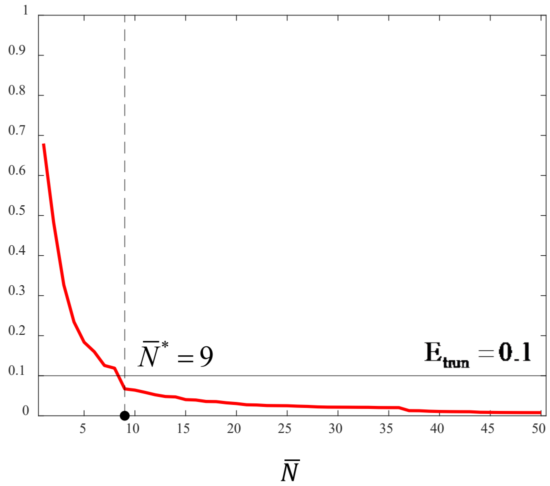

(a)

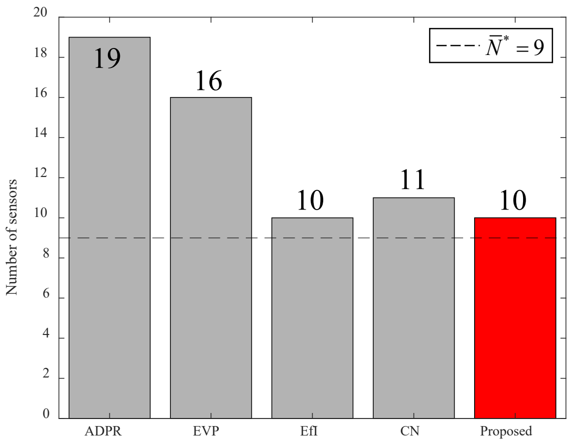

(b)

Figure 3.15: Numerical example 2: (a) Determination of the number of basis vectors, (b) Minimum number of sensors for each sensor placement method.

To compare the virtual sensing performance according to sensor placement determined by each sensor placement method, the same number of sensors and determined number of basis vectors are applied to each method. Fig. 3.16 shows the estimation error of each sensor placement method for target responses and the sensor placement determined by the proposed method when $\bar{N} = 9$ and $M = 11$. The estimation error of the proposed method, EfI method, and CN method for the target strain fields are quite close to $\mathrm{E}_{\min}$.

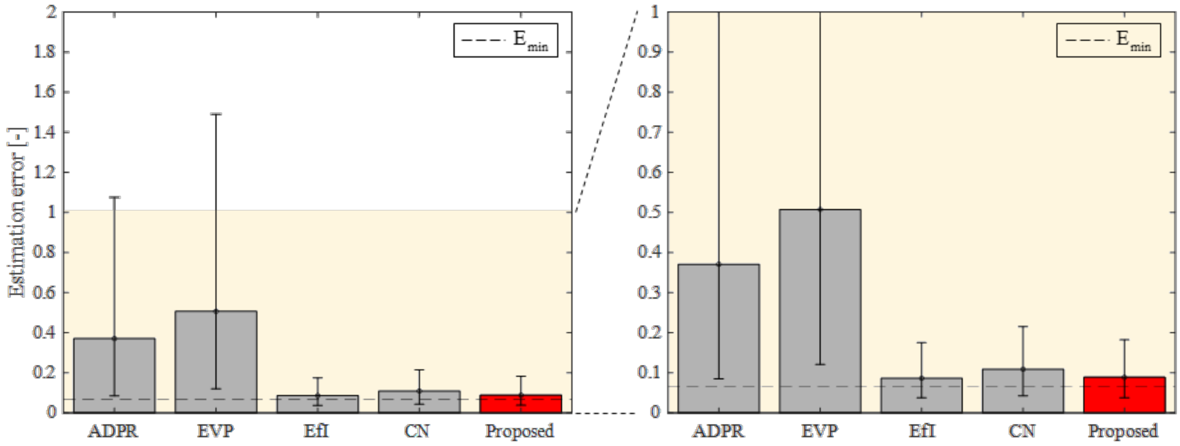

(a)

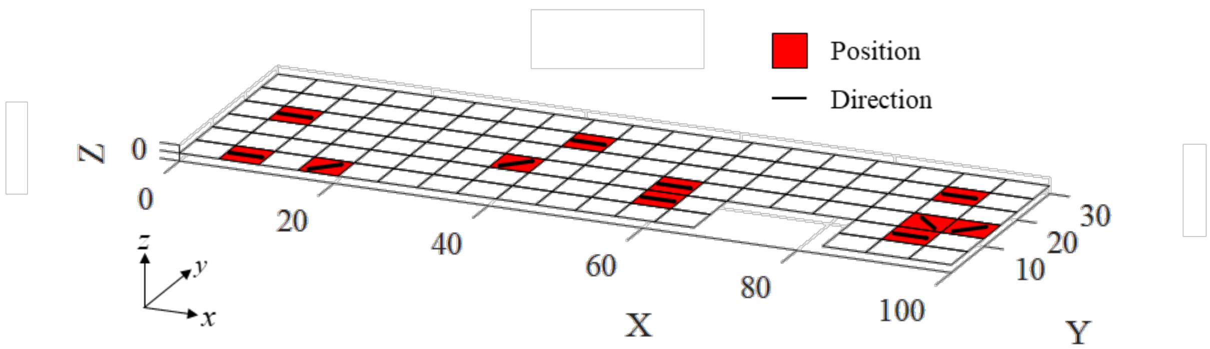

(b)

Figure 3.16: Numerical example 2: (a) Estimation errors of each sensor placement method for target responses, (b) Determined sensor placement by the proposed method.

Next, numerical experiments are conducted to validate that the determined sensor placement performs virtual sensing with high accuracy in operational state. The ranges of the random parameters for the numerical experiment are the same with those of example 1 with the damping coefficients $\alpha = 23.3$ and $\beta = 9.1\times10^{-5}$.

Fig. 3.17 shows the results of the numerical experiments. Fig. 3.17(a) shows the mean and standard deviation of the estimation error of sensor placement methods. Except for ADPR and EVP method, estimation errors are quite low. In this example, the proposed method and some existing methods find the appropriate sensor placement, which is expected because the geometry and behavior of the structure are relatively simple. Fig. 3.17(b) compares the estimated strain field on the deformed shape of the proposed method with that of the FE solution at a moment of iterations, where the two results are in good agreement. The norm ratio and correlation of the estimated strain vector to that of the FE solution is 1.0 and 0.99, respectively.

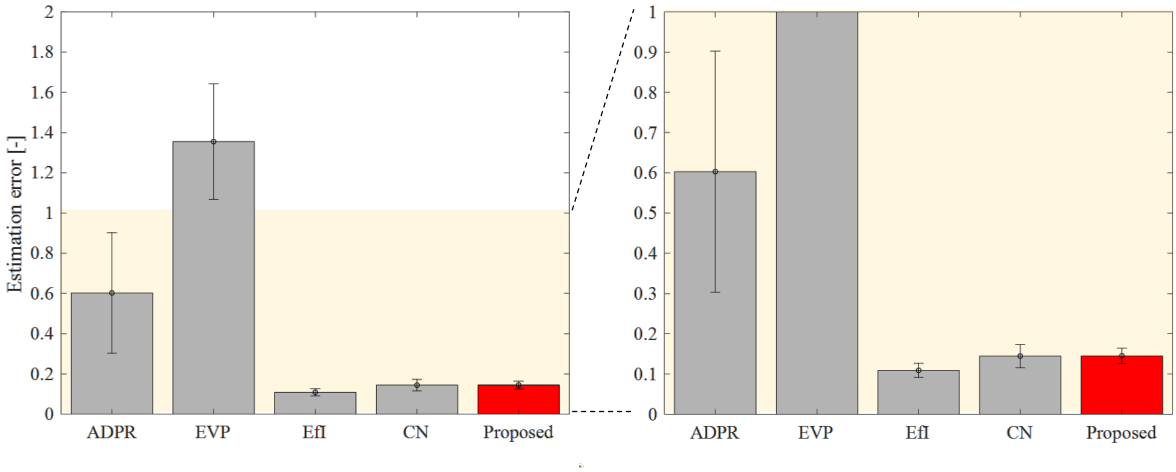

(a)

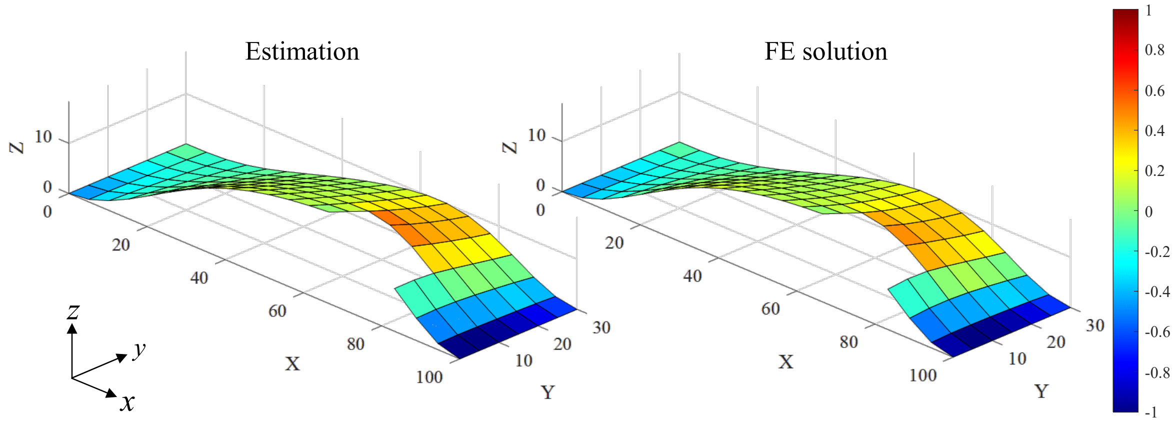

(b)

Figure 3.17: Estimation error of each sensor placement method during numerical experiment, (b) Estimated strain distribution on the deformed shape using determined sensor placement by the proposed method with that of FE analysis at one of iterations during numerical experiment.

3.6.3 L-shaped bracket structure

Fig. 3.18 shows the FE model of a L-shaped bracket structure and the distributions of four assumed operational loads. The target strain field consists of 20 cases with frequencies of 0, 22, 63, 111, and 151 Hz (static and 80% of the 1st to 4th natural frequencies of the structure) applied to the 4 main loads. The nodes colored in pink represent the fixed boundary conditions, and the material properties are listed in Table 1. The axis of $\theta = 0^{\circ}$ for defining the sensor direction is aligned with the x-direction for the elements in bottom and z-direction for the other elements. This structure exhibits a variety of behaviors, including deflection, torsion, and rotation; thus, this example demonstrates the performance of sensor placement on arbitrary structures.

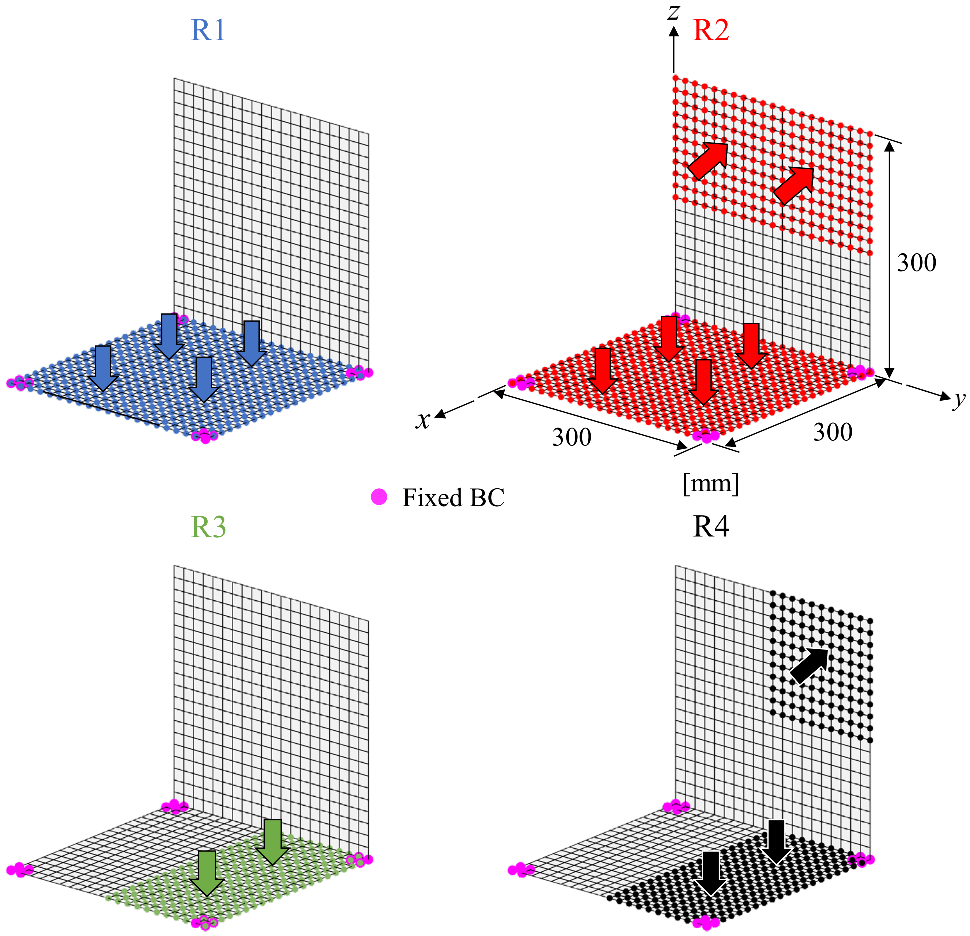

Figure 3.18: Numerical example 3: Chair-shaped structure with its boundary condition and operational loads.

The number of basis vector is determined by Eq. (3.19). Fig. 3.19(a) shows the estimation error for the target strain fields as a function of the number of basis vector, where $\bar{N}^* = 5$ is the minimum number of basis vector that satisfies the target performance.

By applying the determined number of basis vectors, $\bar{N} = 5$, the location, direction, and number of sensors are determined to satisfy Eq. (3.22). Fig. 3.19(b) shows the minimum number of sensors that satisfy Eq. (3.22) for each sensor placement method. The proposed method, EfI method, and CN method satisfy the target performance when the number of sensors is $M = 6$ or more. The proposed method enables efficient sensor placement from the perspective of sensor cost, and it uses small number of sensors compared to other methods to achieve sensor placement that satisfies the target performance.

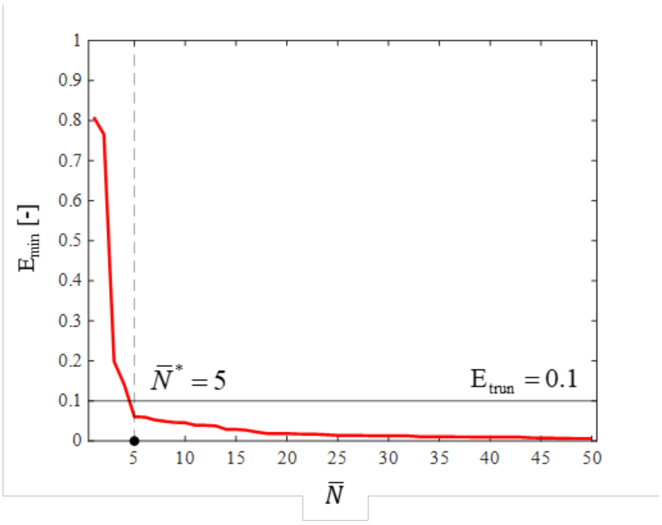

(a)

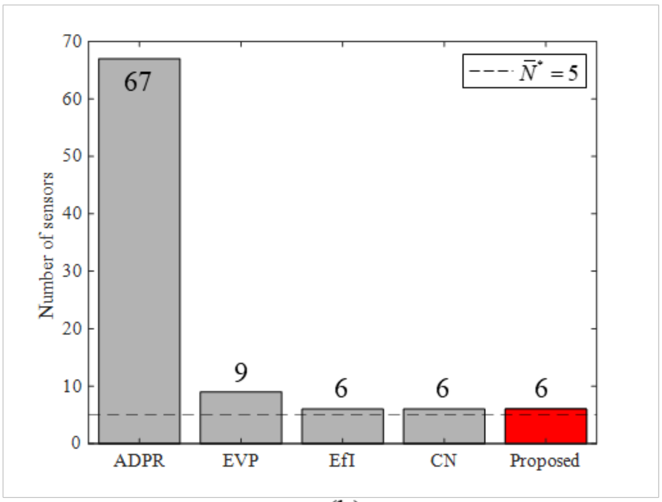

(b)

Figure 3.19: Numerical example 3: (a) Estimation errors of each sensor placement method for target responses, (b) Determined sensor placement by the proposed method.

To compare the virtual sensing performance according to sensor placement determined by each sensor placement method, the same number of sensors and determined number of basis vectors are applied to each method. In addition, to consider constrained sensor installation area in actual structures, limit the area of the initially located sensors as shown in Fig. 3.20(a). Figs. 20(b) and (c) show the sensor placements determined by the proposed method and the estimation error of each sensor placement method for the target strain fields, respectively, when $\bar{N} = 5$ and $M = 7$. The estimation error of the proposed method for the target strain fields are closest to $\mathrm{E}_{\min}$.

Fig. 3.21 shows the results of the numerical experiment for the proposed method, which is performed under the same conditions with those of previous examples and the damping coefficients $\alpha = 12.8$ and $\beta = 1.5 \times 10^{-4}$. Fig. 21(a) shows the mean and standard deviation of the estimation error of sensor placement methods, where proposed methods shows the lowest estimation error. Fig. 21(b) compares the estimated strain field on the deformed shape by the proposed method with that of the FE solution at a moment of iterations, where the two results are in good agreement. The norm ratio and correlation of the estimated strain vector to that of the FE solution is 1.02 and 0.96, respectively.

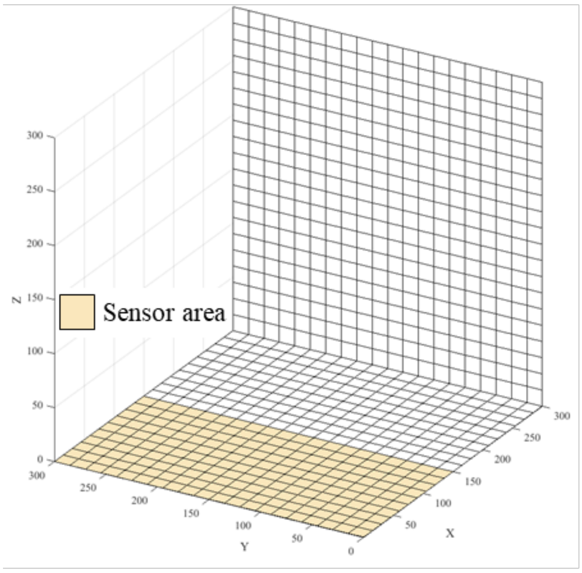

(a)

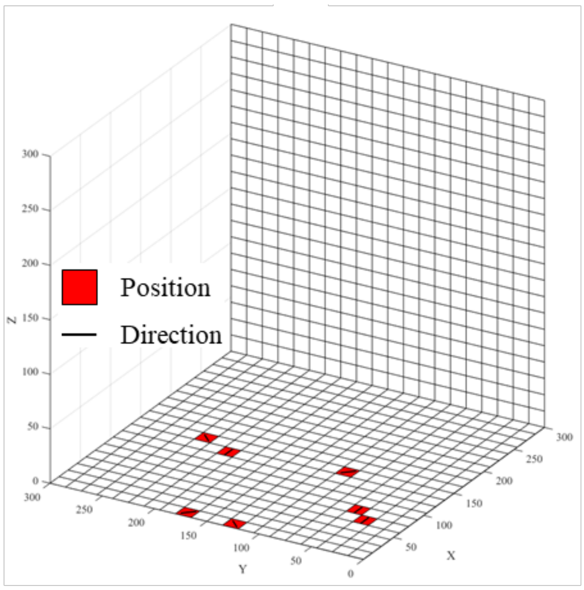

(b)

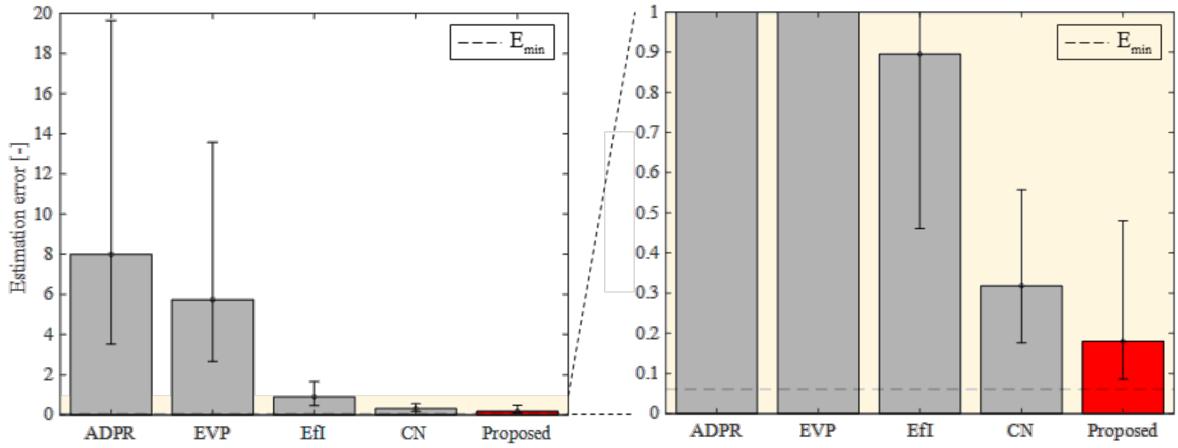

(c)

Figure 3.20: Numerical example 3: (a) Estimation errors of each sensor placement method for target responses, (b) Determined sensor placement by the proposed method.

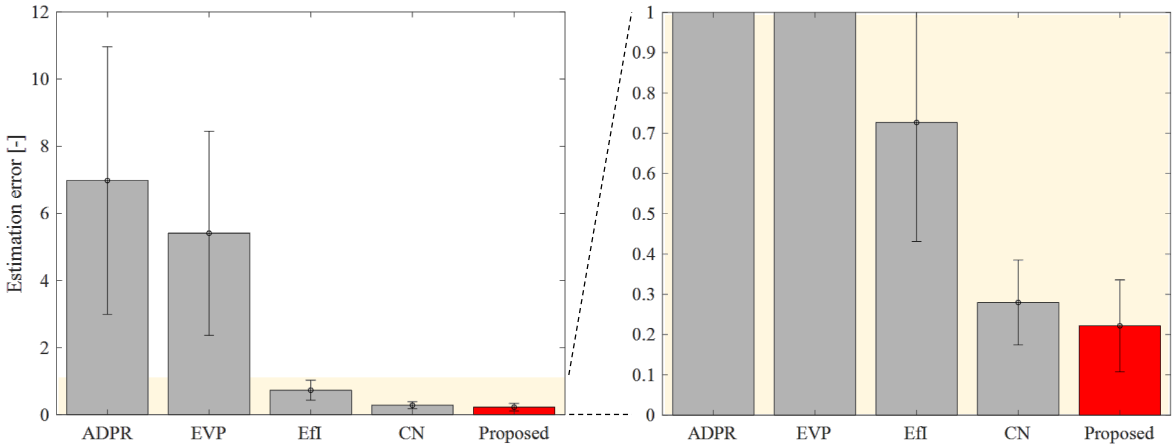

(a)

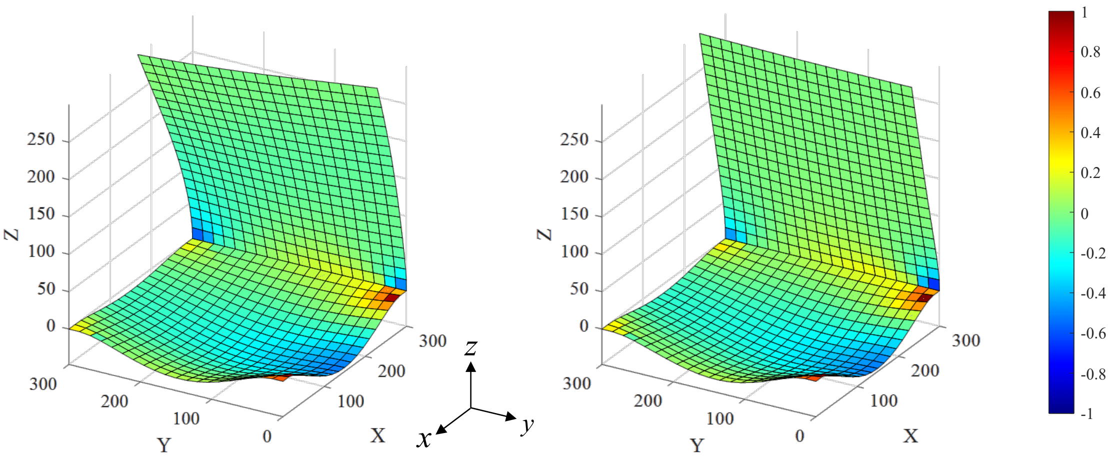

(b)

Figure 3.21: Numerical example 3: (a) Estimation error of each sensor placement method during numerical experiment, (b) Estimated strain distribution on the deformed shape using determined sensor placement by the proposed method with that of FE analysis at one of iterations during numerical experiment.

Table 3.2 summarized mean and standard deviation of the estimation error of each sensor placement method and each example in numerical experiment. The proposed sensor placement method determines the sensor placement such that the estimated strain fields are close to the target (or reference) strain field regardless of the structure. In addition, even when the sensor installation area is constrained, the proposed method still finds an appropriate sensor placement unlike other sensor placement methods.

Table 3.2: Mean and standard deviation of estimation error during numerical experiment of sensor placement methods according to examples.

Example	ADPR	EVP	EfI	CN	Proposed
Jacket	μ =0.11 σ =0.04	4.15 1.25	0.79 0.33	0.54 0.20	0.24 0.07
Cut-out plate	0.60 0.30	1.36 0.30	0.11 0.02	0.14 0.03	0.14 0.02
L-shaped bracket	0.70 3.83	5.47 2.96	0.74 0.30	0.29 0.12	0.24 0.11

3.7 Conclusions

In this Chapter, the novel sensor placement method is proposed for virtual sensing. Since the accuracy of virtual sensing varies depending on the sensor placement, a method that can determine the proper sensor placement is required. The method presented in this paper determines a sensor placement showing higher virtual sensing accuracy even in the case of various types of structures and constrained sensor installation areas by considering operational loads of the structure.

First, target strain fields corresponding to operational loads are constructed using FE analysis, and the number of basis vectors that satisfy the target performance is determined using the minimum estimation error. Next, sensors are placed at the intersection between the target strain field and the reference strain field that is the maximum accurate estimated strain field by the given basis vectors for the target strain field.

The proposed method is applied to 3 different structures. The proposed method shows the efficiency of finding the sensor placement that satisfies the target performance with a small number of sensors. Through numerical experiments, the sensor placement results are applied to virtual sensing and its performance is evaluated using the estimation error. The sensor placement by the proposed method shows high virtual sensing accuracy and robustness compared to existing sensor placement methods. In particular, the more complex the geometry of the structure and the more diverse the behavior of the structure, the higher the virtual sensing performance of the proposed method compared to the existing methods. Therefore, the proposed sensor placement method is suitable for various structures, and constrained sensor installation area.

For the future works, guidelines for determining E_{trun} and E_{cand} are required for more accurate virtual sensing and completeness of the proposed method. Finally, the proposed method the sensor placement by the proposed method will be applied to actual structures to validate the performance of the proposed method in real conditions.

Chapter 4. Conclusions and Future works

4.1 Conclusions

This dissertation comprehensively explores virtual sensing, covering a wide range of aspects from its formulation to numerical schemes aimed at improving strain estimation accuracy. The proposed procedure ensures accurate and reliable virtual sensing, applicable in real-time structural deformation estimation for next-generation technologies like structural health monitoring, digital twin, virtual reality, etc.

In Chapter 1, the concept of virtual sensing and research background are introduced briefly with the objective and scope of the dissertation.

In Chapter 2, a comprehensive virtual sensing procedure based on the mode superposition method is formulated. This formulation serves as a starting point for the further development of virtual sensing schemes by subsequent researchers. Additionally, the virtual sensing procedure is enhanced by incorporating regularization of generalized coordinates into the conventional least square method to improve accuracy and stability of virtual sensing. The improved virtual sensing more accurately estimates the strain field, alleviating the overfitting problem of the conventional least square method. Finally, the virtual sensing is applied to a lab-scale jacket structure having a complex geometry considering wave loads both numerically and experimentally. This evaluation aims to assess the performance of strain field estimation. In numerical tests, strain and deformed shape are well estimated over the entire area of the structure. In experimental tests, strains at validation sensors are accurately estimated and the estimated strain field and deformed shape are also physically reasonable, despite disturbances from truncation and measurement errors. It is concluded that the performance of virtual sensing is improved by the proposed regularization scheme and the accuracy and feasibility of virtual sensing is verified through experiments.

In Chapter 3, a guideline for proper number of basis vectors and a novel sensors placement method are proposed. The number of basis vector by the proposed guideline satisfies target performance of virtual sensing. The guideline would be very useful for actual installation of virtual sensing system. In addition, the novel sensor placement method is proposed considering operational loads for proper and efficient sensor placement, where sensors are placed on intersection between target and reference strain fields. The proposed method gives better sensor placement for an accurate and robust virtual sensing, especially when sensor installation region is limited. The guideline and sensor placement method are validated through numerical experiment for various examples, resulting that the proposed method finds better sensor placement having high virtual sensing performance compared to existing methods, regardless of target structures and sensor placement conditions.

4.2 Future works

Mode-based virtual sensing offers the advantage of estimating deformation using a small number of sensors, ensuring accurate and stable deformation estimation using basis vectors considering operational loads of the structure. This method, however, has a limitation in accuracy when unconsidered loads are applied to the structure. Given that actual structures generally experience specific loads according to their original purpose rather than arbitrary ones, mode-based virtual sensing is a very efficient and reasonable approach. For more versatility, this method needs to be improved to cover various types of operational loads. The load-dependent issue can be addressed by using a POD basis capable of covering various types of operational loads. Alternatively, ANN-based approach or adaptively changing basis based on structural response would be another solution.

Strain data is employed in this research as a structural response due to its simplicity and cost-effectiveness. Depending on the response type, such as acceleration, velocity, displacement, etc., it may be advantageous to capture specific behaviors of the structure. In addition, limitations in the measuring range or resolution may arise depending on the target response and sensor types. Therefore, measuring various physical quantities enables a more comprehensive capture of structural behavior and facilitates monitoring a wide range and detailed structural health state. To apply various responses to virtual sensing, measured responses need to be normalized properly, and FE formulation is necessary to create basis vectors corresponding to the responses.

Finally, it is crucial to validate the performance of virtual sensing on real-scale structures under operational loads after further improvement to account for various operational loads and a wide range of responses.

Appendix A. Error sources of virtual sensing

In this Chapter, error sources existing in virtual sensing is analyzed how they reduce estimation accuracy. Generally, the number of sensors used for strain estimation in virtual sensing is quite small compared to the number of DOFs of the corresponding FE model due to the cost, maintenance, and installation difficulties of sensors. In addition, measurement errors such as overshooting and noise signal are captured together with the physical strain signal of the structure during measurement. Furthermore, the least square solution used in virtual sensing calculates the generalized coordinates through orthogonal projection, resulting strain error is orthogonal to basis vectors. Limited sensing region, strain error, and orthogonal projection affects together on reducing the accuracy of the virtual sensing (Fig. A.1).

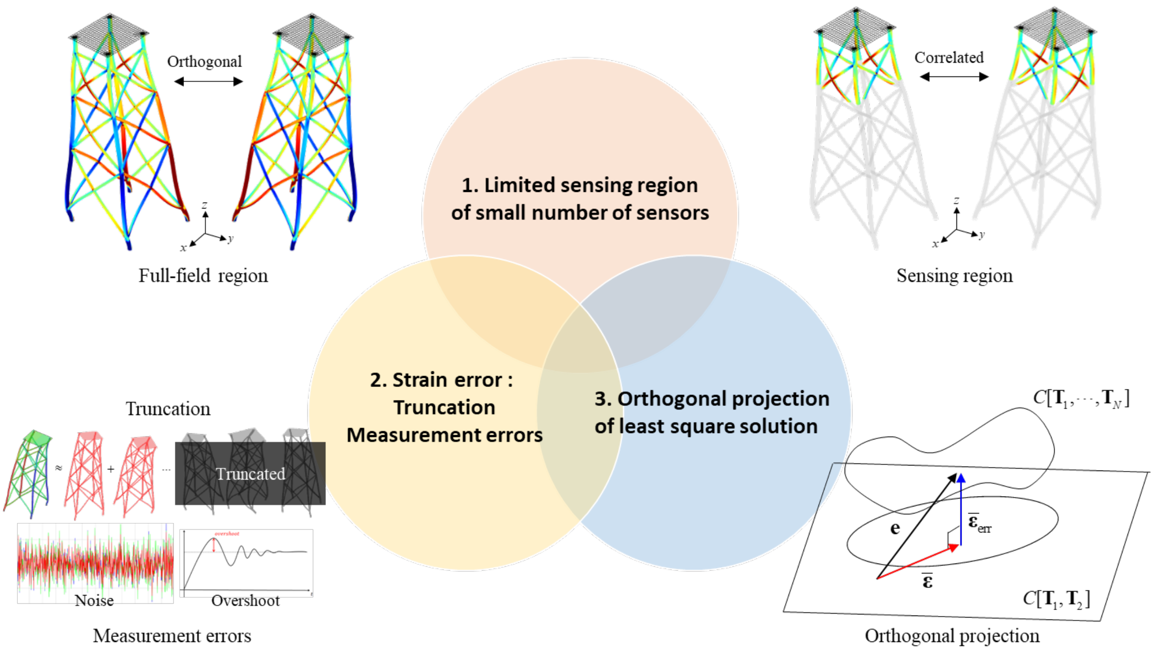

Figure A.1: Error sources of virtual sensing.

The correlations of basis vectors in the sensing region are different from those over the full-field region. Let's consider the correlations of the strain basis vectors for the free vibration part described in Chapter 2. Correlation is calculated using MAC as [87, 88]

$$\mathrm{MAC}_{ij} = \frac{(\mathbf{T}_i^{\mathrm{T}}\mathbf{T}_j)^2}{(\mathbf{T}_i^{\mathrm{T}}\mathbf{T}_i)(\mathbf{T}_j^{\mathrm{T}}\mathbf{T}_j)} \tag{A.1}$$

Fig. A.2 shows the correlations of basis vectors for the full-field region and sensing region where the value of *i*th row and *j*th column corresponds to the correlation between $\mathbf{T}_i$ and $\mathbf{T}_j$. Strain basis vectors over the full-field region have an orthogonal relationship as shown in Fig. A.2(a) but those are correlated in the sensing region as shown in Fig. A.2(b).

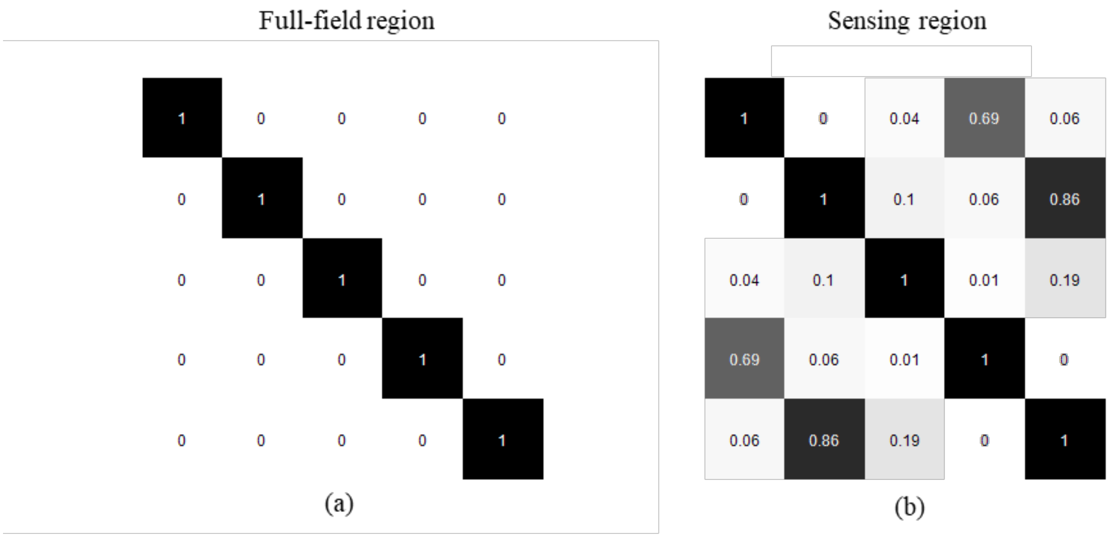

Figure A.2: Correlations of strain basis vectors according to considering region.

Since the least square solution is calculated through orthogonal projection on the basis vectors considered, the strain error is always orthogonal to the basis vectors. Fig. A.3(a) shows the relationship between strain basis vectors $\mathbf{T}$, measured strain $\mathbf{e}$, estimated strain $\bar{\boldsymbol{\varepsilon}}$, and strain error $\bar{\boldsymbol{\varepsilon}}_{\mathrm{err}}$ for the full-field region. The estimated strain considering full-field region corresponds to the reference strain having the maximum accuracy that given basis set can have.

In the actual sensing, strain is measured only at sensor locations, so the result of the least square solution of the full-field region is re-described in the sensing region as shown in Fig. A.3(b). In the sensing region, the correlations between basis vectors are changed, resulting that strain error that is orthogonal to all basis vectors in the full-field region is no longer orthogonal in the sensing region; thus, estimated strain and strain error is re-calculated in the sensing region. The result of the least square solution in the sensing region is expressed with $\boldsymbol{\varepsilon}$ for estimated strain and $\boldsymbol{\varepsilon}_{\mathrm{err}}$ for strain error. In the sensing region, there is quite difference between the estimated strain $\bar{\boldsymbol{\varepsilon}}$ considering full-field region and the estimated strain $\boldsymbol{\varepsilon}$ considering only sensing region. The difference also exists in the other area where strain is virtually measured, and the difference in the virtual region would be much larger. The larger the difference in the sensing region between $\bar{\boldsymbol{\varepsilon}}$ and $\boldsymbol{\varepsilon}$, the larger the estimation error.

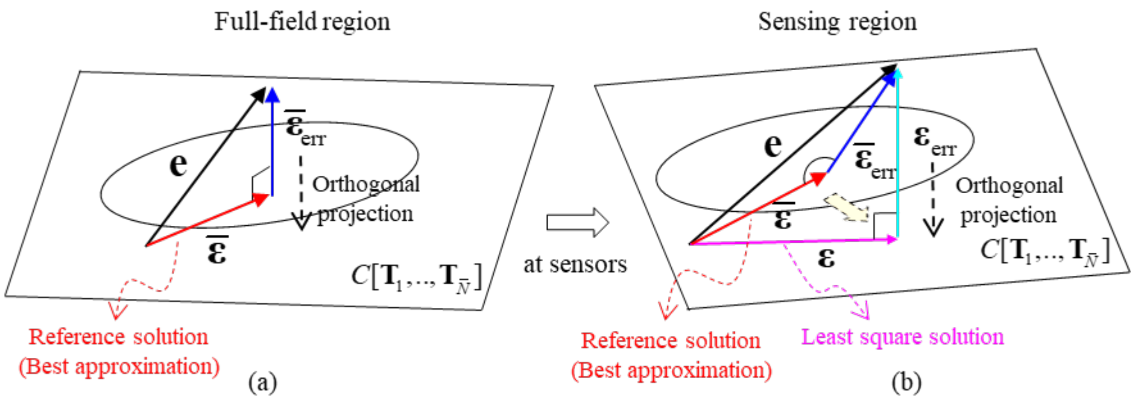

Figure A.3: Orthogonal projection of least square solution.

The measured strain is divided into approximated strain by the linear combination of basis vectors and strain error consisting of the truncation error and the measurement error. In the full-field region,

$$\mathbf{e} = \bar{\boldsymbol{\varepsilon}} + \bar{\boldsymbol{\varepsilon}}_{\mathrm{err}} \quad \text{with} \quad \bar{\boldsymbol{\varepsilon}} = \mathbf{T}\bar{\mathbf{q}}, \tag{A.2}$$

where $\bar{\mathbf{q}}$ is the generalized coordinate vector corresponding to reference strain considering full-field region.

Substituting Eq. (A.2) into Eq. (2.14),

$$\mathbf{q} = (\mathbf{T}^{\mathrm{T}}\mathbf{T})^{-1}\mathbf{T}^{\mathrm{T}}\mathbf{e} = (\mathbf{T}^{\mathrm{T}}\mathbf{T})^{-1}(\mathbf{T}^{\mathrm{T}}\bar{\boldsymbol{\varepsilon}} + \mathbf{T}^{\mathrm{T}}\bar{\boldsymbol{\varepsilon}}_{\mathrm{err}}). \tag{A.3}$$

The generalized coordinate vector for full-field region,

$$\mathbf{q} = \bar{\mathbf{q}} = (\mathbf{T}^{\mathrm{T}}\mathbf{T})^{-1}\mathbf{T}^{\mathrm{T}}\bar{\boldsymbol{\varepsilon}} \quad \text{with} \quad \mathbf{T}^{\mathrm{T}}\bar{\boldsymbol{\varepsilon}}_{\mathrm{err}} = \mathbf{0}, \tag{A.4}$$

where strain error does not affect the value of the generalized coordinate vector because strain error is orthogonal to strain basis vectors. Thus, the $\bar{\mathbf{q}}$ having the maximum accuracy is obtained if full-field region is considered.

In contrast, the generalized coordinates for the sensing region,

$$\mathbf{q} = \bar{\mathbf{q}} + \mathbf{q}_{\mathrm{err}} \quad \text{with} \quad \bar{\mathbf{q}} = (\mathbf{T}^{\mathrm{T}}\mathbf{T})^{-1}\mathbf{T}^{\mathrm{T}}\bar{\boldsymbol{\varepsilon}}, \ \mathbf{q}_{\mathrm{err}} = (\mathbf{T}^{\mathrm{T}}\mathbf{T})^{-1}\mathbf{T}^{\mathrm{T}}\bar{\boldsymbol{\varepsilon}}_{\mathrm{err}}. \tag{A.5}$$

The strain error considering full-field region is no longer orthogonal to strain basis vectors in the sensing region as shown in Fig. A.3. This results in a difference by $\mathbf{q}_{\mathrm{err}}$ for the $\bar{\mathbf{q}}$ and this reduces the accuracy of the virtual sensing over the entire area of the structural, not only sensing region but also virtual sensing region.

The correlations of basis vectors by the limited sensing region, strain error by truncation and measurement error, and orthogonal projection of least square solution cause $\mathbf{q}_{\mathrm{err}}$ in the sensing region. Therefore, these are error sources of virtual sensing reducing the performance of virtual sensing.

Appendix B. Regularization factor

Regularization of generalized coordinates in Eq. (2.32) shows good virtual sensing performance with the proper regularization factor α. Parametric studies are, however, required to determine the proper α value depending on the structures. As the regularization factor increases, estimated strain converges to zero because generalized coordinates converge to zero to minimize the cost function in Eq. (2.31).

To prevent estimated strain from converging to zero, the generalized coordinate vector is scaled by a scale factor β as

$$\mathbf{q} = \beta\overline{\mathbf{q}}' = \beta(\mathbf{T}^{\mathrm{T}}\mathbf{T} + \alpha\mathbf{I})^{-1}\mathbf{T}^{\mathrm{T}}\mathbf{e}\,. \tag{B.1}$$

Substituting Eq. (B.1) to Eq. (2.13), the cost function is re-defined

$$\tilde{C} = \sum_{i=1}^{M}\left(\varepsilon_i - e_i\right)^2 = (\boldsymbol{\varepsilon} - \mathbf{e})^{\mathrm{T}}(\boldsymbol{\varepsilon} - \mathbf{e}) = (\beta\mathbf{T}\overline{\mathbf{q}}' - \mathbf{e})^{\mathrm{T}}(\beta\mathbf{T}\overline{\mathbf{q}}' - \mathbf{e})\,, \tag{B.2}$$

and minimizing the cost function by $\dfrac{\partial\tilde{C}}{\partial\beta} = 0$, the following scale factor β is found as

$$\beta = \frac{(\mathbf{T}\overline{\mathbf{q}}')^{\mathrm{T}}\mathbf{e}}{(\mathbf{T}\overline{\mathbf{q}}')^{\mathrm{T}}(\mathbf{T}\overline{\mathbf{q}}')} \quad \text{with} \quad \overline{\mathbf{q}}' = (\mathbf{T}^{\mathrm{T}}\mathbf{T} + \alpha\mathbf{I})^{-1}\mathbf{T}^{\mathrm{T}}\mathbf{e}\,. \tag{B.3}$$

Using the scaled generalized coordinate vector with the resulting β, nodal displacement vector and strain and stress fields are estimated by Eq. (2.15), Eq. (2.16), and Eq. (2.17), respectively.

In order to analyze the effect of regularization factor on strain estimation, virtual sensing is carried with a wide range of regularization factor α and evaluated by estimation error. The estimation error is defined with estimated and measured strain vectors consisting of 26 axial strains at input and validation sensors during 4 times periods of the wave as

$$\mathrm{Err} = \frac{1}{4T}\int_0^{4T}\frac{\left\|\boldsymbol{\varepsilon}(t) - \mathbf{e}(t)\right\|}{\left\|\mathbf{e}(t)\right\|}dt \tag{B.4}$$

where T is the wave period, $\mathbf{e}(t)$ is measured strain vector at time t, and $\boldsymbol{\varepsilon}(t)$ is estimated strain vector corresponding to $\mathbf{e}(t)$.

Fig. B.1 shows estimation error according to regularization factor, where errors are normalized by that of the conventional least square solution in Eq. (2.14). The estimation error with the regularization scheme decreases in the beginning, and then converges as the regularization factor increases. In addition, the difference is not significant between minimum estimation error and converged estimation error.

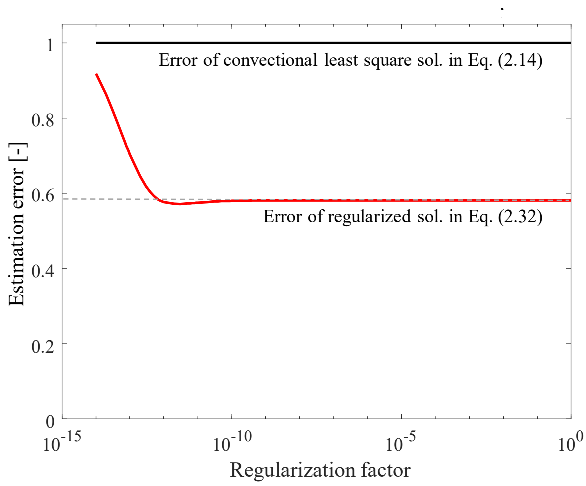

Figure B.1: Estimation error according to regularization factor.

This result implies that high estimation accuracy, as much as that of optimal regularization factor, would be obtained using a sufficiently large regularization factor to Eq. (2.32), and the parametric study to determine the value of α is not required.

As the regularization factor becomes larger, $(\mathbf{T}^{\mathrm{T}}\mathbf{T}+\alpha\mathbf{I})$ in Eq. (2.32) converges to the identity matrix whose components is α ; that is,

$$(\mathbf{T}^{\mathrm{T}}\mathbf{T}+\alpha\mathbf{I}) \approx \alpha\mathbf{I} \quad \text{with} \quad \alpha >> \max(\mathbf{T}^{\mathrm{T}}\mathbf{T}) \tag{B.5}$$

where $\max(\mathbf{T}^{\mathrm{T}}\mathbf{T})$ denotes the maximum value among absolute of $\mathbf{T}^{\mathrm{T}}\mathbf{T}$ components.

In other words, if the regularization factor is large enough, it has the same effect as assuming that basis vectors are uncorrelated. Therefore, regularization scheme is modified using the assumption that strain basis vectors are uncorrelated, but maintaining the estimation accuracy as much as that with optimal α.

Assuming the basis vectors are completely uncorrelated, the generalized coordinate vector becomes proportional to the measured strain vector projected on the strain basis vectors; that is, the generalized coordinate vector is expressed using a scale factor γ as

$$\mathbf{q} = \gamma \mathbf{T}^{\mathrm{T}} \mathbf{e} \tag{B.6}$$

Substituting Eq. (B.6) into Eq. (2.13), the cost function is re-defined

$$\hat{C} = \sum_{i=1}^{M} \left(\varepsilon_i - e_i \right)^2 = (\boldsymbol{\varepsilon} - \mathbf{e})^{\mathrm{T}} (\boldsymbol{\varepsilon} - \mathbf{e}) = (\gamma \mathbf{T}\mathbf{q} - \mathbf{e})^{\mathrm{T}} (\gamma \mathbf{T}\mathbf{q} - \mathbf{e}) . \tag{B.7}$$

In the same way, minimizing the cost function by $\frac{\partial \hat{C}}{\partial \gamma} = 0$, the optimal scale factor γ is found as

$$\gamma = ((\mathbf{T}\mathbf{T}^{\mathrm{T}}\mathbf{e})^{\mathrm{T}} (\mathbf{T}\mathbf{T}^{\mathrm{T}}\mathbf{e}))^{-1} (\mathbf{T}\mathbf{T}^{\mathrm{T}}\mathbf{e})^{\mathrm{T}} \mathbf{e} . \tag{B.8}$$

As a result, with the uncorrelated basis assumption, generalized coordinate vector is calculated as

$$\mathbf{q} = \left[\left((\mathbf{T}\mathbf{T}^{\mathrm{T}}\mathbf{e})^{\mathrm{T}} (\mathbf{T}\mathbf{T}^{\mathrm{T}}\mathbf{e}) \right)^{-1} (\mathbf{T}\mathbf{T}^{\mathrm{T}}\mathbf{e})^{\mathrm{T}} \mathbf{e} \right] \mathbf{T}^{\mathrm{T}} \mathbf{e} . \tag{B.9}$$

The regularization with the uncorrelated assumption $(\alpha >> \max(\mathbf{T}^{\mathrm{T}}\mathbf{T}))$ calculates the *i*th generalized coordinate using only *i*th strain basis vector as Eq. (B.9), whereas the conventional least square solution $(\alpha = 0)$ in Eq. (2.14) calculates the *i*th generalized coordinate using $\bar{N}$ given strain basis vectors. That is, the regularization factor α adjusts the extent of correlation between basis vectors according to its value.

This means the regularization scheme estimates the solution with low order approximation using low DOFs compared to the conventional least square solution, and the order of approximation is adjusted by the regularization factor α. As α increases, the regularization scheme approximates the solution with lower orders, and if the value of α is large enough to make the basis vectors uncorrelated completely, solution is approximated using only 1 DOF $(\mathbf{q}_i = \gamma \mathbf{T}_i^{\mathrm{T}} \mathbf{e})$. This results in a relatively smooth representation of estimated strain and improves the performance of the virtual sensing by preventing estimated strain from being overfitted to the measured strain. Therefore, the regularization scheme, mitigating overfitting through low order approximation, will be more effective when measured strain signal contains some amount of strain error that causes overfitting.

In projection perspective, regularization scheme approximates the solution through the tilted projection on the basis vectors rather than orthogonal projection as described in Fig. B.2, which allows more accurate strain estimation. The direction of the tilted projection is adjusted according to the regularization factor α.

Furthermore, if basis vectors are nearly orthogonal, the regularization with uncorrelated assumption is appropriate to apply, but if highly correlated, the regularization with the proper α determined through the parametric study is recommend.

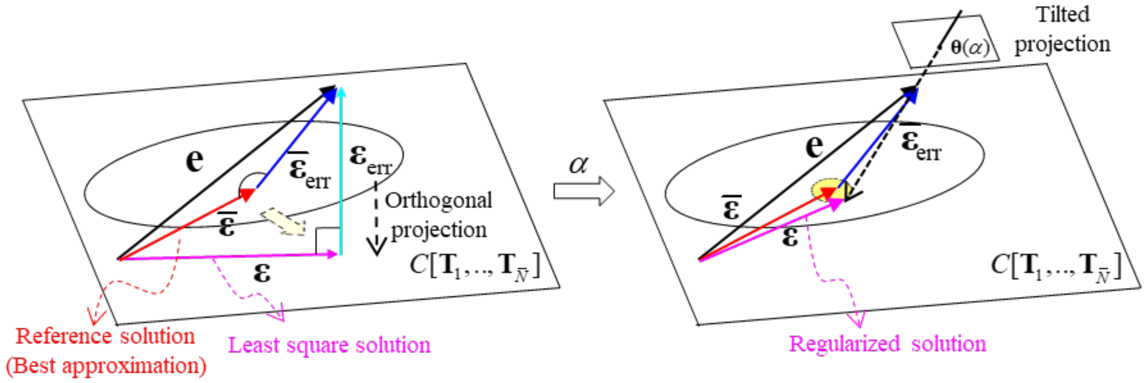

Figure B.2: Tilted projection of regularization scheme.

Bibliography

[1] Go M-S, Lim JH, Lee S. Physics-informed neural network-based surrogate model for a virtual thermal sensor with real-time simulation. International Journal of Heat and Mass Transfer 2023; 214: 124392.

[2] Tarpø M, Nabuco B, Georgakis C, Brincker R. Expansion of experimental mode shape from operational modal analysis and virtual sensing for fatigue analysis using the modal expansion method. International journal of fatigue 2020; 130: 105280.

[3] Avitabile P, Pingle P. Prediction of full field dynamic strain from limited sets of measured data. Shock and vibration 2012; 19: 765-785.

[4] Kefal A, Mayang JB, Oterkus E, Yildiz M. Three dimensional shape and stress monitoring of bulk carriers based on iFEM methodology. Ocean Engineering 2018; 147: 256-267.

[5] Kefal A, Oterkus E. Displacement and stress monitoring of a Panamax containership using inverse finite element method. Ocean Engineering 2016; 119: 16-29.

[6] Kefal A, Oterkus E. Displacement and stress monitoring of a chemical tanker based on inverse finite element method. Ocean Engineering 2016; 112: 33-46.

[7] Kefal A, Tessler A, Oterkus E. An enhanced inverse finite element method for displacement and stress monitoring of multilayered composite and sandwich structures. Composite Structures 2017; 179: 514-540.

[8] Lee S, Park M, Oh M-H, Lee P-S. Virtual sensing for real-time strain field estimation and its verification on a laboratory-scale jacket structure under water waves. Computers & Structures 2024; 298: 107344.

[9] Sisson W, Karve P, Mahadevan S. Digital twin approach for component health-informed rotorcraft flight parameter optimization. AIAA Journal 2022; 60: 1923-1936.

[10] Tarpø M, Amador S, Katsanos E, Skog M, Gjødvad J, Brincker R. Data-driven virtual sensing and dynamic strain estimation for fatigue analysis of offshore wind turbine using principal component analysis. Wind Energy 2022; 25: 505-516.

[11] Haag S, Anderl R. Digital twin–Proof of concept. Manufacturing letters 2018; 15: 64-66.

[12] Cimino C, Negri E, Fumagalli L. Review of digital twin applications in manufacturing. Computers in industry 2019; 113: 103130.

[13] Li C, Mahadevan S, Ling Y, Choze S, Wang L. Dynamic Bayesian network for aircraft wing health monitoring digital twin. Aiaa Journal 2017; 55: 930-941.

[14] Wang S, Lai X, He X, Qiu Y, Song X. Building a trustworthy product-level shape-performance integrated digital twin with multifidelity surrogate model. Journal of Mechanical Design 2022; 144: 031703.

[15] Park J-W, Sim S-H, Jung H-J. Displacement estimation using multimetric data fusion. IEEE/ASME Transactions On Mechatronics 2013; 18: 1675-1682.
[16] Pedersen EB, Jørgensen D, Riber HJ, Ballani J, Vallaghé S, Paccaud B. True fatigue life calculation using digital twin concept and operational modal analysis. The 29th International Ocean and Polar Engineering Conference 2019.
[17] Rasheed A, San O, Kvamsdal T. Digital twin: Values, challenges and enablers from a modeling perspective. Ieee Access 2020; 8: 21980-22012.
[18] Tao F, Zhang H, Liu A, Nee AY. Digital twin in industry: State-of-the-art. IEEE Transactions on industrial informatics 2018; 15: 2405-2415.
[19] Kefal A, Yildiz M. Modeling of sensor placement strategy for shape sensing and structural health monitoring of a wing-shaped sandwich panel using inverse finite element method. Sensors 2017; 17: 2775.
[20] Dong P, Hong J. The master SN curve approach to fatigue evaluation of offshore and marine structures. International Conference on Offshore Mechanics and Arctic Engineering 2004; 37440: 847-855.
[21] Lotsberg I, Sigurdsson G. Hot spot stress SN curve for fatigue analysis of plated structures. Journal of offshore mechanics and Arctic engineering 2006; 128: 330-336.
[22] Bogert P, Haugse E, Gehrki R. Structural shape identification from experimental strains using a modal transformation technique. 44th AIAA/ASME/ASCE/AHS/ASC Structures, Structural Dynamics, and Materials Conference 2003; 1626.
[23] Pisoni AC, Santolini C, Hauf DE, Dubowsky S. Displacements in a vibrating body by strain gage measurements. Proceedings-SPIE the International Society for Optical Engineering 1995; 119-119.
[24] Rapp S, Kang L-H, Han J-H, Mueller UC, Baier H. Displacement field estimation for a two-dimensional structure using fiber Bragg grating sensors. Smart Materials and Structures 2009; 18: 025006.
[25] Kang L-H, Kim D-K, Han J-H. Estimation of dynamic structural displacements using fiber Bragg grating strain sensors. Journal of sound and vibration 2007; 305: 534-542.
[26] Pelayo F, Skafte A, Aenlle ML, Brincker R. Modal analysis based stress estimation for structural elements subjected to operational dynamic loadings. Experimental Mechanics 2015; 55: 1791-1802.
[27] Baqersad J, Niezrecki C, Avitabile P. Extracting full-field dynamic strain on a wind turbine rotor subjected to arbitrary excitations using 3D point tracking and a modal expansion technique. Journal of Sound and Vibration 2015; 352: 16-29.
[28] Tarpø M, Friis T, Nabuco B, Amador S, Katsanos E, Brincker R. Operational modal analysis based stress estimation in friction systems. Springer 2019; 143-153.
[29] Yu M, Guo J, Lee K-M. A modal expansion method for displacement and strain field reconstruction of a thin-

wall component during machining. IEEE/ASME Transactions on Mechatronics 2018; 23: 1028-1037.

[30] Henkel M, Weijtjens W, Devriendt C. Fatigue stress estimation for submerged and sub-soil welds of offshore wind turbines on monopiles using modal expansion. Energies 2021; 14: 7576.

[31] Foss G, Haugse E. Using modal test results to develop strain to displacement transformations. Proceedings of the 13th international modal analysis conference 1995; 2460: 112.

[32] Ko WL, Richards WL, Fleischer VT. Applications of Ko displacement theory to the deformed shape predictions of the doubly-tapered Ikhana Wing. 2009.

[33] Kefal A, Oterkus E, Tessler A, Spangler JL. A quadrilateral inverse-shell element with drilling degrees of freedom for shape sensing and structural health monitoring. Engineering science and technology, an international journal 2016; 19: 1299-1313.

[34] Kefal A, Tabrizi IE, Yildiz M, Tessler A. A smoothed iFEM approach for efficient shape-sensing applications: Numerical and experimental validation on composite structures. Mechanical Systems and Signal Processing 2021; 152: 107486.

[35] Gherlone M, Cerracchio P, Mattone M, Di Sciuva M, Tessler A. An inverse finite element method for beam shape sensing: theoretical framework and experimental validation. Smart Materials and Structures 2014; 23: 045027.

[36] Tessler A, Spangler JL. A least-squares variational method for full-field reconstruction of elastic deformations in shear-deformable plates and shells. Computer methods in applied mechanics and engineering 2005; 194: 327-339.

[37] Fang Z, Wang M, Hu W, Chang K, Zhang B. Temperature-Field Sparse-Reconstruction of Lithium-Ion Battery Pack Based on Artificial Neural Network and Virtual Thermal Sensor Technology. Energy Technology 2021; 9: 2100258.

[38] Shin S, Ko B, So H. Noncontact thermal mapping method based on local temperature data using deep neural network regression. International Journal of Heat and Mass Transfer 2022; 183: 122236.

[39] Wang M, Hu W, Jiang Y, Su F, Fang Z. Internal temperature prediction of ternary polymer lithium-ion battery pack based on CNN and virtual thermal sensor technology. International Journal of Energy Research 2021; 45: 13681-13691.

[40] Xie J, Yang R, Gooi HB, Nguyen HD. PID-based CNN-LSTM for accuracy-boosted virtual sensor in battery thermal management system. Applied Energy 2023; 331: 120424.

[41] Raissi M, Perdikaris P, Karniadakis GE. Physics-informed neural networks: A deep learning framework for solving forward and inverse problems involving nonlinear partial differential equations. Journal of Computational physics 2019; 378: 686-707.

[42] Iliopoulos A, Weijtjens W, Van Hemelrijck D, Devriendt C. Fatigue assessment of offshore wind turbines on

monopile foundations using multi-band modal expansion. Wind Energy 2017; 20: 1463-1479.
[43] Henkel M, Weijtjens W, Devriendt C. Validation of virtual sensing on subsoil strain data of an offshore wind turbine. International Operational Modal Analysis Conference 2019.
[44] Iliopoulos A, Weijtjens W, Hemelrijck DV, Devriendt C. Full-field strain prediction applied to an offshore wind turbine. Springer 2016; 349-357.
[45] Skafte A, Kristoffersen J, Vestermark J, Tygesen UT, Brincker R. Experimental study of strain prediction on wave induced structures using modal decomposition and quasi static Ritz vectors. Engineering structures 2017; 136: 261-276.
[46] Andrade P, Santos J, Escórcio P. Direct integration methods versus modal superposition method, on predicting staircases vibrations. Procedia Structural Integrity 2020; 28: 279-286.
[47] Bathe KJ. Finite element procedures. K.J. Bathe, Watertown, MA 2016.
[48] Avitabile P. Modal testing: a practitioner's guide. John Wiley & Sons 2017.
[49] Heylen W, Sas P. Modal analysis theory and testing. 2006.
[50] Kim H-J, Yoon K, Lee P-S. Continuum mechanics based beam elements for linear and nonlinear analyses of multi-layered composite beams with interlayer slips. Composite Structures 2020; 235: 111740.
[51] Yoon K, Lee P-S, Kim D-N. An efficient warping model for elastoplastic torsional analysis of composite beams. Composite Structures 2017; 178: 37-49.
[52] Kim S, Lee P-S. A new enriched 4-node 2D solid finite element free from the linear dependence problem. Computers & Structures 2018; 202: 25-43.
[53] Reddy JN. An introduction to continuum mechanics. Cambridge university press 2013.
[54] Saini DS, Karmakar D, Ray-Chaudhuri S. A review of stress concentration factors in tubular and non-tubular joints for design of offshore installations. Journal of Ocean Engineering and Science 2016; 1: 186-202.
[55] Ko Y, Lee Y, Lee P-S, Bathe K-J. Performance of the MITC3+ and MITC4+ shell elements in widely-used benchmark problems. Computers & Structures 2017; 193: 187-206.
[56] Lee C, Lee P-S. The strain-smoothed MITC3+ shell finite element. Computers & Structures 2019; 223: 106096.
[57] Wilson EL, Yuan MW, Dickens JM. Dynamic analysis by direct superposition of Ritz vectors. Earthquake Engineering & Structural Dynamics 1982; 10: 813-821.
[58] Hansteen OE, Bell K. On the accuracy of mode superposition analysis in structural dynamics. Earthquake Engineering & Structural Dynamics 1979; 7: 405-411.
[59] Sarpkaya T. Force on a circular cylinder in viscous oscillatory flow at low Keulegan—Carpenter numbers.

Journal of Fluid Mechanics 1986; 165: 61-71.

[60] Gudmestad OT, Moe G. Hydrodynamic coefficients for calculation of hydrodynamic loads on offshore truss structures. Marine Structures 1996; 9: 745-758.

[61] Phillips O. The dynamics of the upper ocean, Cambridge Univ. Press, Cambridge 1977.

[62] Dingemans MW. Water wave propagation over uneven bottoms: Linear wave propagation. World Scientific 2000.

[63] Penzien J. Dynamics of structures. McGraw-Hill 1993.

[64] Greub WH. Linear algebra. Springer Science & Business Media 2012.

[65] Wijker JJ. Modal effective mass. Spacecraft structures 2008; 247-263.

[66] Lundin B, Mårtensson P. Finding general guidelines for choosing appropriate cut-off frequencies for modal analyses of railway bridges trafficked by high-speed trains. Division of Solid Mechanics, Lund University 2006.

[67] Everitt BS, Skrondal A. The Cambridge dictionary of statistics. 2010.

[68] Bottou L, Bousquet O. The tradeoffs of large scale learning. Advances in neural information processing systems 2007; 20.

[69] Harrell FE. Regression modeling strategies. Bios 2017; 330: 14.

[70] Tikhonov AN, Arsenin V. Solutions of ill-posed problems. (No Title) 1977.

[71] Hoerl AE, Kennard RW. Ridge regression: Biased estimation for nonorthogonal problems. Technometrics 1970; 12: 55-67.

[72] Khalaf G, Shukur G. Choosing ridge parameter for regression problems. 2005.

[73] National Instruments. NI 9236 Datasheet & Specifications. https://www.ni.com.

[74] National Instruments. NI 9178 Datasheet & Specifications. https://www.ni.com.

[75] National Instruments. Manuals - LabVIEW Fundamentals. https://www.ni.com.

[76] HBM. Strain Gauge Catalogue - Strain Gauges: First choice for strain measurements. https://www.hbm.com.

[77] Heylen W, Lammens S. FRAC: a consistent way of comparing frequency response functions. Proceedings of the conference on identification in engineering systems 1996; 48-57.

[78] Liu K, Yan R-J, Soares CG. Optimal sensor placement and assessment for modal identification. Ocean Engineering 2018; 165: 209-220.

[79] Yang C, Ma R, Ma R. Optimal sensor placement for modal identification in multirotary-joint solar power satellite. IEEE sensors journal 2020; 20: 7337-7346.

[80] Meo M, Zumpano G. On the optimal sensor placement techniques for a bridge structure. Engineering

structures 2005; 27: 1488-1497.

[81] Yao L, Sethares WA, Kammer DC. Sensor placement for on-orbit modal identification via a genetic algorithm. AIAA journal 1993; 31: 1922-1928.

[82] Brunton SL. Data Driven Science & Engineering.

[83] Willcox K. Unsteady flow sensing and estimation via the gappy proper orthogonal decomposition. Computers & fluids 2006; 35: 208-226.

[84] Kammer DC. Sensor placement for on-orbit modal identification and correlation of large space structures. Journal of Guidance, Control, and Dynamics 1991; 14: 251-259.

[85] Worden K, Burrows A. Optimal sensor placement for fault detection. Engineering structures 2001; 23: 885-901.

[86] Choi H-G, Lee P-S. The simplified MITC4+ shell element and its performance in linear and nonlinear analysis. Computers & Structures 2024; 290: 107177.

[87] Heylen W, Janter T. Extensions of the modal assurance criterion. 1990.

[88] Pastor M, Binda M, Harčarik T. Modal assurance criterion. Procedia Engineering 2012; 48: 543-548.